USGS Award No. G09AP00131

# VALIDATION OF METHODOLOGIES USED TO MAP EARTHQUAKE-INDUCED LANDSLIDE POTENTIAL

FINAL TECHNICAL REPORT

SUBMITTED: August 2011

**ELLEN M. RATHJE, PH.D., P.E.**
University of Texas at Austin
ECJ 9.227C, C1792
Austin, TX 78712
Tel: 512-471-4929
Fax: 512-471-6548
e.rathje@mail.utexas.edu
http://www.caee.utexas.edu/dept/area/geotech/GeotechnicalEngr.htm

**NEHRP Element:** III
**Key Words:** Earthquake Effects, Landslides, Ground Failure

*Research supported by the U.S. Geological Survey (USGS), Department of the Interior, under USGS award number (G09AP00131). The views and conclusions contained in this document are those of the authors and should not be interpreted as necessarily representing the official policies, either expressed or implied, of the U.S. Government*

## ABSTRACT

The rigid sliding-block analysis introduced by Newmark in 1965 has become a popular method for assessing the stability of slopes during earthquakes. Estimates of sliding displacement calculated using this methodology serve as an index of seismic performance and are used for mapping seismic landslide hazard potential. The original approach of rigorously integrating ground acceleration time-histories to compute estimates of sliding displacement has been replaced by the use of simple, empirical models that predict displacement as a function of a slope's yield acceleration and one or more measures of ground shaking. To have confidence in these models, the displacement computed by these models must be compared with observations of landslides from previous earthquakes.

Seven different empirical models were evaluated by comparing predicted displacements with an inventory of observed landslides from the 1994 Northridge, California earthquake. Using a comprehensive set of ground motion data and shear strength properties from the Northridge earthquake, sliding displacements were calculated within a geographic information system (GIS) and the accuracy of each model was computed. The influence of factors such as landslide size, geologic unit, slope angle, and material strength on the prediction of landslides was also evaluated. The results indicate that the accuracy of the predictive models depends less on the model used and more on the uncertainty in the model parameters, specifically the assigned shear strength values. Because current approaches do not take into account the spatial variability of strength within individual geologic units, the accuracy of the predictive models is controlled by the distribution of slope angles within observed and predicted landslide cells. Assigning overly conservative (low) shear strength values results in a higher percentage of landslides accurately identified, but also results in a large over-estimation of the seismic landslide hazard.

## NON-TECHNICAL SUMMARY

The methods used to predict the occurrence of earthquake-induced landslide integrate ground shaking, topographic, and geologic/strength information to generate estimates of downslope movement. These models are based predominantly on numerical simulation, and thus require comparison with the observed locations of landslides during previous earthquakes. This study evaluates seven different models by comparing their estimates of movement with observed landslides from the 1994 Northridge earthquake. The results indicate that, in general, many of the models do equally as well, and that the accuracy of the models depends mostly on the assigned strengths to the geologic units.

# Table of Contents

List of Tables ..... ix

List of Figures ..... xi

Chapter 1: Introduction ..... 1

1.1 Research Significance ..... 1

1.2 Scope of Research ..... 3

Chapter 2: Evaluation of Earthquake-Induced Landslides ..... 5

2.1 Introduction ..... 5

2.2 Permanent Displacement Analysis ..... 8

2.2.1 Yield acceleration ..... 11

2.2.2 Ground Motions ..... 13

2.2.3 Displacement Prediction Equations ..... 14

2.3 Seismic Landslide Hazard Maps ..... 16

2.3.1 CGS Approach ..... 17

2.3.2 USGS Approach ..... 20

2.4 Previous Validation Studies ..... 21

2.4.1 Jibson et al. (2000) ..... 22

2.4.2 McCrink (2001) ..... 28

2.5 Summary ..... 32

Chapter 3: Validation Approach for the Northridge Earthquake ..... 33

3.1 Introduction ..... 33

3.2 Northridge Earthquake Study Area ..... 34

3.3 Calculating Yield Acceleration ..... 36

3.3.1 Slope Angle ..... 37

3.3.2 Shear Strength Properties ..... 40

3.3.3 Maps of Yield Acceleration ..... 47

3.4 Calculating Permanent Displacements ..... 50

3.4.1 Predictive Models ..... 50

3.4.2 Ground Motion Data .....54
3.5 Evaluating the Use of Sliding Displacements to Predict Landslides .....59
3.5.1 Cell-by-Cell Approach .....69
3.5.2 Landslide-by-Landslide Approach .....72
3.6 Summary .....73
Chapter 4: Validation Results .....74
4.1 Introduction .....74
4.2 Maps of Sliding Displacement .....78
4.3 Comparison of Sliding Displacements with Observed Landslides .....86
4.3.1 Cell-by-cell Comparison .....86
4.3.2 Landslide-by-landslide Comparison .....95
4.3.3 Influence of Geologic Unit and Slope Angle on Model Accuracy .....102
4.4 Influence of Shear Strength on Landslide Predictions .....107
Chapter 5: Conclusions .....112
5.1 Summary and Conclusions .....112
5.1.1 Comparing Predictive Models .....113
5.1.2 Factors Influencing Model Accuracy .....114
5.2 Recommendations .....117
Appendix A: Maps of Data Used In This Study .....118
References .....143
Vita .....146

# Chapter 1

# Introduction

## 1.1 RESEARCH SIGNIFICANCE

Earthquakes pose a dangerous and costly threat to many people around the world. As the devastating March 11, 2011 earthquake in Japan ($M_w = 9.0$) has so tragically demonstrated, earthquake-induced hazards such as tsunamis often represent a greater threat to life and property than the ground shaking that occurs during an earthquake. Earthquake-induced landslides are another significant seismic hazard that can damage and destroy life and property, disrupt transmission lines, block roads and hamper relief efforts. The areas that are most susceptible to earthquake-induced landslides are mountainous regions that are in close proximity to active tectonic plate boundaries. In the United States this describes portions of coastal California, as well as large portions of the Pacific Northwest.

To be resilient to the effects of earthquake-induced landslides requires significant hazard planning on the part of communities and local governments. Hazard planning efforts are supported by research on the causes of seismic slope failures and how to

predict them in the future. Current research on studying earthquake-induced landslides from previous earthquakes typically involves the use of aerial photography and/or satellite imagery to identify the landslides that occurred during the earthquake, and an analysis of the geologic, hydrologic or other factors that may have contributed to the landsliding. Assuming that future landslides will occur under the same conditions as past events, these observations can be used to develop criteria for assessing potential seismic landslide hazards.

For planning purposes, regional maps of seismic landslide hazard potential are most useful. A seismic landslide hazard map delineates zones where earthquake-induced landslides are a concern and where additional investigation is required before developing the land. Current hazard mapping efforts for earthquake-induced landslides use estimates of sliding displacement to evaluate the potential for ground failure. In these procedures, slopes that are predicted to develop significant, permanent, downslope displacements during an earthquake are deemed seismically unstable. The use of a Geographic Information System (GIS) to create seismic landslide hazard maps has become widespread because it has the capabilities to collect, store, manipulate, display and analyze large amounts of spatially-referenced data quickly.

Mapping seismic landslide hazards requires an assessment of (1) the strength of the slope, (2) the expected level of ground shaking, and (3) a prediction of displacement. To have confidence in the developed methodology, it is important to validate the procedures against observations from previous earthquakes. The goal of this research is to validate the performance of some recently developed seismic landslide hazard mapping methodologies against observations of landsliding within six quadrangles in Los Angeles, California that were shaken by the 1994 Northridge earthquake. More than 11,000 triggered landslides were documented following the Northridge earthquake, the

majority of them occurring in the Santa Susana Mountains to the northwest of the earthquake epicenter. The results of this research can be used to improve current methods for creating seismic landslide hazard maps, and to identify elements of the mapping procedure that warrant further evaluation.

## 1.2 SCOPE OF RESEARCH

This thesis focuses on comparing the results from current seismic landslide hazard mapping procedures with observed landslides from the Northridge earthquake and assessing the model parameters that affect estimates of sliding displacement. Seven different displacement prediction models are used to predict displacements as a function of topography (slope angle), geology (material strength), and ground shaking estimates. These displacements are compared with locations of observed landslides from the 1994 Northridge earthquake. Several methods are used to assess and compare the accuracy of each model. The influence of the model parameters (slope angle, material strength) on the results is also evaluated in an effort to identify potential improvements in the modeling procedures.

Chapter 1 briefly discusses the significance of this research, and provides the scope and organization of this thesis.

Chapter 2 provides background information on seismic slope stability, common procedures used to assess the performance of slopes during earthquake shaking, and previous work conducted in seismic landslide hazard mapping.

Chapter 3 summarizes the procedures used in this research to calculate sliding block displacements, the data used by the different displacement prediction equations, and the proposed methods for comparing predicted displacements with observed landslides from the 1994 Northridge earthquake. This includes a cell-by-cell approach that assesses the accuracy of each model based on their ability to match predicted

landslide cells with observed landslide cells, and a landslide-by-landslide approach that assesses the accuracy of each model based on their ability to identify at least 50% of an observed landslide.

Chapter 4 presents and discusses the maps of sliding displacement developed for this study, and summarizes statistics on the accuracy of each displacement prediction equation using the methods described in Chapter 3. In addition, the influence of factors such as landslide size, geologic unit, slope angle, and material shear strength on the results is evaluated.

Chapter 5 discusses the significance of the results and provides conclusions and recommendations for future work in mapping earthquake-induced landslides.

Chapter 2

# Evaluation of Earthquake-Induced Landslides

## 2.1 INTRODUCTION

A landslide or slope failure refers to the downslope movement of soil and rock materials under the influence of gravity, caused by a destabilizing force or condition. Heavy rainfall and earthquake shaking are common natural causes for landslides. During an earthquake, sliding is expected when the strength of the slope materials is exceeded by a combination of the static stresses and the stresses imparted by the ground shaking. The best way to limit the risk of damage and prevent loss of life due to earthquake-induced landslides is to conduct seismic slope stability analyses and identify those slopes that represent the greatest seismic hazard. This chapter covers background information on seismic slope stability analyses, procedures for seismic landslide hazard mapping, and previous research in this area conducted by others.

Current methods to assess the performance of slopes during earthquakes are generally based on either *finite element modeling* or *limit equilibrium analysis* (Jibson, 2010). Dynamic finite element modeling is computationally intensive, requiring

a sufficient amount of high-quality data and intimate knowledge of the nonlinear stress-strain-strength characteristics of the soil, as well as specification of a suite of input acceleration-time histories. The goal of the analyses is to predict the level of deformation that will occur under the expected seismic loading. Due to the time and effort involved, this approach is typically reserved for critical projects such as earth dams.

A simpler alternative to finite element modeling is limit equilibrium analysis. The limit equilibrium approach is commonly used for static slope stability analyses. This approach considers the shear stresses along a failure surface and computes a factor of safety based on the available shear strength and the shear stresses required for equilibrium. The minimum factor of safety for a slope is estimated by trial and error for a large number of assumed failure surfaces. The limit equilibrium approach can be modified to consider seismic stability, and in this case is called pseudostatic slope stability analysis.

A pseudostatic slope stability analysis is a limit equilibrium analysis that models earthquake shaking as a destabilizing, horizontal static force. This concept is illustrated in Figure 2.1.

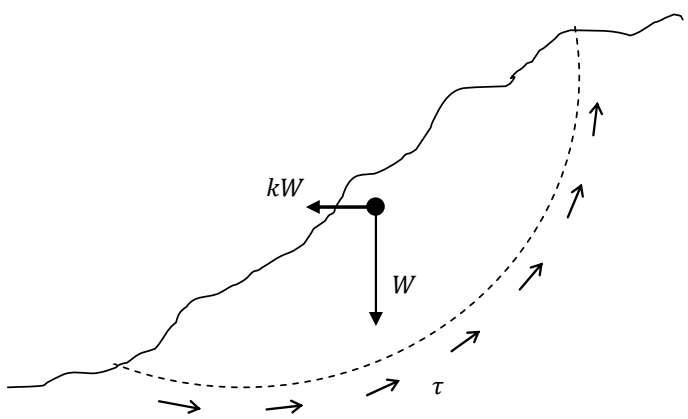


Figure 2.1: Pseudostatic force acting on a given failure surface

The destabilizing force, F, is given by:

$$F = kW \tag{2.1}$$

where $k$ is the seismic coefficient, $W$ is the weight of the sliding mass, and $\tau$ represents the mobilized shear strength of the soil along the failure surface (Kramer, 1996). A factor of safety is computed as the ratio of resisting forces (available shear strength) to driving forces (gravity + pseudostatic force).

The pseudostatic approach greatly simplifies the earthquake shaking problem and is not a very accurate representation of the complex, dynamic inertial forces that actually exist during earthquake shaking (Jibson, 2010). Other challenges are the selection of an appropriate seismic coefficient ($k$), which is typically selected to be some fraction of the expected peak ground acceleration, and the value of an acceptable factor of safety. The limit equilibrium analysis only shows a slope to be stable (FS < 1.0) or unstable (FS > 1.0) with no indication of the likelihood or consequences of instability.

Representing a compromise between the overly simplistic pseudostatic analysis and the more complex finite element analysis, permanent displacement analysis has become widely used in the earthquake engineering community to assess the seismic performance of slopes. This approach recognizes that the pseudostatic stability of a slope varies throughout earthquake shaking because ground accelerations vary, and that permanent displacements will accumulate during periods of instability (FS < 1.0). Calculated displacements do not necessarily correspond to observed movements in the field, but they do represent an index of the seismic performance and can be used to determine relative seismic hazard levels. Permanent displacement analysis is the basis for

the seismic landslide hazard mapping procedures used in this study and is discussed in more detail in the following sections.

## 2.2 PERMANENT DISPLACEMENT ANALYSIS

Permanent-displacement analysis (Newmark, 1965) models a potential landslide as a rigid block resting on an inclined plane (Figure 2.2). If a dynamic force exerted on the block exceeds the shear resistance at the sliding interface, the block displaces downslope. The base acceleration required to generate a force that overcomes the shear resistance and initiates sliding is known as the critical or yield acceleration ($k_y$). The application of $k_y$ results in a factor of safety FS = 1.0.

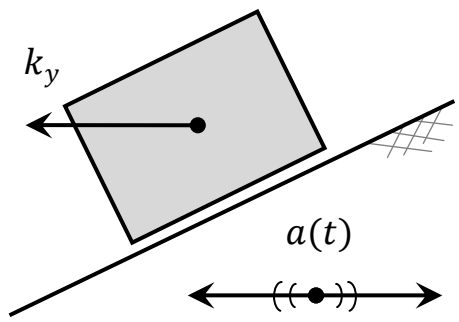


Figure 2.2: Sliding block model used in permanent displacement analysis

Provided with an earthquake acceleration-time history, any portion of the record that exceeds the yield acceleration contributes to the accumulation of permanent displacements. The movement of the block relative to the inclined plane can be obtained by integrating the relative acceleration (i.e. the difference between the acceleration and $k_y$) twice; this procedure is illustrated in Figure 2.3. Every time the yield acceleration is exceeded, the amount of relative sliding displacement induced is related to both the

amount by which the yield acceleration is exceeded, and the length of time spent sliding. Thus, the total relative displacement is influenced by the amplitude, frequency content and duration of shaking (Kramer, 1996).

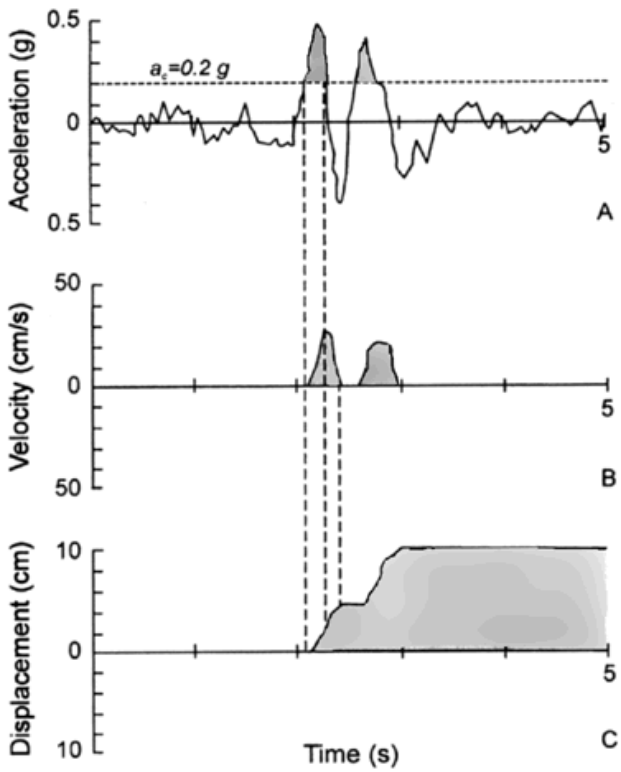


Figure 2.3: Demonstration of sliding block displacement calculation for a yield acceleration ($k_y = a_c$ in figure) of 0.20 g (Jibson et al., 2000)

An important assumption of the original sliding block analysis is that the displaced mass is a rigid-plastic body; the block itself does not deform and no permanent displacements are experienced until the yield acceleration is exceeded. In reality, though, landslide masses do not behave as rigid-plastic bodies and they deform internally during earthquake shaking. The internal deformations represent the dynamic response of the sliding mass during earthquake shaking. As an earthquake ground motion propagates

through a slope, different parts of the slope move differently and in different directions. These differences are typically small for thin failure masses, and more considerable for thick failure masses (Kramer, 1997). The dynamic response of a potential landslide mass can be accounted for by performing a more rigorous decoupled sliding block analysis. In this two-step process, the spatially varying ground acceleration distribution within the sliding mass is computed (assuming no sliding) and used to calculate an average acceleration-time history. This average acceleration at any instant during ground shaking represents the inertial force associated with the ground acceleration distribution within the sliding mass. The resulting average acceleration time-history is then input into a rigid-block analysis to compute permanent displacement (Jibson, 2010). Decoupled analysis has been shown to accurately predict field behavior, but requires an estimate of the dynamic response of the sliding mass.

Decoupled sliding block analysis is required for deeper sliding masses because the dynamic response of the sliding mass is of significance. Rigid sliding block analysis ignores the dynamic response of the sliding mass, and thus it is most applicable to thin, veneer slope failures. This failure mode is common in natural slopes (Keefer, 1984).

In its original application, conducting a rigorous permanent displacement analysis requires an estimate of the yield acceleration of the slope and an acceleration-time history (or suite of time histories) that represents the expected earthquake shaking at the site. More recent applications use empirical predictive models that compute displacements as a function of the yield acceleration and one or more ground motion parameters (e.g. Jibson (2007), Saygili and Rathje (2008), Rathje and Saygili (2009)). Typical procedures for calculating the yield acceleration, selecting appropriate ground motion data and calculating permanent displacements are discussed in the following sections.

### 2.2.1 Yield acceleration

For a given slope and an assumed failure surface, such as the one considered in Figure 2.1, the critical or yield acceleration can be estimated by iteratively performing a pseudostatic analysis to determine the seismic coefficient that results in a factor of safety of FS = 1.0. The seismic coefficient multiplied by g is equivalent to the yield acceleration. Selection of the critical slip surface geometry that results in the lowest seismic coefficient is a trial and error process. However, most failures in natural slopes are shallow and have small thickness to length ratios (Keefer, 1984, 2002). In these cases an infinite slope model can be used to approximate the slip surface geometry.

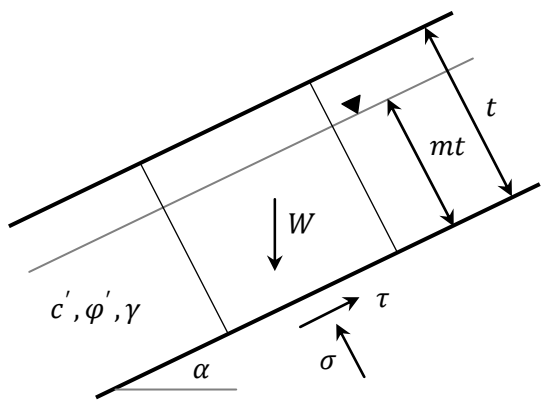


Figure 2.4: Infinite slope model under static conditions

The geometry of the infinite slope model is shown in Figure 2.4. In this figure $c'$ is the effective cohesion, $\varphi'$ is the effective friction angle, $\gamma$ is the material unit weight, $\alpha$ is the slope angle, $t$ is the slope-normal thickness of the rigid block, $m$ is the proportion of the block thickness that is saturated, $W$ is the weight of the sliding block, and $\tau$ and $\sigma$ are the shear and normal stresses acting on the slip surface, respectively (Jibson et al., 2000).

If one considers earthquake shaking to occur parallel to a slope (Newmark, 1965), the yield acceleration can be expressed as a simple function of the static factory of safety, the acceleration of gravity and the slope angle:

$$k_y = (FS - 1)g \cdot sin\alpha \tag{2.2}$$

A somewhat different equation results if the ground acceleration is assumed to be horizontal rather than parallel to the slope, but the differences in the computed values of $k_y$ are small (Saygili, 2008). Based on the slope geometry and the soil properties represented in Figure 2.4, the static factor of safety for an infinite slope model is computed as:

$$FS = \frac{c\prime}{\gamma t \sin\alpha} + \frac{\tan\varphi\prime}{\tan\alpha}\left(1 - m\frac{\gamma_w}{\gamma}\right) \tag{2.3}$$

For regional applications of the infinite slope model, slope angles are derived from a Digital Elevation Model (DEM), and nominal values for unit weight, saturation and block thickness are typically assumed. The main source of uncertainty in calculating the static factor of safety (and thus the yield acceleration) is the assigned material shear strength properties.

Shear strength is typically assigned using Mohr-Coulomb strength parameters $c'$ and $\varphi'$ obtained from direct shear or triaxial tests. For unsaturated materials ($m = 0$), this represents total stress conditions. For saturated materials ($m > 0$), the changes in pore pressures generated during earthquake shaking are generally ignored such that the strength is assigned using $c'$, $\varphi'$, and the effective stresses before shaking. This is generally conservative, however, because non-liquefiable sands are typically dense and

negative pore pressures are generated due to dilatancy, resulting in higher temporary strengths. Using $c'$ and $\varphi'$ to assign strengths is not appropriate for liquefiable (loose) sands, but the sliding block analysis is not applicable to these soils. For clay sites, an undrained strength ($s_u$) is assigned and $\varphi = 0$.

Shear strength data are compiled and assigned based on geologic units. Variability within a geologic unit is typically ignored due to practical constraints. After values of $c'$ and $\varphi'$ are assigned, yield accelerations can be calculated and combined with ground shaking information to compute estimates of sliding displacement.

### 2.2.2 Ground Motions

To conduct a rigorous sliding-block displacement analysis, ground acceleration-time histories are required. The selection of appropriate acceleration-time histories is often guided by the results of a probabilistic seismic hazard analysis (PSHA). PSHA takes into account all possible earthquake scenarios (i.e., magnitude and distance) around a particular site to compute the probability of exceedance of a specified ground motion level across multiple spectral periods. These “hazard curves” are used to develop a target acceleration response spectrum based on a design hazard level, typically a 10% or 2% probability of exceedance in 50 years.

Using a public database of available ground motion recordings from previous earthquakes, and one of a handful of widely available software programs, time histories are selected to fit the PSHA-derived target response spectrum. For a given hazard level, there are magnitude and distance combinations that contribute more to that hazard – this information can be acquired by performing what is known as a deaggregation of the hazard. Ground motions are not only selected based on how well they match the target response spectrum, but also based on how well they match the magnitude and distance from the deaggregation. Because of the large aleatory variability in earthquake ground

motions, it is recommended that a suite of motions be considered when fitting a PSHA-derived target.

Given an estimate of the yield acceleration and a suite of ground motions, a sliding displacement can be calculated for each ground motion. Displacement is computed by double integrating the difference between the acceleration-time history and the yield acceleration. This integration initiates when the acceleration exceeds the yield acceleration, and continues until the relative velocity between the ground and sliding block becomes zero. The average displacement from the suite of ground motions is often used as the expected displacement.

### 2.2.3 Displacement Prediction Equations

Conducting a rigorous sliding-block analysis is relatively straightforward, but for a large, regional hazard analysis it can be impractical to try and select multiple, unique acceleration-time histories for the conditions to be modeled. Double integrating all of these time histories multiple times for every slope is also time consuming. A simpler approach is to use an empirical regression equation which is based on displacements computed for a large database of ground motions and $k_y$ values. Because the magnitude of predicted displacement is sensitive to the characteristics of earthquake ground motions (i.e. intensity, frequency content, duration), researchers have developed models that estimate displacements as a function of yield acceleration and one or more ground motion (GM) parameters, using the form:

$$\ln D = f(k_y, GM\ parameters) \tag{2.4}$$

Peak ground acceleration (PGA) is the most commonly used measure of ground shaking intensity, and the ratio of yield acceleration to PGA ($k_y/PGA$) is used in recent

predictive models developed by Saygili and Rathje (2008), Rathje and Saygili (2009), and Jibson (2007). The ratio of $k_y/PGA$ is a useful parameter to incorporate in a predictive model because $k_y/PGA \geq 1.0$ indicates that the peak ground acceleration does not exceed the yield acceleration and that there is zero displacement. One of the limitations of using PGA to characterize a ground motion is that it only measures a single point in the acceleration-time history, and therefore does not provide information on the frequency content or duration of the motion. Therefore additional parameters are required to characterize the ground motion. Peak ground velocity (PGV) can be obtained by integrating the acceleration-time history over time, and has been shown to correlate to earthquake damage better than PGA (Wu et al. 2003).

A more comprehensive measure of shaking intensity was developed by Arias (1970) and is related to the integral over time of squared accelerations in a strong-motion record:

$$I_a = \frac{\pi}{2g} \int [a(t)]^2 dt \tag{2.5}$$

where $I_a$ is Arias intensity in units of velocity (m/s) and $a(t)$ is ground acceleration as a function of time. Jibson (1993, 2007) and Jibson et al. (1998, 2000) developed models that relate displacement to yield acceleration and $I_a$, and Arias intensity is one of several ground motion parameters used by Saygili and Rathje (2008). Other ground motion parameters that have been used include the natural period of the sliding mass ($T_s$) and the spectral acceleration at select periods (Bray and Travasarou, 2007).

Displacement prediction equations essentially provide the same information as a rigorous sliding block analysis, but require less time and effort. The median calculated displacement is also more stable than a value derived from a single acceleration-time history or a small suite of time histories. The different predictive models are generally

judged based on their ability to reduce the standard deviation of the prediction, which, for a given $k_y$ and ground motion level, can result in a range of expected displacements greater than one order of magnitude (Saygili and Rathje, 2008).

## 2.3 SEISMIC LANDSLIDE HAZARD MAPS

Permanent-displacement models are commonly used to create seismic landslide hazard maps. These maps are used for emergency-preparedness and long-term land use planning, among other things. Areas of relative seismic landslide hazard (low, moderate, high, etc.) are typically demarcated based on specified thresholds of allowable displacement, or on a specified annual probability of exceedance. Creating regional hazard maps involves manipulating large sets of detailed spatial data within a Geographic Information System (GIS).

The use of GIS was recommended by Holden and Real (1990) as the most cost effective way to prepare regional-scale hazard maps, and it has since defined the state of practice. The increased availability of high-quality GIS data combined with powerful analytical tools has made it a robust research platform. The two most common types of GIS data are vector and raster data. Vector data are stored as points (pairs of x, y coordinates), lines (a sequence of points), or polygons (a closed set of lines). This type of data is well-suited for locating discrete values or boundaries between data sets. Raster data represent continuous areas and are characterized by raster cells (i.e. a grid).

When geographically-referenced layers of slope angle, soil shear strength, and earthquake ground shaking are imported into a GIS as raster data, estimates of yield acceleration and sliding displacement can be computed and assigned to each raster cell. The typical resolution of raster data used in seismic landslide hazard mapping is 10 meters, which means that a 100-km$^2$ area can be characterized by one million unique

cells (and thus one million unique values of yield acceleration and displacement). In order to turn maps of yield acceleration or displacement into maps of seismic landslide hazard, thresholds must be established that relate ranges of yield acceleration or displacement values to different hazard levels. These thresholds depend on many factors that are project-specific.

The two organizations that do the most work mapping earthquake-induced landslides within the United States are the California Geological Survey (CGS) and the United States Geological Survey (USGS). Each organization has adopted a different approach to seismic landslide hazard mapping, although both are based on displacements predicted for a rigid sliding block.

### 2.3.1 CGS Approach

Following the 1989 Loma Prieta ($M_w = 6.9$) earthquake outside of San Francisco, the Seismic Hazards Mapping Act of 1990 was adopted by the California legislature (Public Resources Code, Section 2690-2699.6). The Seismic Hazards Mapping Act directs the California Geological Survey (CGS) to delineate Seismic Hazard Zones for strong ground shaking, soil liquefaction, and landslides. In accordance with the Seismic Hazards Mapping Act, CGS published in 1997 a special publication entitled *Guidelines for Evaluating and Mitigating Seismic Hazards in California* that provides guidelines for identifying hazard zones where detailed investigations are required. The report was updated and re-issued in 2008.

The methodology adopted by CGS for creating earthquake-induced landslide hazard potential maps is based on a procedure proposed by McCrink and Real (1996). The procedure is based on developing yield acceleration thresholds that represent different levels of rigid sliding block displacement. The yield acceleration thresholds are based on the expected ground shaking within a given quadrangle. A single earthquake

strong-motion record is selected to be representative of the ground motion hazard for a particular quadrangle. Selection of the strong-motion record is based on the value of PGA that has a 10% probability of exceedance in 50 years, and the magnitude and distance combination that contributes most to the ground motion hazard (obtained from the deaggregation). The selected strong-motion record is used to calculate sliding displacement for a range of yield acceleration values, the relationship between displacement and $k_y$ is plotted (Figure 2.5), and the thresholds identified.

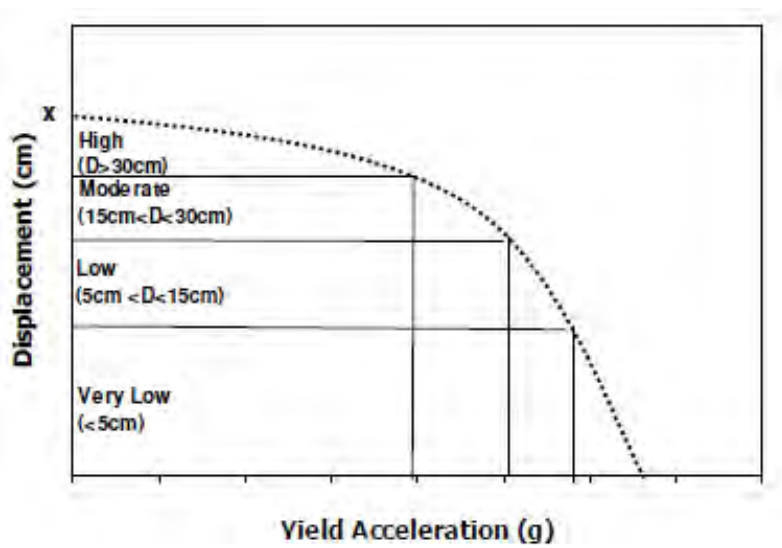


Figure 2.5: Plot of sliding displacement as a function of yield acceleration for a selected strong-motion record (Saygili, 2008)

As shown in Table 2.2, CGS has defined different displacement levels that represent different landslide hazard levels. Using the sliding displacement-yield acceleration plot, yield acceleration thresholds are identified that represent the landslide hazard levels for the selected ground motion.

Table 2.2: Landslide hazard displacement thresholds used by CGS

| **Landslide Hazard** | **Sliding Displacement (cm)** |
|---|---|
| Very Low | < 5 cm |
| Low | 5 cm < D < 15 cm |
| Moderate | 15 cm < D < 30 cm |
| High | D > 30 cm |

The resulting yield acceleration thresholds are compared (within a GIS) with the gridded yield acceleration values computed throughout the quadrangle from the infinite slope model (i.e. equations 2.2 and 2.3) and used to assign an appropriate landslide hazard level. In equation 2.3, the CGS procedures assume unsaturated slope conditions ($m = 0$) and no shear strength contribution from cohesion ($c' = 0$). These assumptions are based on the results from McCrink and Real (1996) and McCrink (2001) that showed ignoring cohesion and setting $m = 0$ resulted in the best comparison with observed landslides from the Loma Prieta earthquake.

All cells that correspond to a sliding displacement of 5 cm or greater (i.e. Low, Moderate, High hazard levels) are defined as landslide hazard zones. In addition, CGS breaks down the results for each quadrangle in a hazard potential matrix, which shows how the assigned hazard levels vary with slope angle and friction angle. An example of a hazard potential matrix published for the Oat Mountain quadrangle in Los Angeles County is provided in Table 2.3. The shaded groups are included in the hazard zone map for the quadrangle.

Table 2.3: Hazard potential matrix for earthquake-induced landslides in the Oat Mountain 7.5-minute quadrangle (CDMG, 1997b)

| Geologic Material Group | MEAN PHI | SLOPE CATEGORY I 0-7 | II 8-29 | III 30-38 | IV 39-45 | V 46-49 | VI 50-53 | VII 54-55 | VIII 56-65 | IX 66-70 | X >70% |
|---|---|---|---|---|---|---|---|---|---|---|---|
| 1 | 38 | VL | VL | VL | VL | VL | VL | L | L | M | H |
| 2 | 32 | VL | VL | VL | L | L | M | M | H | H | H |
| 3 | 27 | VL | VL | L | M | H | H | H | H | H | H |
| 4 | 8 | M | H | H | H | H | H | H | H | H | H |

### 2.3.2 USGS Approach

The approach used by the USGS is based on a study conducted by Jibson et al. (1998, 2000) regarding the earthquake-induced landslides from the 1994 Northridge earthquake. Similar to the approach used by CGS, gridded yield acceleration values are calculated within a GIS using an infinite slope model and equations 2.2 and 2.3. However, unlike the CGS approach, values of cohesion are considered in the calculation ($c' \neq 0$). The ground motion hazard is also characterized differently. Rather than selecting a single representative strong-motion record and rigorously computing displacements for a range of yield acceleration values, a displacement prediction model is used to calculate displacements as a function of gridded yield acceleration values and gridded values of some ground motion parameters, commonly either peak ground acceleration ($PGA$) or Arias intensity ($I_a$). Values of ground shaking intensity that have a 2% and 10% probability of exceedance are considered.

After displacements are calculated for the two ground motion hazard levels, ranges of displacement are assigned to different landslide hazard categories, as shown in Table 2.4. In addition, each hazard category is assigned a probability of landsliding based on an equation developed by Jibson et al. (1998, 2000) that calculates the probability of

landsliding as a function of predicted displacement. This procedure was recently used to produce landslide hazard maps for Anchorage, Alaska (Jibson and Michael, 2009).

Table 2.4: Landslide hazard displacement thresholds and associated probabilities of landsliding used by USGS

| Hazard Category | Displacement (cm) | Probability of Landsliding (%) |
|---|---|---|
| Low | 0 -1 | 0 - 2 |
| Moderate | 1 - 5 | 2 - 15 |
| High | 5 - 15 | 15 - 32 |
| Very High | > 15 | > 32 |

## 2.4 PREVIOUS VALIDATION STUDIES

For the sliding block analysis to be useful in evaluating the potential for earthquake-induced landslides, values of calculated yield acceleration and/or displacement must be quantitatively correlated with observations of landslides from previous earthquakes. This comparison can be made within the GIS framework. Similar to the information for slope angle, shear strength, and ground motion data that are used as input into displacement prediction models, locations of observed landslides are also imported into a GIS as raster data. A cell that falls within a mapped landslide area is assigned a numerical value that identifies it as part of that particular landslide; non-landslide cells are assigned “null” values. Values of yield acceleration or displacement can be compared with locations of landslide cells, and different predictive models or sets of model parameters can be assessed based on how well they predict the locations of the landslides. Two of the most comprehensive validation exercises for mapping earthquake-induced landslide hazards were performed by Jibson et al. (2000) for 1994 Northridge earthquake and McCrink (2001) for the 1989 Loma Prieta earthquake.

Both studies compiled information using a GIS platform and created regional maps of predicted displacements to compare with maps of known earthquake-induced landslides.

### 2.4.1 Jibson et al. (2000)

Jibson et al. (2000) considered six quadrangles in the Santa Susana Mountains north of Los Angeles, California that were shaken by the 1994 Northridge earthquake. This was the first earthquake for which a comprehensive data set of slope and soil information, ground shaking, and observed landsliding was available to permit a detailed regional analysis. The study area covered nearly 1,000 square kilometers, and more than 7,000 landslides were documented within that area, covering approximately 16 square kilometers or 1.6% of the six quadrangles. All data used in the study were imported into a GIS platform and converted to layers of gridded raster data at 10-meter cell spacing.

Jibson et al. (2000) calculated values of yield acceleration for each 10-meter cell using equations 2.2 and 2.3 from an infinite slope model. Slope angles were calculated from Digital Elevation Models (DEM) that were derived from scanned U.S. Geological Survey contour plates, and soil shear strength parameters ($c', \varphi'$) were determined based on the results of direct-shear tests from local geotechnical consultants on samples of geologic units in the region. Before calculating displacements, shear strengths were increased incrementally until all cells were statically stable (FS > 1.0). Importance was placed on keeping relative strength differences between geologic units intact. The values of $c'$ and $\varphi'$ used by Jibson et al. (2000) are shown in Table 2.5.

Table 2.5: Shear strengths assigned by Jibson et al. (2000) to geologic units in the study area[a]

| Unit name (description) | Oat Mountain | Santa Susana | Simi Valley | Newhall | Val Verde | Piru | ϕ' (°) | *c'* (kPa) |
|---|---|---|---|---|---|---|---|---|
| Artificial fill | af | | af | af | af | af | 34 | 16.8 |
| Artificial cut and fill | acf | | | | | | 34 | 16.8 |
| Rockfall deposits | rf | | | | | | 34 | 16.8 |
| Spoil from quarries | Qsp | | | | | | 34 | 16.8 |
| Alluvium ( young) | Qay | | | | | | 34 | 16.8 |
| Pond deposits | Qp | | | Ql | | | 34 | 16.8 |
| Flood plain deposits | | | | | | Qfp | 34 | 16.8 |
| Alluvium | Qal | Qal | Qal | Qal (1,2) | Qal | Qal | 34 | 16.8 |
| Older alluvium | Qao | Qao | Qao | Qao | Qao | Qao | 34 | 16.8 |
| Slope wash | Qsw | Qsw | | Qsw | | | 34 | 19.2 |
| Caliche | Qc | | | Qc? | | | 34 | 16.8 |
| Landslide deposits | Qls | Qls | Qls | Qls | Qls | Qls | 30 | 24.0 |
| Terrace deposits | Qt | Qt | Qt | Qt | Qt | Qt | 34 | 16.8 |
| Fan and terrace deposits | | Qft | | | Qf | Qf | 34 | 16.8 |
| Pacoima Fm. (ss/cg ) | | | | Qpa | | | 34 | 19.2 |
| Older terrace deposits | Qto | | | Qto | | | 34 | 16.8 |
| Old fanglomerate | | | | Qfo | | | 34 | 16.8 |
| Saugus Fm. | QTs | Qs | Qs | Qs | Qs | Qs | 34 | 19.2 |
| Upper Member (silty breccia) | QTsu | | | | | | 34 | 21.6 |
| Lower Member/Sunshine Ranch Fm. | QTsm | Qsm | Qsm | | | | 34 | 21.6 |
| Saugus ( Pelona Schist clasts) | | | | Qsp | Qsp | | 34 | 19.2 |
| Saugus (San Francisquito clasts) | | | | Qss | Qss | | 34 | 19.2 |
| Pico Fm. | Tp | QTp | QTp | | Tp | Tp | 32 | 24.0 |
| Pico Fm. (?) | Tp? | | | | | | 34 | 24.0 |
| Pico Fm. (ss/cg) | Tpc | QTpc | | Tpc | Tpc | Tpc | 34 | 24.0 |
| Pico Fm. (silt ) | Tps | QTps | | Tps | Tps | Tps | 30 | 24.0 |
| Towsley Fm. (ss/shale) | Tw | Tw | | | | | 34 | 26.3 |
| Towsley Fm. (shale) | Tws | Tws | | Tws | Tws | Tws | 30 | 26.3 |
| Towsley Fm. (ss) | Twc | Twc | | Twc | Twc | Twc | 34 | 26.3 |
| Hasley Conglomerate | | | | | Twhc | Twhc | 34 | 24.0 |
| Castaic Fm. (ss) | | | | Tcs | Tcs | | 34 | 19.2 |
| Mint Canyon Fm. (ss) | | | | Tmc | | | 34 | 19.2 |
| Mint Canyon Fm. (ss/clay) | | | | Tmcl | | | 32 | 19.2 |
| Modelo Fm. (shale) | Tm | Tm | Tm | | | Tm | 31 | 26.3 |
| Modelo Fm. (shale/mud ) | Tm1 | | Tm1 | | | Tm1 | 31 | 26.3 |
| Modelo Fm. ( porc. shale) | Tm2 | Tm2 | Tm2 | | | Tm2 | 31 | 26.3 |
| Modelo Fm. (ss) | Tm3 | Tm3 | Tm3 | | | Tm3 | 34 | 26.3 |
| Modelo Fm. (shale) | Tm4 | Tm4 | Tm4 | | | Tm4 | 31 | 26.3 |
| Modelo Fm. (shale) | | | | | | Tm5 | 31 | 26.3 |
| Modelo Fm. (diatom. shale) | Tmd | Tmd | | | | | 31 | 26.3 |
| Modelo Fm. (shale) | Tms | | | | Tms | | 31 | 26.3 |
| Modelo Fm. (cg/ss) | | | | | Tmc | | 34 | 26.3 |
| Topanga Fm. (ss) | Tt | Tt | Tt | | | | 34 | 26.3 |
| Topanga Fm. ( basalt ) | Ttb | Ti | | | | | 34 | 33.5 |
| Topanga Fm. (shale) | Tt1 | | | | | | 31 | 28.7 |
| Topanga Fm. (ss) | Tt2 | | | | | | 34 | 26.3 |
| Topanga Fm. (shale) | Tt3 | | | | | | 31 | 28.7 |
| Topanga Fm. (ss) | Tt4 | | | | | | 34 | 26.3 |
| Conejo Volcanics (andesite/basalt) | | | Tco | | | | 40 | 40.7 |
| Conejo Volcanics (andesite) | | | Tcoa | | | | 40 | 43.1 |
| Conejo Volcanics ( basalt) | | | Tcob | | | | 40 | 38.3 |
| Rincon Shale | | | | | | Trn | 30 | 19.2 |
| Vaqueros Fm. (silt, ss) | | | Tv | | | Tv | 33 | 28.7 |
| Sespe Fm. (ss, cg) | | Ts | Ts | | | Ts | 33 | 26.3 |
| Llajas Fm. (ss, silt, clay, cg) | Tl | Tl | Tl | | | | 33 | 28.7 |
| Llajas Fm. (calc. ss, hard ) | Tlc | Tlc | | | | | 36 | 43.1 |
| Santa Susana Fm. (clay shale) | Tss | Tss | | | | | 30 | 33.5 |
| Simi Conglomerate | | Tsc | | | | | 34 | 40.7 |
| Simi Conglomerate (cg) | Tsc1 | | | | | | 34 | 40.7 |
| Simi Conglomerate (shale) | Tsc2 | | | | | | 30 | 33.5 |
| Simi Conglomerate (ss) | Tsc3 | | | | | | 34 | 38.3 |
| Chatsworth Fm. (ss) | Kc | Kc | | | | | 40 | 47.9 |

a φ': effective angle of internal friction; c': effective cohesion intercept; ss: sandstone; cg: conglomerate; 1 kPa = 20.885 lb/ft$^2$.

Rigid sliding block displacements for the Jibson et al. (2000) study were calculated using the following displacement prediction equation, derived from a database of 555 acceleration-time histories from 13 worldwide earthquakes:

$$\log D = 1.521 \log I_a - 1.993 \log k_y - 1.546 \tag{2.6}$$

where $D$ is displacement in centimeters, $I_a$ is Arias intensity in meters per second, and $k_y$ is yield acceleration in units of g. The equation was regressed on two predictor variables: yield acceleration values (which ranged from 0.02 to 0.40 $g$), and Arias intensity values calculated for each acceleration-time history. To calculate displacements for the Northridge earthquake, a ground shaking grid from the earthquake was prepared. For each of the 189 strong-motion recordings of the main shock, the average Arias intensity from the two horizontal components was computed and plotted at the location of the strong motion station. A simple kriging algorithm was then used to interpolate values of $I_a$ to each 10-meter cell across the six quadrangles. Figure 2.6 shows the contours of Arias intensity throughout the study area based on calculated and interpolated values. Values range from less than 1 m/s in the northwest corner to greater than 5 m/s in the southeast corner, which is closest to the Northridge earthquake epicenter.

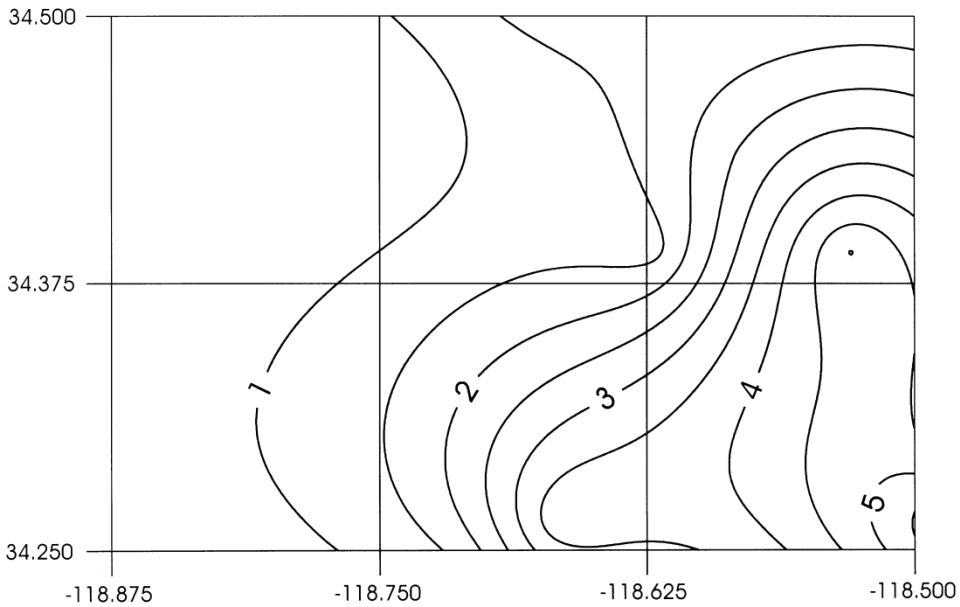


Figure 2.6: Contours of Arias intensity ($I_a$) in meters per second in six quadrangles studied by Jibson et al. (2000) and shaken by the 1994 Northridge earthquake (Jibson et al., 2000)

Maps of predicted displacement (Figure 2.7) were then compared with maps of observed landslides (Figure 2.8). Observed landslides were digitized by Harp and Jibson (1995, 1996) using high-resolution aerial photographs taken by the U.S. Air Force the morning of the earthquake and converted to 10-meter raster grids. Landslide source areas were defined by Jibson et al. (2000) as those grid cells having elevations above the median elevation for each landslide, so that the upper half of each landslide was considered a source area.

Figure 2.7 shows the displacements predicted in a section of the Oat Mountain quadrangle using the procedure described above. The largest displacements, represented by the darker red areas, are concentrated along steeper ridges north of Interstate 5. Figure 2.8 shows the observed landslides triggered by the Northridge earthquake over the same area. These landslides are also concentrated to the north of Interstate 5, although they appear to represent a larger area than the large-displacement cells from Figure 2.7.

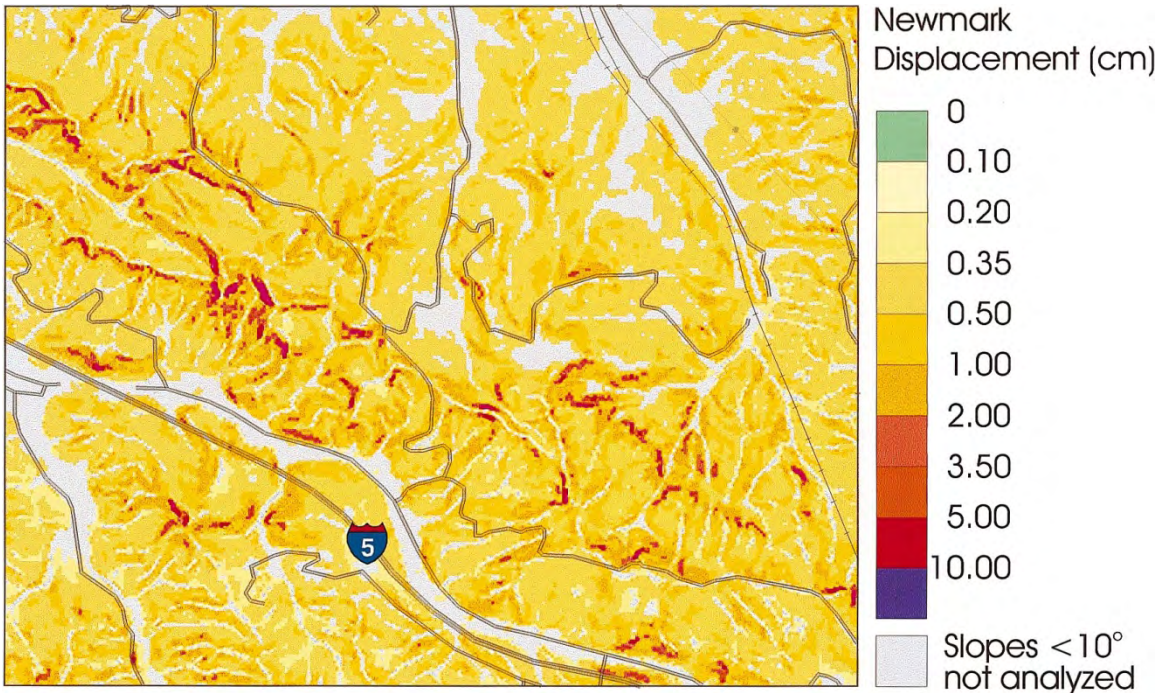


Figure 2.7: Predicted displacements in part of the Oat Mountain quadrangle (Jibson et al., 2000)

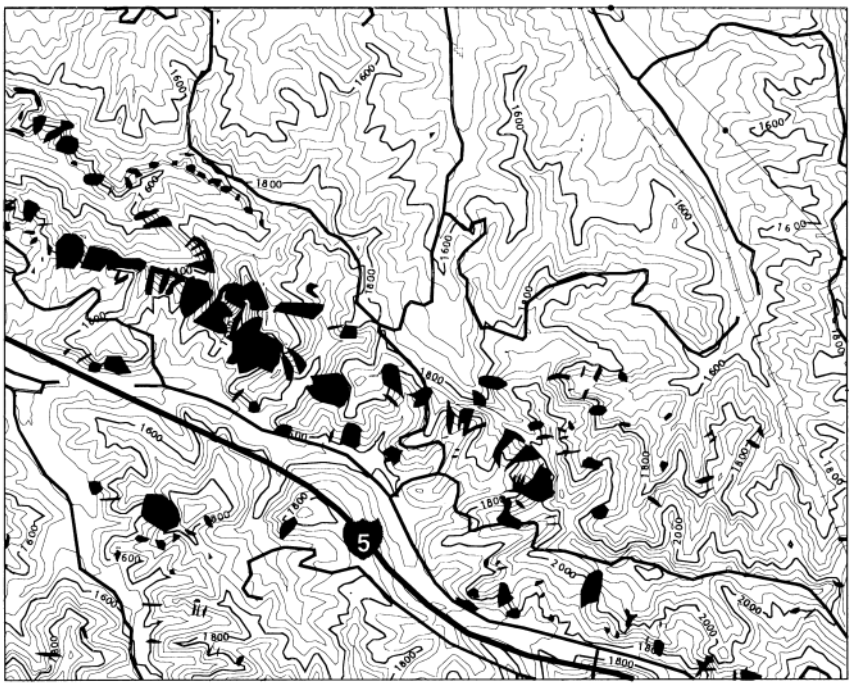


Figure 2.8: Landslides triggered in part of the Oat Mountain quadrangle (Jibson et al., 2000)

To quantitatively assess the accuracy of computed sliding displacements in predicting earthquake-induced landslides, Jibson et al. (2000) evaluated a probability of failure ($P_f$) for different displacement levels. Probability of failure was defined as the proportion of cells occupied by landslide source cells for a specified range of displacement. For example, for a displacement bin centered around 10 cm, only the cells with predicted displacements within that bin are considered. The number of landslide source cells within the identified 10 cm cells is divided by the total number of 10 cm cells to compute $P_f$. Figure 2.9 shows the data derived from the analysis and the equation that was fit to the data.

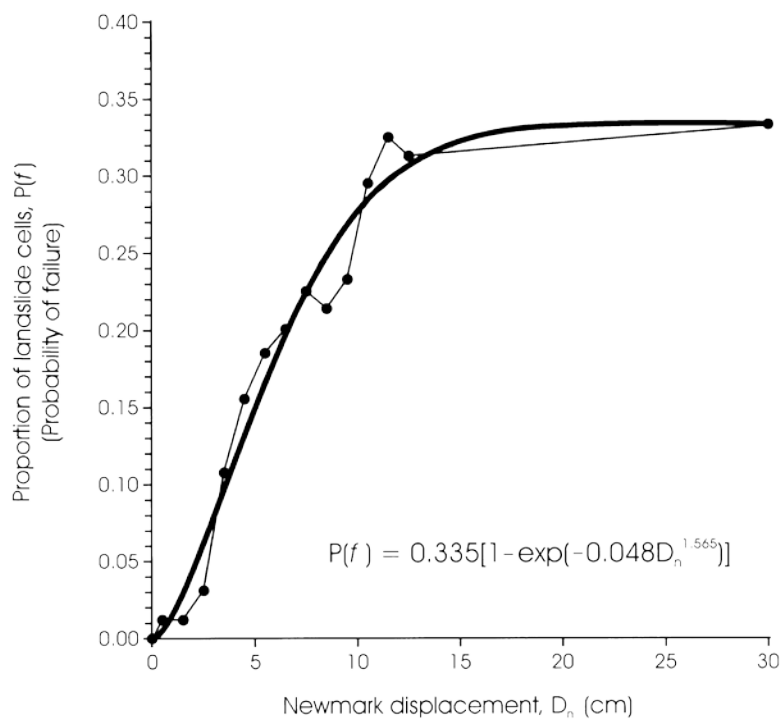


Figure 2.9: Proportion of landslide source cells as a function of displacement (Jibson et al., 2000)

Figure 2.9 shows that the probability of failure never exceeds about 34% even at very large displacements, suggesting that no more than 34% of high landslide hazard areas are likely to experience failure during an earthquake. Jibson et al. (2000) used this equation to create hazard maps showing the probability of slope failure as a function of predicted displacement.

### 2.4.2 McCrink (2001)

Earthquake-induced landslides from the 1989 Loma Prieta earthquake near San Francisco, California were used to validate a seismic hazard mapping procedure developed by McCrink (2001). This procedure was adopted by the California Geological Survey for preparing seismic hazard zone maps throughout California. The validation exercise was conducted using data collected from a quadrangle in the Santa Cruz Mountains. The data were combined within a GIS platform and converted to layers of gridded raster data at 10-meter cell spacing.

Values of yield acceleration were calculated for each cell using equations 2.2 and 2.3 for an infinite slope model, just as Jibson et al. (2000) had done. Geologic material strength values were compiled from laboratory test results found in reports on file with the Santa Cruz County Planning Department. To characterize the expected ground shaking within the quadrangle, a single representative strong-motion record from the Loma Prieta earthquake was used. The selected record was from the Corralitos station, and produced a peak horizontal ground acceleration ($PGA$) of 0.64g during the Loma Prieta earthquake. This record was used to compute sliding displacements for a range of typical yield accelerations, and different $k_y$-displacement thresholds were established (Figure 2.10).

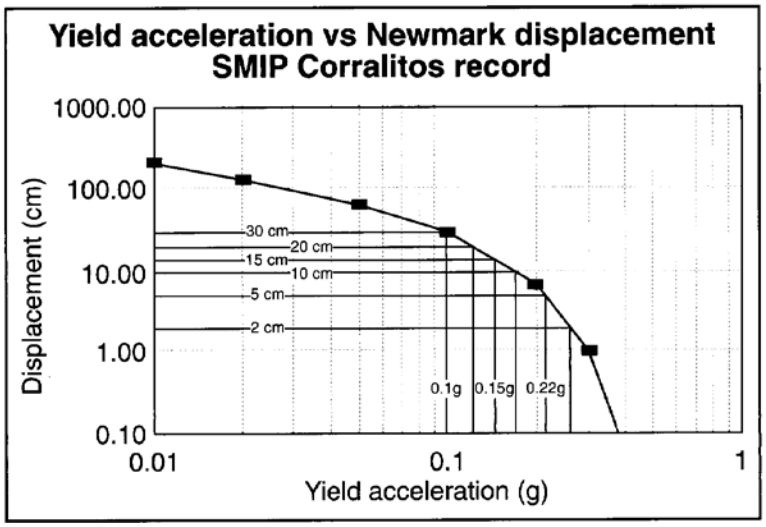


Figure 2.10: Yield acceleration versus sliding displacement for the Corralitos strong-motion record from the 1989 Loma Prieta earthquake (McCrink, 2001)

After a relationship between yield acceleration and predicted displacement was established for the expected ground shaking in the quadrangle, McCrink (2001) calibrated the mapping procedure to find the optimal set of model parameters that would maximize the number of landslides captured, while minimizing the area included in the hazard zone. Values of $c', \varphi'$, the thickness of the failure mass ($t$), and the saturation thickness ($m$) were varied in the analyses. Different combinations of displacement thresholds at 2, 5, 10, 15, 20 and 30 cm were also considered.

McCrink (2001) established an efficiency parameter to quantitatively compare the accuracy of different parameter sets. Efficiency was defined as the difference between the percentage of landslides accurately identified (GFC = % Ground Failure Capture) and the percentage of the entire quadrangle identified as a seismic hazard zone (QC = % Quadrangle Covered). Using this efficiency parameter (Efficiency = %GFC - %QC) rather than just using % GFC to judge the accuracy of different parameter sets prevented the identification of the optimal parameters based on a scenario where a 100% of the

landslides were accurately identified (i.e. GFC = 100%) because 100% of the quadrangle was covered by landslide zones (i.e. QC = 100% and efficiency is zero).

Figure 2.11 shows the plot of efficiency (i.e. percent difference) and % GFC calculated for each parameter set by McCrink (2001). Instead of selecting the optimum parameter set (i.e. the maximum efficiency), McCrink (2001) decided to compromise on efficiency to include more ground failures. The chosen best parameter set is indicated on the plot, capturing approximately 84% of the Loma Prieta slope failures within the quadrangle, while covering approximately 50% of the quadrangle with landslide hazard zones (i.e. an efficiency of 34%). The set of parameters that corresponded with these results was mean friction angle, no cohesion ($c' = 0$), unsaturated slope conditions ($m = 0$), and a displacement threshold of 5 centimeters (low, moderate and high landslide potential).

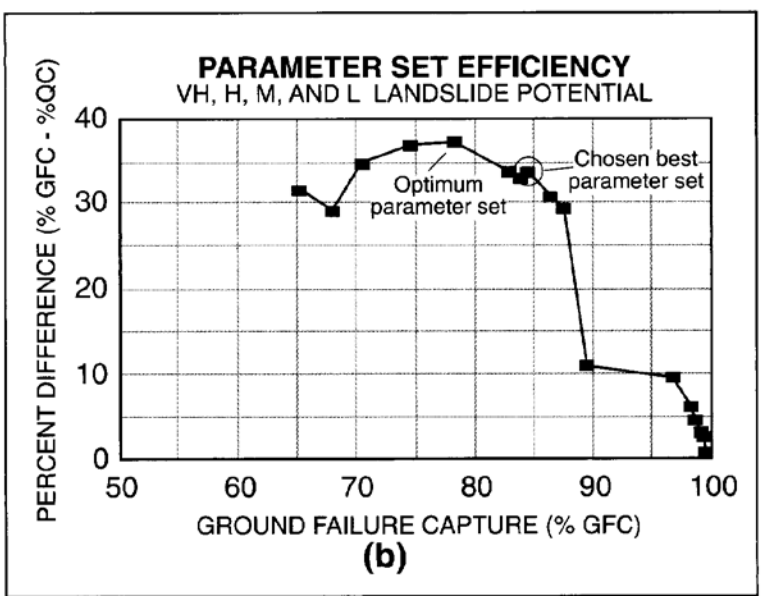


Figure 2.11: Plot of efficiency versus ground failure capture for different combinations of model parameters (McCrink, 2001)

McCrink (2001) also summarized the results in a landslide potential matrix (Figure 2.12), which shows how the different hazard potential levels for the chosen parameter set are distributed as a function of geologic strength group and slope angle. Very Low (VL) hazard potential corresponds to displacements less than 5 cm, Low (L) to between 5 and 15 cm, Moderate (M) to between 15 and 30 cm, and High (H) to greater than 30 cm. The shaded areas represent the hazard potential levels (L, M, H) included in the seismic hazard zone (i.e. all areas with displacements greater than 5 cm).

| Geologic material group | SLOPE CATEGORY I 0-4% | II 5-9% | III 10-20% | IV 21-27% | V 28-31% | VI 32-37% | VII 38-42% | VIII 43-50% | IX 51-58% | X 59-63% | XI >63% |
|---|---|---|---|---|---|---|---|---|---|---|---|
| A | VL | VL | VL | VL | VL | VL | VL | VL | L | M | H |
| B | VL | VL | VL | VL | L | L | M | H | H | H | H |
| C | VL | VL | VL | L | M | H | H | H | H | H | H |
| D | L | M | H | H | H | H | H | H | H | H | H |

Parameters used:
$\phi$ = Mean
c = 0
H = N/A
Displacement / Landslide potential criteria = 5, 15, and 30 cm

Capture Efficiency:
Ground failures captured = 84.2%
% of quadrangle covered (H, M, and L) = 50.3%
GFC - QC = 33.9%

Figure 2.12: Landslide potential matrix for the chosen best parameter set for Laurel quadrangle (McCrink, 2001)

## 2.5 SUMMARY

Permanent displacement analysis has become a common procedure for evaluating the seismic performance of slopes. Appropriate for modeling shallow, infinite slope failures, the results of a rigid-block permanent displacement analysis can be used to develop maps of seismic landslide susceptibility or hazard. The magnitude of predicted displacement is sensitive to variations in yield acceleration, and to the intensity, frequency content and duration of the expected earthquake ground motions. Recent research has led to the development of empirical predictive models that estimate displacements as a function of one or more ground motion parameters. These models provide a simple, powerful tool for conducting large-scale, regional analyses.

Comprehensive validation exercises have been performed for some of the early procedures adopted for the evaluation of earthquake-induced landslides. As research continues to yield advances in predictive modeling, these efforts must be validated against past earthquakes and compared with previous methodologies.

# Chapter 3

# Validation Approach for the Northridge Earthquake

## 3.1 INTRODUCTION

This chapter describes the validation exercises performed in this study. The validation is based on comparing locations of observed landslides induced by a previous earthquake with sliding-block displacements predicted by various empirical models. Six quadrangles located in the Santa Susana Mountains north of Los Angeles, California are selected as the study area for this exercise. This study area was chosen based on the availability of a comprehensive landslide inventory from the 1994 Northridge earthquake.

The workflow and data used in this study is similar to the validation exercise performed by Jibson et al. (2000). This chapter describes the data and assumptions used to calculate yield accelerations, the different empirical models used to calculate sliding displacements, the ground motion information for the study area, and the procedures used for mapping and assessing the accuracy of the results. Results are presented in the next chapter. All data in this study were converted to 10-meter raster grids and all

computations were performed using ArcGIS© 9.3 software developed by the Environmental Systems Research Institute (ESRI).

## 3.2 NORTHRIDGE EARTHQUAKE STUDY AREA

Six quadrangles located in the Santa Susana Mountains north of Los Angeles, California were used for the validation study. These six quadrangles – Piru, Val Verde, Newhall, Simi Valley, Santa Susana, and Oat Mountain – are the same quadrangles that Jibson et al. (2000) evaluated previously. The locations of the quadrangles are shown in Figure 3.1. These quadrangles were studied by Jibson et al. (2000) because of the dense concentration of landslides triggered during the 1994 Northridge earthquake, and because the study area was large enough to encompass significant variations in ground shaking. A map of the instrumental intensity of the Northridge earthquake (related to Modified Mercalli Intensities, MMI) produced by the USGS (Figure 3.2) shows that the study area is located just to the northwest of the earthquake epicenter in an area that experienced severe and violent shaking. Peak ground accelerations in the study area ranged from 0.2 to 0.9 g, and are discussed further in subsequent sections of this chapter.

The Northridge earthquake was the first earthquake for which all of the data sets necessary to conduct a detailed, regional seismic landslide hazard analysis were available. This includes (1) a comprehensive inventory of triggered landslides (Harp and Jibson 1995), (2) about 200 strong-motion records of the main shock recorded throughout the region, (3) detailed geologic maps, (4) extensive soil shear strength data, and (5) high resolution digital elevation models (Jibson et al. 2000).

Figure 3.1: Location of study area (Map obtained from the California Geologic Survey Seismic Hazard Zonation Program website available at http://www.conservation.ca.gov/cgs/shzp)

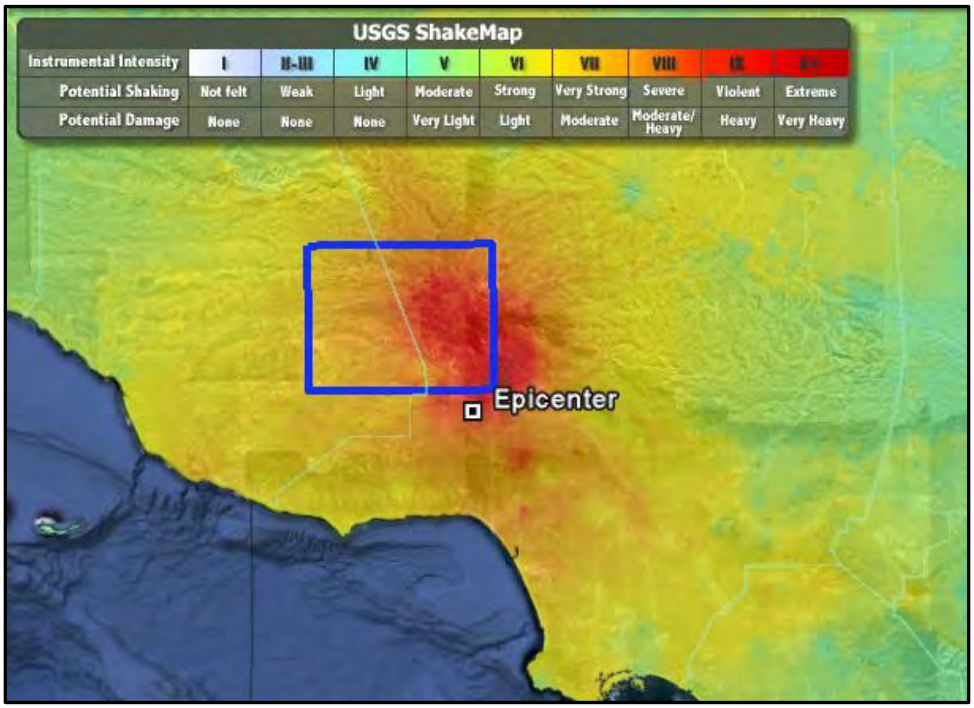


Figure 3.2: Map of instrumental intensity for the 1994 Northridge earthquake. The blue box represents the six quadrangles used in this study (Map created in Google Earth using data from the USGS ShakeMaps website available at http://earthquake.usgs.gov/earthquakes/shakemap/)

## 3.3 CALCULATING YIELD ACCELERATION

The first step of the validation exercise is calculating yield accelerations for the slopes within the study area. Similar to the procedures used by CGS and USGS, an infinite slope model is used to approximate conditions in the field and the pseudostatic force is assumed to act parallel to the slope (Figure 3.3).

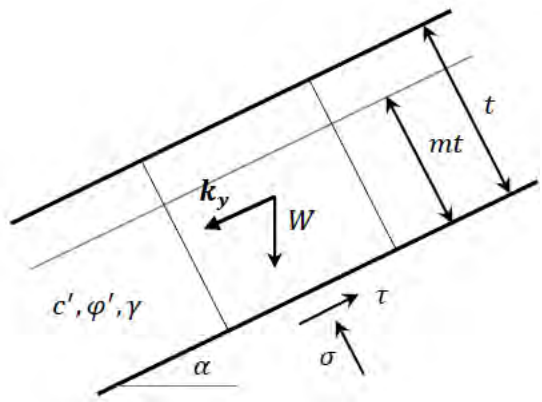


Figure 3.3: Infinite slope conditions for calculating yield acceleration

The equation for yield acceleration was derived in Chapter 2 for infinite slope conditions, and is shown again below:

$$k_y = (FS - 1)g \cdot sin\alpha \tag{3.1}$$

$$FS = \frac{c\prime}{\gamma t \sin\alpha} + \frac{\tan\varphi\prime}{\tan\alpha}\left(1 - m\frac{\gamma_w}{\gamma}\right) \tag{3.2}$$

where $k_y$ is the yield acceleration, $g$ is the acceleration due to gravity, FS is the static factor of safety, $\alpha$ is the slope angle, $c'$ is the effective cohesion, $\varphi'$ is the effective friction angle, $t$ is the slope-normal thickness of the rigid block, $\gamma$ is the material unit weight, $\gamma_w$ is the unit weight of water, and $m$ is the proportion of the block thickness that is saturated. For this study the contribution of pore water pressure is considered

negligible ($m = 0$) because almost all of the failures in the Northridge earthquake occurred in dry conditions (Jibson et al. 2000). In addition, to be consistent with previous research (Jibson et al. 2000) a unit weight of 15.7 kN/m$^3$ and a sliding-mass thickness of 2.4 m are assigned to represent a typical slope failure from the Northridge earthquake. The yield acceleration then becomes only a function of the shear strength parameters ($c'$, $\varphi'$) and the slope angle. These parameters for the quadrangles studied are discussed next.

### 3.3.1 Slope Angle

Maps of slope angle are computed for each quadrangle based on 10-meter resolution digital elevation models (DEM) provided by the USGS. The DEMs had been created from high-resolution scans of USGS contour plates. Slope angles (in degrees) are derived using a simple algorithm within ArcGIS© that computes the maximum difference in elevation between a given cell and neighboring cells. Figure 3.4 shows the digital elevation model and the calculated slope angles for the Oat Mountain quadrangle. The southern portion of the quad is very flat with most slopes less than 15°, while most of the hills to the north are between 25° and 45°. Some of the peaks visible in the DEM correspond to slope angles greater than 45°.

The distributions of slope angles within each quadrangle are compared in Figure 3.5. The Piru and Val Verde quadrangles in the northwest of the study area contain the greatest concentration of steep terrain; nearly 25% of the slopes in the Piru quadrangle are greater than 35°. In contrast, less than 3% of the slopes in the Newhall and Simi Valley quadrangles are steeper than 35°. The slope angle distributions of the neighboring Santa Susana and Oat Mountain quadrangles are very similar with about 10% of the slopes greater than 35°.

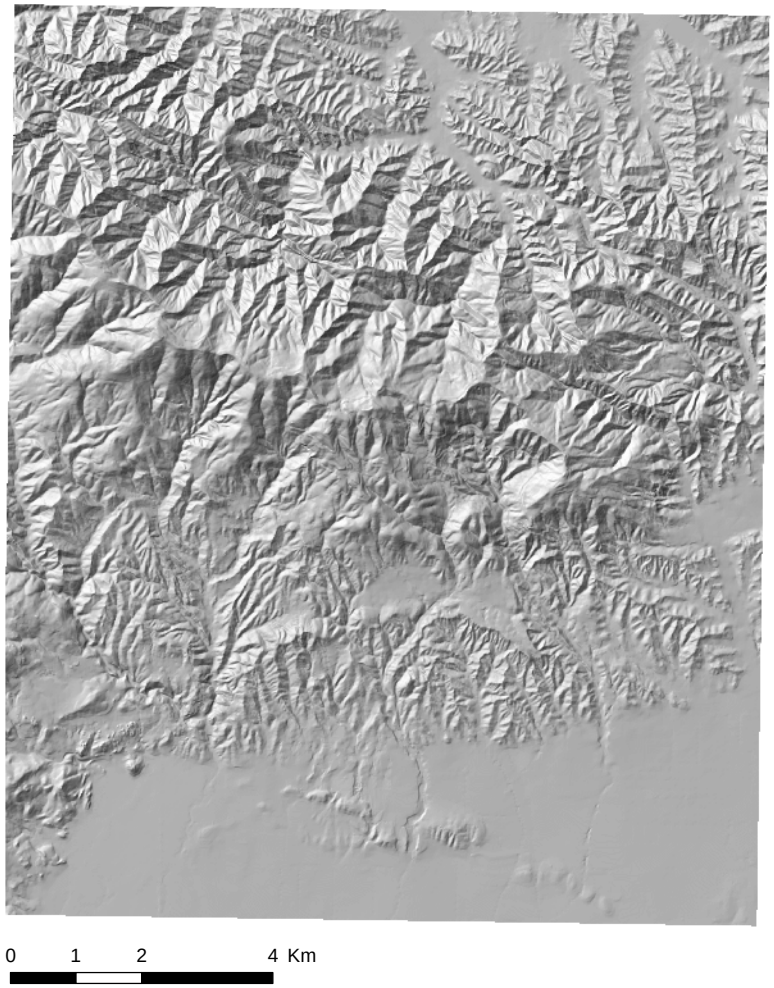


(a)

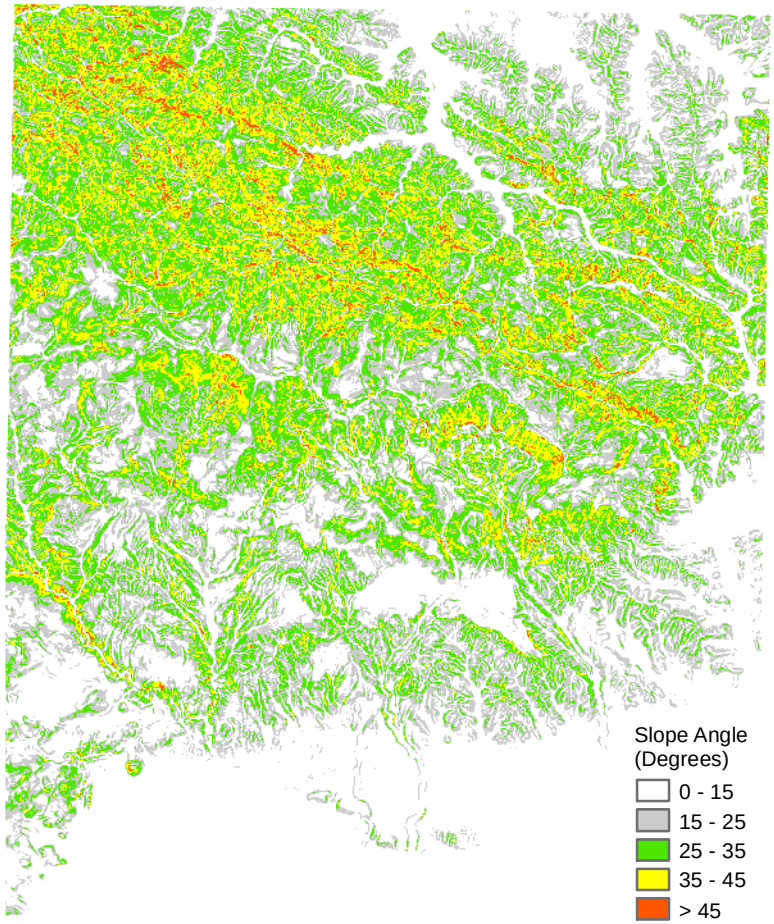


(b)

Figure 3.4: (a) Digital elevation model with hillshading and (b) map of slope angle values for the Oat Mountain quadrangle.

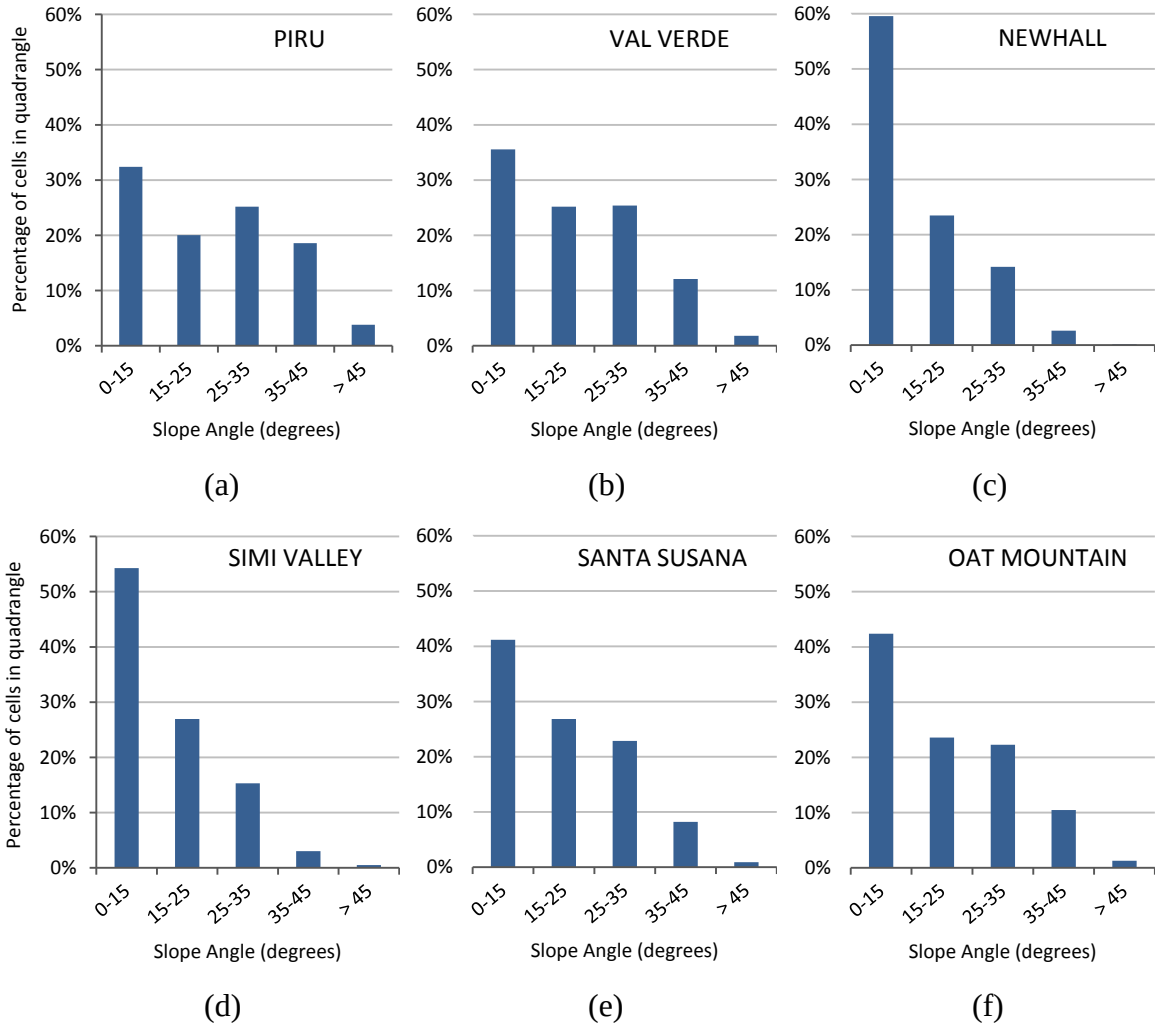


Figure 3.5: Distribution of slope angles for the (a) Piru, (b) Val Verde, (c) Newhall, (d) Simi Valley, (e) Santa Susana and (f) Oat Mountain quadrangles

Jibson et al. (2000) noted that slope angles greater than about 60° are generally under-represented in the dataset because of the difficulty in representing steep slopes on a contour plate. Other research on the use of digital elevation models has shown that practical applications of GIS-based models that rely on slope angle as a parameter can assume standard deviations of ± 3° to 4° (Haneberg, 2006). Despite these observations, DEM's are generally not a significant source of uncertainty when compared with the difficulties of estimating ground motions or assigning material properties.

### 3.3.2 Shear Strength Properties

Shear strength properties are developed based on assigning values of ($c'$, $\varphi'$) to mapped geologic units. The spatial distribution of geologic units across all six quadrangles is based on 1:24,000-scale geologic maps of Yerkes and Campbell (1995a-d, 1997a-b). The geologic map for the Oat Mountain quadrangle is shown in Figure 3.6. The legend identifies each geologic unit by the unit symbol; descriptions of these units are included later in this section. Comparing the geologic map with the digital elevation model in Figure 3.3, the low-lying areas in the northeast corner and bottom portion of the quadrangle consist of predominately Quaternary alluvial materials (Qal/Qay/Qp, Qao), and a large portion of the steeper, mountainous areas consist of Tertiary materials from the Modelo, Towsley and Pico formations (Tm, Tw, Tps respectively). The geologic maps for all six quadrangles are given in Appendix A (Figures A-1 through A-6).

Representative shear strengths were assigned to these geologic units based on the median values of ($c'$, $\varphi'$) published by the California Geological Survey (CGS) in their Seismic Hazard Reports for each quadrangle (CDMG 1997, 1997b, 1997c, CGS 2002, 2002b). Shear strength data were gathered by CGS primarily from geotechnical reports prepared by consultants on file with local government permitting departments. If shear test data were limited, test results from adjacent quadrangles were used to augment the data. CGS grouped geologic units together on the basis of average friction angle ($\varphi'$) and lithologic character. Each strength group was then assigned a single representative value of $\varphi'$ for use in stability analyses. CGS does not consider cohesion in their stability analyses ($c' = 0$) but mean and median values of $c'$were published in their reports. Shear strength groupings published by CGS for the Oat Mountain quadrangle are shown in Figure 3.6 as an example of the strength data used in this study.

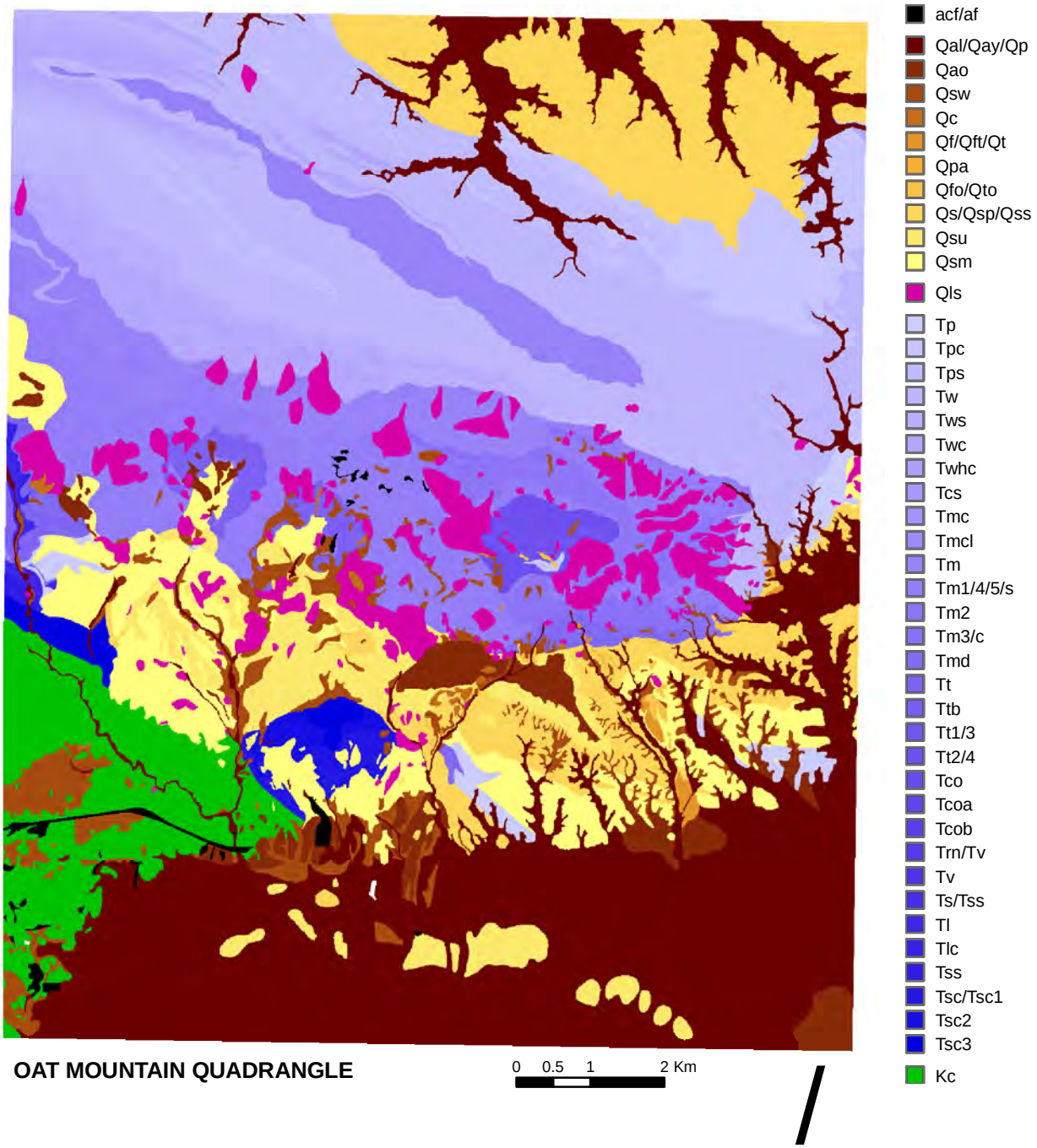


Figure 3.6: Map of geologic units within the Oat Mountain quadrangle, based on the geologic map of Yerkes and Campbell (1993, 1995).

**OAT MOUNTAIN QUADRANGLE**
**SHEAR STRENGTH GROUPINGS**

| | Formation Name | Number Tests | Mean/Median PHI | Group Mean/Median PHI (deg.) | Group Mean/Median Cohesion (psf) | No Data: Similar Lithology | Phi Values Used in Stability Analyses |
|---|---|---|---|---|---|---|---|
| GROUP 1 | Tt | 5 | 41.4/41 | 38.4/39.3 | 544/654 | Tm1-fbc, Tm2-fbc, Tm3-fbc,Tm4-fbc | 38 |
| | Tsc | 11 | 39.1/39 | | | Tmd-fbc, Tms-fbc, Tsc1, Tsc2-fbc | |
| | Tm-fbc | 7 | 39.0/39 | | | Tsc3, Tt1-fbc, Tt2, Tt3-fbc, Tt4, Ttb | |
| | Kc | 28 | 37.8/38 | | | Tlc, Tl-fbc, Tss-fbc | |
| GROUP 2 | Tpc/Tp-fbc | 5 | 33.0/32 | 31.9/32.8 | 376/278 | | 32 |
| | Twc/Tw-fbc | 2 | 34.0/34 | | | | |
| | Qs/Qsu | 85 | 32.0/33 | | | | |
| | Qsm-fbc | 13 | 31.9/33 | | | | |
| | Qvoa1/Qvof2 | 11 | 31.0/34 | | | | |
| | Qsw | 12 | 30.9/31 | | | | |
| GROUP 3 | Tps/Tp-abc | 4 | 27.8/28 | 27.3/28.3 | 390/410 | af, acf, rf, Qay, Qay1, Qay2, Qc, Qw | 27 |
| | Qsm-abc | 13 | 27.7/28 | | | Qt, Qao, Qto, Tws, Tw-abc, Tl-abc, | |
| | Qyf2/Qal | 9 | 28.1/30 | | | Tm-abc, Tm1-abc, Tm2-abc, Tm3-abc, | |
| | Qof1/Qoa | 17 | 25.5/26 | | | Tm4-abc, Tmd-abc, Tms-abc, Tt1-abc | |
| | Qyf1 | 7 | 29.0/30 | | | Tt3-abc, Tss-abc, Tsc2-abc | |
| GROUP 4 | Qls | 6 | 20.3/25 | 20.3/25 | 490/465 | | 8 |

abc = adverse bedding condition, fine-grained material strength
fbc = favorable bedding condition, coarse-grained material strength

Figure 3.7: Shear strength groups published in the CGS Seismic Hazard Report for Oat Mountain (CDMG, 1997b), available online at http://gmw.consrv.ca.gov/shmp/html/eval_rpts_so.html

The higher strength groups generally consist of well-cemented Tertiary rock units composed of sandstone and siltstone, limestone, shale and conglomerate. The lower strength groups predominately consist of loosely-consolidated quaternary deposits and previously identified landslide materials. For some geologic units CGS distinguishes between the strength under favorable bedding and adverse bedding conditions. This distinction depends on the angle of material bedding with respect to a horizontal plane (known as dip) and slope geometry. If the dip direction of a formation and the slope direction are roughly the same, adverse bedding conditions exist because a landslide can slip along the bedding surface. Orthogonal dip and slope directions are considered favorable bedding conditions. In general, CGS assumes that favorable bedding conditions are representative of coarse-grained (higher strength) lithologies, and adverse bedding

conditions are representative of fine-grained (lower strength) lithologies (CDMG, 1997b). In consultation with Dr. Randall Jibson from the USGS, only favorable bedding conditions were considered when selecting the appropriate shear strength values for this study because of the difficulty in identifying adverse bedding conditions on a regional scale (Jibson, personal communication).

The mapped shear strength groups for the Oat Mountain quadrangle are shown in Figure 3.8. The darkest shade of grey represents the strongest shear strength group (Group 1). The pink areas represent the previous landslide deposits (Group 4). Maps of shear strength groups for all six quadrangles are given in Appendix A (Figures A-7 through A-12).

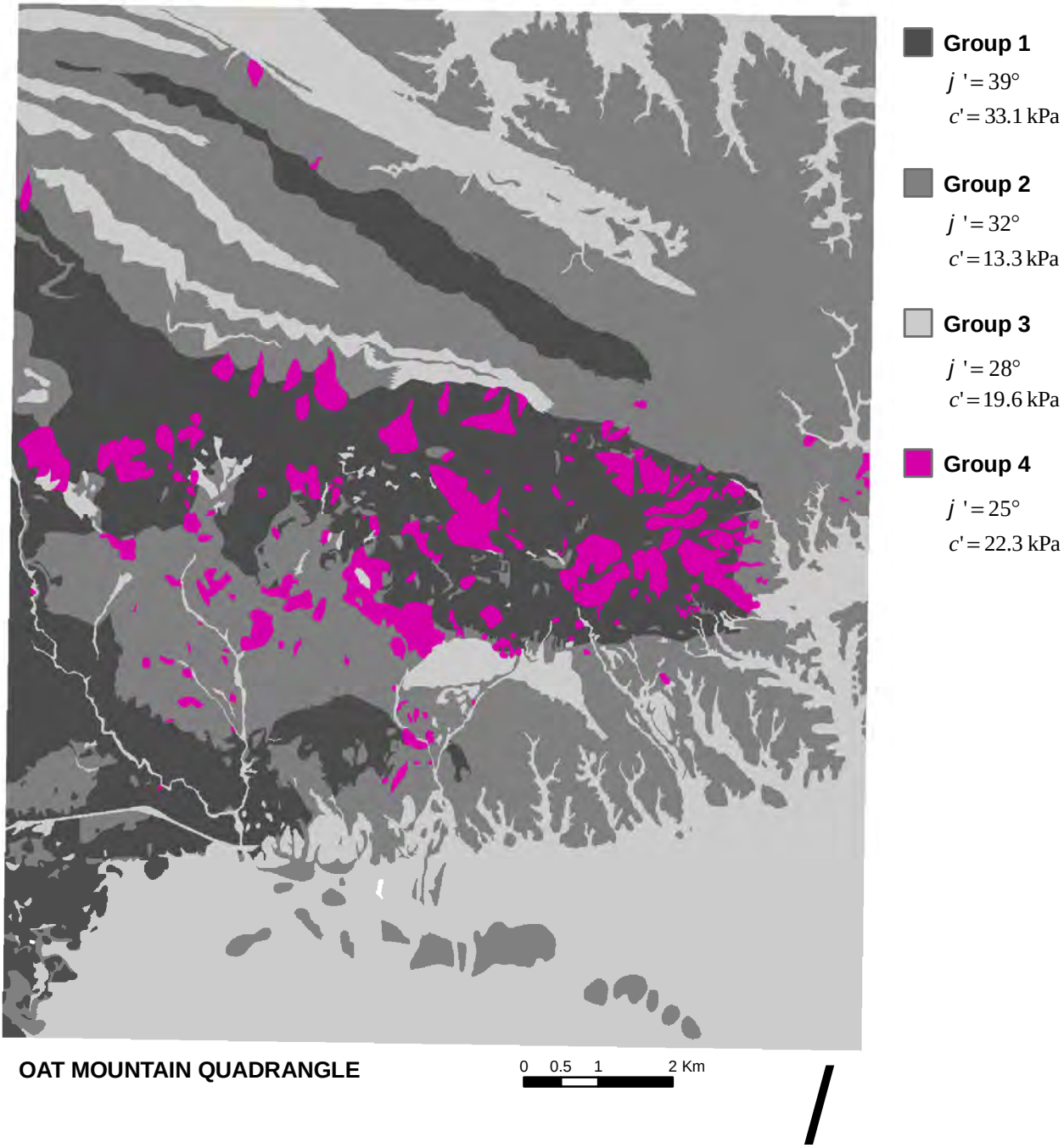


Figure 3.8: Map of shear strength groups within the Oat Mountain quadrangle based on the map of geologic units (Figure 3.6) and the shear strength values in Table 3.1

A summary of geologic units and assigned shear strengths for each quadrangle is provided in Table 3.1. Values for cohesion ($c'$) range from 12 to 35 kPa, and values for friction angle ($\varphi'$) range from 12° for previous landslide deposits (Qls) to 39° for the well-cemented tertiary units. The strength values in Table 3.1 are generally lower than those assigned by Jibson et al. (2000), and in some cases significantly lower. Values of $c'$assigned by Jibson et al. (2000) ranged from approximately 17 to 48 kPa and values of $\varphi'$ ranged from 30° to 40°. Jibson et al. (2000) started with median strengths compiled from direct-shear test results provided by local geotechnical consultants, and increased them incrementally until all slopes less than 60° were modeled as statically stable prior to earthquake shaking. This constraint resulted in large strengths being assigned to many geologic units in an effort to ensure that most steep slopes were statically stable. Jibson et al. (2000) believed that keeping intact the relative strength differences between geologic units was more important than the absolute values. However, this approach then overestimates the strength for an entire geologic unit if it contains some steep slopes. Because the strength of a material in an area with a steep slope is most likely stronger than the average value for that geologic unit, increasing the strength of the entire geologic unit results in overestimating the strength of the flatter slopes within that geologic unit. Therefore, for this study the median strength values were used throughout a geologic unit even if those strength parameters resulted in the steepest slopes being statically unstable within that unit.

In contrast, the approach used by CGS is to ignore any contribution from cohesion ($c' = 0$) in their stability analyses. For the same values of friction angle and slope angle, this results in a smaller yield acceleration (i.e. higher landslide susceptibility) and can be overly conservative. The influence of the assigned shear strength parameters on the yield acceleration is further explored in the next section.

Table 3-1: Shear strengths assigned in this study to geologic units in the six quadrangles of the study area

| Unit Name (description) | Type | Piru | | Val Verde | | Newhall | | Simi Valley | | Santa Susana | | Oat Mountain | |
|---|---|---|---|---|---|---|---|---|---|---|---|---|---|
| | | $\phi'$(°) | $c'$(kPa) | $\phi'$(°) | $c'$(kPa) | $\phi'$(°) | $c'$(kPa) | $\phi'$(°) | $c'$(kPa) | $\phi'$(°) | $c'$(kPa) | $\phi'$(°) | $c'$(kPa) |
| Artificial fill | af | 31 | 14.4 | 32 | 12.4 | 31 | 14.4 | 28 | 14.4 | | | 28 | 19.6 |
| Artificial cut and fill | acf | | | | | | | | | | | 28 | 19.6 |
| Rockfall deposits | rf | | | | | | | | | | | 28 | 19.6 |
| Alluvium (young) | Qay | | | | | | | | | | | 28 | 19.6 |
| Pond deposits | Qp | | | | | | | | | | | 28 | 19.6 |
| Flood plain deposits | Qfp | 31 | 14.4 | | | | | | | | | | |
| Alluvium | Qal | 31 | 14.4 | 32 | 12.4 | 31 | 14.4 | 28 | 14.4 | 28 | 14.4 | 28 | 19.6 |
| Older alluvium | Qao | 25 | 34.7 | 32 | 12.4 | 31 | 14.4 | 28 | 14.4 | 28 | 14.4 | 28 | 19.6 |
| Slope wash | Qsw | | | | | 31 | 14.4 | | | 28 | 14.4 | 32 | 13.3 |
| Caliche | Qc | | | | | 31 | 14.4 | | | | | 28 | 19.6 |
| Landslide deposits | Qls | 12 | 14.1 | 13 | 15.6 | 25 | 12.0 | 23 | 22.5 | 23 | 22.5 | 25 | 22.3 |
| Terrace deposits | Qt | 31 | 14.4 | 32 | 12.4 | 31 | 14.4 | 28 | 14.4 | 28 | 14.4 | 28 | 19.6 |
| Fan and terrace deposits | Qf/Qft | 31 | 14.4 | 32 | 12.4 | | | | | 28 | 14.4 | | |
| Pacoima Fm. (ss/cg) | Qpa | | | | | 31 | 14.4 | | | | | | |
| Older terrace deposits | Qto | | | | | 31 | 14.4 | | | | | 28 | 19.6 |
| Old fanglomerate | Qfo | | | | | 31 | 14.4 | | | | | | |
| Saugus Fm. | Qs | 31 | 14.4 | 32 | 12.4 | 31 | 14.4 | 35 | 12.0 | 35 | 12.0 | 32 | 13.3 |
| Upper Member (silty breccia) | Qsu | | | | | | | | | | | 32 | 13.3 |
| Lower Member/Sunshine Ranch | Qsm | | | | | | | 35 | 12.0 | 35 | 12.0 | 32 | 13.3 |
| Saugus (Pelona Schist clasts) | Qsp | | | 32 | 12.4 | 31 | 14.4 | | | | | | |
| Saugus (San Francisquito clasts) | Qss | | | 32 | 12.4 | 31 | 14.4 | | | | | | |
| Pico Fm. | Tp | 31 | 14.4 | 32 | 12.4 | | | 35 | 12.0 | 35 | 12.0 | 32 | 13.3 |
| Pico Fm. (ss/cg) | Tpc | 31 | 14.4 | 32 | 12.4 | 31 | 14.4 | | | 35 | 12.0 | 32 | 13.3 |
| Pico Fm. (silt) | Tps | 25 | 34.7 | 28 | 20.1 | 31 | 14.4 | | | 23 | 19.2 | 28 | 19.6 |
| Towsley Fm. (ss/shale) | Tw | | | | | | | | | 35 | 12.0 | 32 | 13.3 |
| Towsley Fm. (shale) | Tws | 31 | 14.4 | 28 | 20.1 | 37 | 14.8 | | | 23 | 19.2 | 28 | 19.6 |
| Towsley Fm. (ss) | Twc | 31 | 14.4 | 32 | 12.4 | 37 | 14.8 | | | 35 | 12.0 | 32 | 13.3 |
| Hasley Conglomerate | Twhc | 31 | 14.4 | 32 | 12.4 | | | | | | | | |
| Castaic Fm. (ss) | Tcs | | | 28 | 20.1 | 37 | 14.8 | | | | | | |
| Mint Canyon Fm. (ss) | Tmc | | | | | 37 | 14.8 | | | | | | |
| Mint Canyon Fm. (ss/clay) | Tmcl | | | | | 37 | 14.8 | | | | | | |
| Modelo Fm. (shale) | Tm | 31 | 14.4 | | | | | 35 | 12.0 | 35 | 12.0 | 39 | 31.3 |
| Modelo Fm. (shale/mud) | Tm1 | 25 | 34.7 | | | | | 35 | 12.0 | | | 39 | 31.3 |
| Modelo Fm. (porc. shale) | Tm2 | 31 | 14.4 | | | | | 35 | 12.0 | 35 | 12.0 | 39 | 31.3 |
| Modelo Fm. (ss) | Tm3 | 31 | 14.4 | | | | | 35 | 12.0 | 35 | 12.0 | 39 | 31.3 |
| Modelo Fm. (shale) | Tm4 | 31 | 14.4 | | | | | 35 | 12.0 | 35 | 12.0 | 39 | 31.3 |
| Modelo Fm. (shale) | Tm5 | 31 | 14.4 | | | | | | | | | | |
| Modelo Fm. (diatom. shale) | Tmd | | | | | | | | | 35 | 12.0 | 39 | 31.3 |
| Modelo Fm. (shale) | Tms | | | 28 | 20.1 | | | | | | | 39 | 31.3 |
| Modelo Fm. (cg/ss) | Tmc | | | 28 | 20.1 | | | | | | | | |
| Topanga Fm. (ss) | Tt | | | | | | | 35 | 12.0 | 35 | 12.0 | 39 | 31.3 |
| Topanga Fm. (basalt) | Ttb | | | | | | | | | 28 | 14.4 | 39 | 31.3 |
| Topanga Fm. (shale) | Tt1 | | | | | | | | | | | 39 | 31.3 |
| Topanga Fm. (ss) | Tt2 | | | | | | | | | | | 39 | 31.3 |
| Topanga Fm. (shale) | Tt3 | | | | | | | | | | | 39 | 31.3 |
| Topanga Fm. (ss) | Tt4 | | | | | | | | | | | 39 | 31.3 |
| Conejo Volcanics (andesite/basalt) | Tco | | | | | | | 38 | 28.7 | | | | |
| Conejo Volcanics (andesite) | Tcoa | | | | | | | 38 | 28.7 | | | | |
| Conejo Volcanics (basalt) | Tcob | | | | | | | 38 | 28.7 | | | | |
| Rincon Shale | Trn | 31 | 14.4 | | | | | | | | | | |
| Vaqueros Fm. (silt, ss) | Tv | | | | | | | 35 | 12.0 | | | | |
| Sespe Fm. (ss, cg) | Ts | 34 | 13.8 | | | | | 35 | 12.0 | 35 | 12.0 | | |
| Llajas Fm. (ss, silt, clay, cg) | Tl | | | | | | | 35 | 12.0 | 35 | 12.0 | 39 | 31.3 |
| Llajas Fm. (calc. ss, hard) | Tlc | | | | | | | | | 35 | 12.0 | 39 | 31.3 |
| Santa Susana Fm. (clay shale) | Tss | | | | | | | | | 35 | 12.0 | 39 | 31.3 |
| Simi Conglomerate | Tsc | | | | | | | | | 35 | 12.0 | | |
| Simi Conglomerate (cg) | Tsc1 | | | | | | | | | | | 39 | 31.3 |
| Simi Conglomerate (shale) | Tsc2 | | | | | | | | | | | 39 | 31.3 |
| Simi Conglomerate (ss) | Tsc3 | | | | | | | | | | | 39 | 31.3 |
| Chatsworth Fm. (ss) | Kc | | | | | | | | | 38 | 28.7 | 39 | 31.3 |

a φ': effective angle of internal friction; c': effective cohesion intercept; ss: sandstone; cg: conglomerate; 1 kPa= 20.885 lb/ft$^2$.

### 3.3.3 Maps of Yield Acceleration

Values of slope angle and shear strength are used in Equations 3.1 and 3.2 to compute yield acceleration. Yield acceleration values were computed at 10-meter grid spacing across all six quadrangles based on the computed grids of slope angle and shear strength. Because yield acceleration is a function of the static factor of safety (FS) and is independent of the expected level of ground shaking, a map of yield acceleration is essentially a map of seismic landslide susceptibility. The effect of shear strength properties on the dynamic performance of a slope can be evaluated by comparing values of yield acceleration. Figure 3.9 below shows the distribution of yield acceleration values and static factors of safety across the Oat Mountain quadrangle for the cases considered in the preceding section:

(i) CASE I: Strengths used by Jibson et al. (2000)

(ii) CASE II: Strengths used in this study ($c'$ and $\varphi'$ from Table 3.1)

(iii) CASE III: CGS approach ($\varphi'$ from Table 3.1, $c' = 0$)

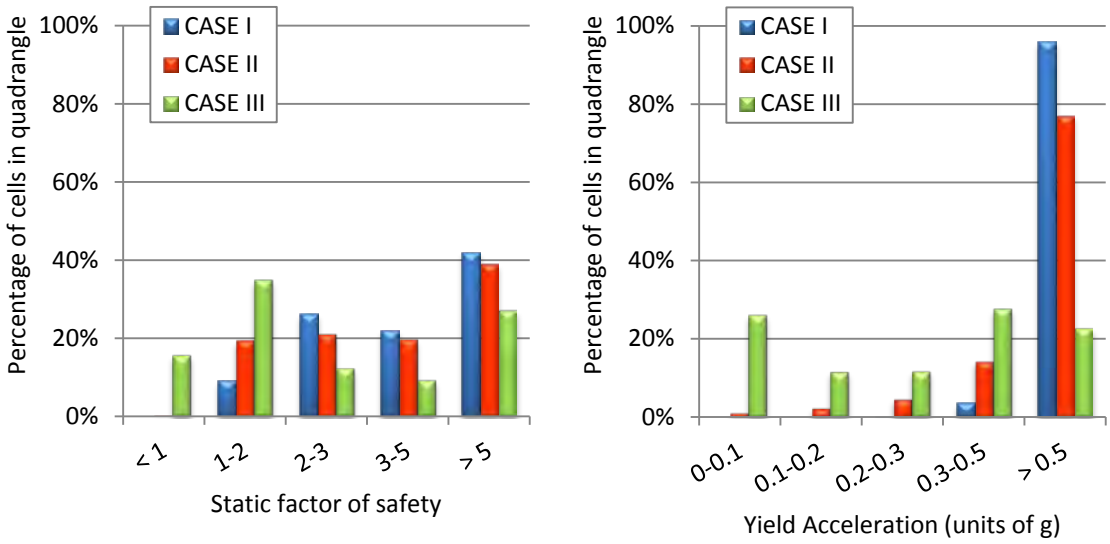


Figure 3.9: Distribution of values of a) factor of safety, and b) yield acceleration in the Oat Mountain quadrangle for Case I, Case II, and Case III

The approach used by CGS (Case III), which ignores the contribution of cohesion to the shear strength, results in almost 20% of the quadrangle being statically unstable (FS < 1) and nearly 40% of the quadrangle having a yield acceleration less than 0.20. In contrast, the large shear strength values used by Jibson et al. (2000) result in very few (< 1%) yield accelerations below 0.30, which implies that the landslide susceptibility across the entire quadrangle is very low. The approach used in this study (Case II) results in a small percentage of the quadrangle being statically unstable (0.4%). Figure 3.10 shows a map of yield acceleration values computed for the Oat Mountain quadrangle using the shear strength parameters in Table 3.1 (Case II). In general, smaller yield acceleration values are concentrated in the steeper slopes. The noticeable band of yield accelerations greater than 0.50 surrounded by areas with much smaller yield accelerations in the north central portion of the quadrangle corresponds to geologic unit "Tm" in the map of geology (Figure 3.5), described as the upper Miocene Modelo Formation (CDMG, 1997b). This geologic unit is in the highest shear strength group in the quadrangle. Maps of yield acceleration for all six quadrangles (for Case II) are given in Appendix A (Figures A-13 through A-18).

A yield acceleration value is a good indicator of a slope's susceptibility to landsliding, but the occurrence of a landslide is also a function of the ground motion intensity. The sliding-block analysis combines the yield acceleration with ground shaking information to predict the occurrence of landslides based on an estimate of the sliding displacement. Empirical models that predict displacement as a function of yield acceleration and one or more ground motion parameters are discussed in the following section.

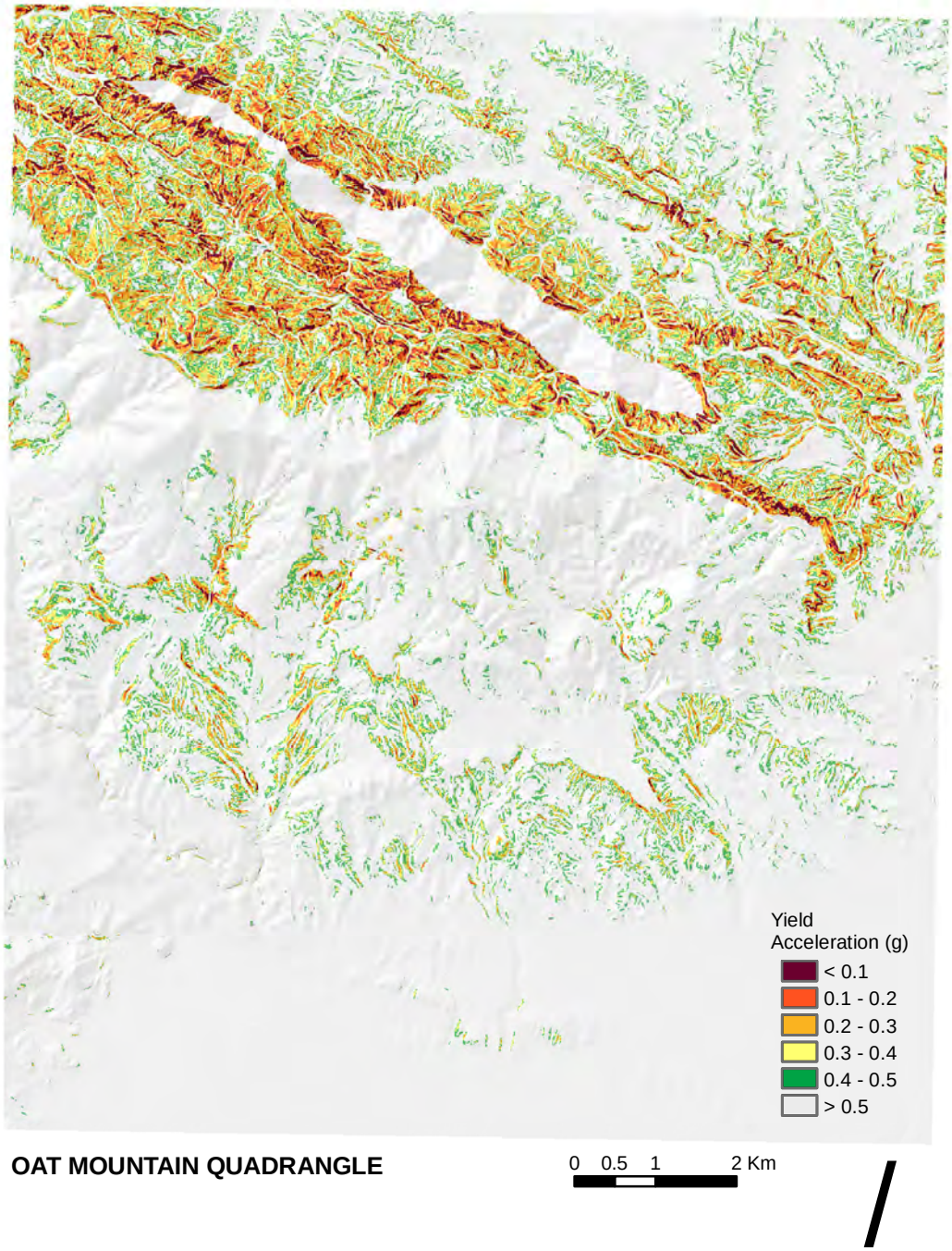


Figure 3.10: Map of yield acceleration values computed for the Oat Mountain quadrangle using shear strength values from Table 3.1 (Case II).

## 3.4 CALCULATING PERMANENT DISPLACEMENTS

The use of displacement prediction equations is an efficient way to compute rigid sliding-block displacements over a large area. Values of yield acceleration and ground shaking information are combined within a GIS and values of permanent displacement are calculated and assigned to individual cells across each quadrangle. Ground shaking is characterized by different predictive models using a single ground motion parameter or combinations of ground motion parameters. The predictive models used in this study and the related ground motion parameters are discussed below.

### 3.4.1 Predictive Models

Seven displacement prediction equations are considered for this study and are summarized in Table 3.2. Models J-($I_a$), J-($PGA$), and J-($PGA$, $I_a$) were developed by Jibson (2007), model RS-($PGA$, M) was developed by Rathje and Saygili (2009), and models RS-($PGA$, $PGV$), RS-($PGA$, $I_a$), and RS-($PGA$, $PGV$, $I_a$) were developed by Saygili and Rathje (2008). For convenience the models designated "RS" will be referred to as the Rathje and Saygili (2008, 2009) models.

The models developed by Jibson (2007) were developed using a database of 2,270 strong-motion records from 30 worldwide earthquakes. The records were double-integrated for five different yield acceleration values (0.05, 0.10, 0.20, 0.30, and 0.40 g) to produce a large data set of displacements with corresponding yield accelerations, peak ground accelerations, and Arias intensities. This data set was sampled to produce a final set of 875 displacements – 175 for each of the five yield acceleration values. Based on this final data set, Jibson (2007) modeled displacements as a function of yield acceleration ($k_y$), Arias intensity ($I_a$), and peak ground acceleration ($PGA$). The standard deviations of these three models are between 0.510 and 0.656 log (base 10) units.

Table 3.2: Displacement prediction equations used in this study

| | | |
|---|---|---|
| **Jibson (2007)** | | |
| J-($I_a$) | $\log D = 2.401 \log I_a - 3.481 \log k_y - 3.230$ | (3.3) |
| J-($PGA$) | $\log D = 0.215 + \log\left[\left(1 - \frac{k_y}{PGA}\right)^{2.341} \cdot \left(\frac{k_y}{PGA}\right)^{-1.438}\right]$ | (3.4) |
| J-($PGA, I_a$) | $\log D = 0.561 \log I_a - 3.833 \log\left(\frac{k_y}{PGA}\right) - 1.474$ | (3.5) |
| **Rathje and Saygili (2008, 2009)** | | |
| RS-($PGA, M$) | $\ln D = 2.39 - 5.24\left(\frac{k_y}{PGA}\right) - 18.78\left(\frac{k_y}{PGA}\right)^2 + 42.01\left(\frac{k_y}{PGA}\right)^3 - 29.15\left(\frac{k_y}{PGA}\right)^4$ $-1.56 \ln PGA + 1.38 \ln I_a$ | (3.6) |
| RS-($PGA, PGV$) | $\ln D = -1.56 - 4.58\left(\frac{k_y}{PGA}\right) - 20.84\left(\frac{k_y}{PGA}\right)^2 + 44.75\left(\frac{k_y}{PGA}\right)^3 - 30.50\left(\frac{k_y}{PGA}\right)^4$ $-0.64 \ln PGA + 1.55 \ln PGV$ | (3.7) |
| RS-($PGA, I_a$) | $\ln D = -0.74 - 4.93\left(\frac{k_y}{PGA}\right) - 19.91\left(\frac{k_y}{PGA}\right)^2 + 43.75\left(\frac{k_y}{PGA}\right)^3 - 30.12\left(\frac{k_y}{PGA}\right)^4$ $-1.30 \ln PGA + 1.04 \ln PGV + 0.67 \ln I_a$ | (3.8) |
| RS-($PGA, PGV, I_a$) | $\ln D = 4.89 - 4.85\left(\frac{k_y}{PGA}\right) - 19.64\left(\frac{k_y}{PGA}\right)^2 + 42.49\left(\frac{k_y}{PGA}\right)^3 - 29.06\left(\frac{k_y}{PGA}\right)^4$ $+0.72 \ln PGA + 0.89(M - 6)$ | (3.9) |

*Note: $D$ is displacement in centimeters, $I_a$ is Arias intensity in meters per second, $k_y$ is the yield acceleration in units of g, PGA is peak ground acceleration in units of g, PGV is peak ground velocity in units of cm/s, and M is moment magnitude.*

The models developed by Rathje and Saygili (2008, 2009) were developed using 2,383 strong motion records downloaded from the Next Generation Attenuation (NGA) database of the Pacific Earthquake Engineering Research Center (http://peer.berkeley.edu/nga). These models use combinations of ground motion parameters that were selected based on the concept of "efficiency" developed by Cornell and Luco (2001). Ground motion parameters that produce less variability in the displacement prediction are considered more efficient. Saygili and Rathje (2008) found that incorporating multiple ground motion parameters significantly increased the efficiency (i.e. reduced the standard deviation) of the displacement prediction. The Rathje and Saygili (2008, 2009) models used in this study predict displacement as a function of yield acceleration and different combinations of peak ground acceleration ($PGA$), peak ground velocity ($PGV$), Arias intensity ($I_a$) and moment magnitude ($M$).

A comparison of the models in Table 3.2 is provided in Figure 3.11. For a given deterministic earthquake event ($M = 7$ @ $5$ $km$) at a typical rock site ($V_{s30} = 760$ $m/s$), predicted displacements are plotted against a range of practical yield acceleration values. Using ground motion prediction equations developed by Boore and Atkinson (2008) this event produces PGA = 0.32 g and PGV = 30 cm/s. The Arias intensity for this event is $I_a$ = 1.1 m/s using the relationship developed by Bray and Travasarou (2003). In general, the models developed by Rathje and Saygili (2008, 2009) predict slightly larger displacements than the models developed by Jibson (2007) in the range of $k_y$ = 0.05 to 0.25. For example, at a yield acceleration of $k_y$ = 0.10, model J-($PGA$, $I_a$) predicts a displacement of $D$ = 3 cm while model RS-($PGA$, $I_a$) predicts a displacement of $D$ = 6 cm. As the yield acceleration approaches zero, the Jibson (2007) model predictions increase towards very large values, while the Rathje and Saygili (2008, 2009) model predictions do not increase as much. Additionally, as the yield acceleration approaches

the peak ground acceleration ($PGA = 0.32\ g$), most of the model predictions approach zero except for the two Jibson (2007) models J-($I_a$) and J-($PGA$, $I_a$) These models do not approach zero because they do not explicitly consider whether $k_y$ is greater than $PGA$.

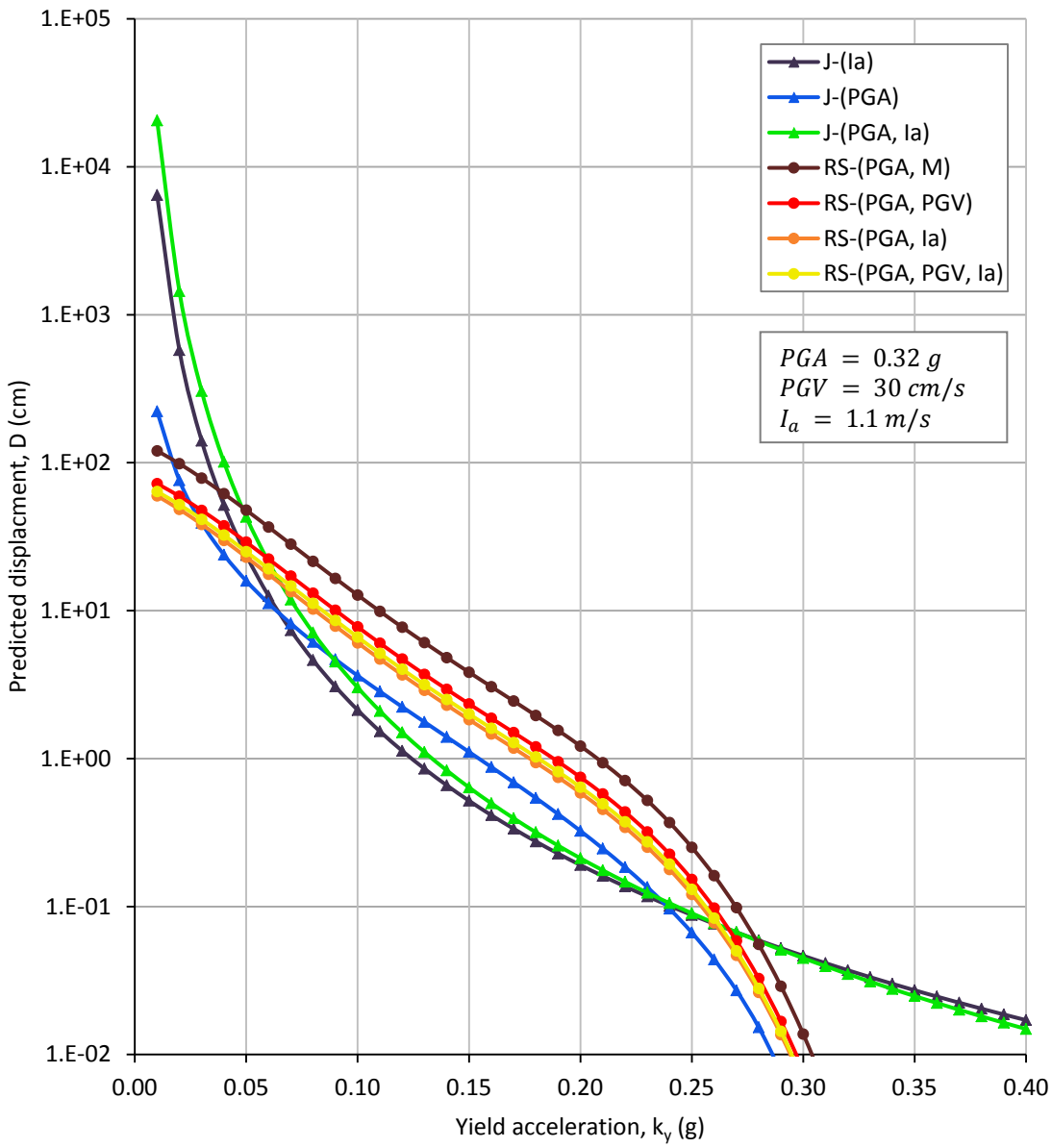


Figure 3.11: Comparison of displacements predicted by the displacement prediction equations in Table 3.2 for a deterministic event (M = 7 @ 5 km)

### 3.4.2 Ground Motion Data

Values of peak ground acceleration ($PGA$ in g), peak ground velocity ($PGV$ in cm/s), and Arias intensity ($I_a$ in m/s) are required to use the displacement prediction models considered in this study. To calculate displacements, estimates of these ground shaking parameters are assigned to 10-meter grid cells within the study area. Because the goal is to evaluate the performance of these models against observations of landsliding from the Northridge earthquake, ground shaking data from the Northridge earthquake are required.

Ground shaking information from the Northridge earthquake is available for download from ShakeMap®, an online mapping tool developed by the USGS that rapidly assesses the extent and intensity of ground shaking following an earthquake. Ground motion estimates are based on strong motion recordings and predicted ground motions derived from empirical ground motion prediction equations (GMPE). Using a reported earthquake magnitude and location, the GMPE calculates values of ground shaking for a grid of hypothetical rock sites. If a grid point falls at an instrumented strong-motion site, the recorded motion is used instead of the predicted motion. For grid points close to an instrumented strong-motion site, ShakeMap® uses both the recorded motion and the predicted motion to develop an estimate of ground shaking. Additionally, ShakeMap® corrects ground motions for site amplification using estimates of shear-wave velocity ($V_{s30}$) and amplification estimates used in GMPEs.

ShakeMap® uses different attenuation relationships for different ground motion parameters. For $PGA$, the Boore et al. (1997) GMPE is used, and for $PGV$, the Joyner and Boore (1988) GMPE is used. Estimates of Arias intensity are not currently generated by ShakeMap®. However, for this project Dr. David Wald of the USGS developed a map of $I_a$ for the Northridge earthquake using values of $I_a$ computed from the recorded motions

combined with the empirical attenuation relationship developed by Travasarou et al. (2003). The output from ShakeMap® is a finely sampled grid (1.5-km spacing) of latitude and longitude pairs with associated ground motion estimates at each point. $PGA$, $PGV$, and $I_a$ data from the Northridge earthquake were downloaded in ASCII file format and converted into 10-meter raster grids within ArcGIS© using a simple kriging interpolation algorithm.

Figure 3.12 shows a map of peak ground acceleration ($PGA$) produced by ShakeMap® following the Northridge earthquake. The approximate location of the study area is shown by the larger blue rectangle (dashed line). The smaller black rectangle represents the surface projection of the fault (Wald et al. 1996), and the black star represents the earthquake epicenter. The majority of strong-motion recording stations (yellow triangles) are located in Los Angeles County, to the south and east of the epicenter. Fewer stations are located to the northwest, near the study area. This results in a greater reliance on ground motion prediction equations to produce estimates of ground shaking within the study area. There can be a great deal of uncertainty involved in creating estimates of ground shaking, particularly when using a sparse network of station recordings. This uncertainty stems from the fact that ground motions can vary greatly over small distances.

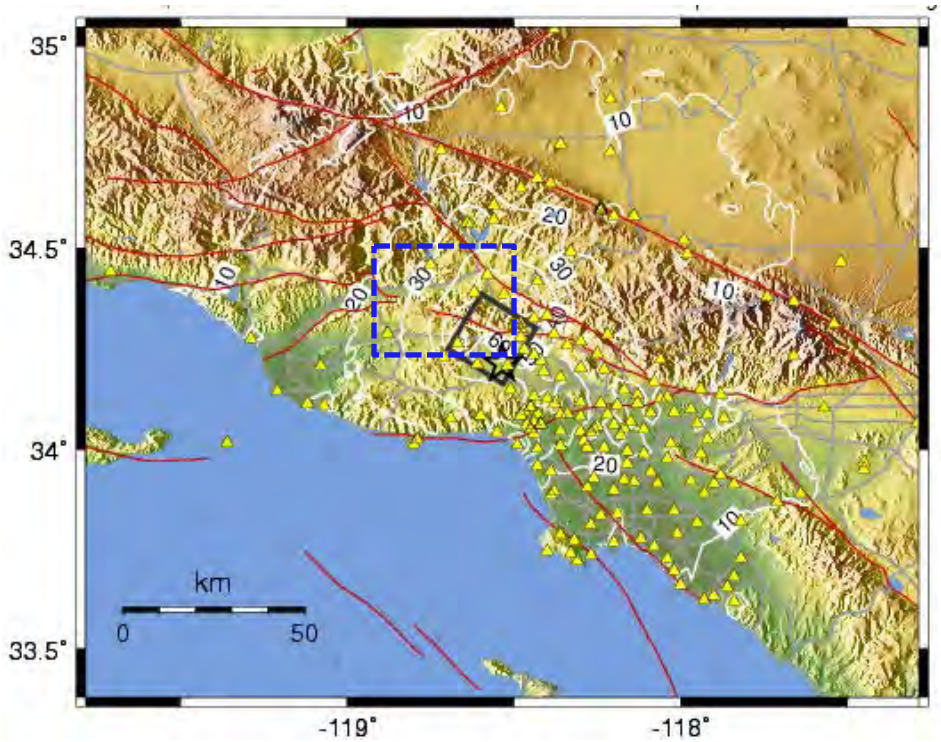


Figure 3.12: ShakeMap® of peak ground acceleration (PGA) during the 1994 Northridge earthquake. Strong motion stations are shown as yellow triangles. The black rectangle represents the surface projection of the fault from Wald et al. (1996). Contours of PGA are shown in % g.

Figures 3.13 through 3.15 show the contours of peak ground acceleration ($PGA$), peak ground velocity ($PGV$), and Arias intensity ($I_a$), respectively, derived from ShakeMap® for the six quadrangles in the study area. The values shown represent the values used in this study. As expected, the values of $PGA$, $PGV$, and $I_a$ increase towards the southeast, closest to the earthquake epicenter. Values of $PGA$ range from about 0.2 g in the northwest corner of the Piru quadrangle to about 0.9 g in the southern portion of the Santa Susana quadrangle; values of $PGV$ range from about 20 cm/s in Piru up to about 140 cm/s in the southeast corner of Oat Mountain; and values of $I_a$ range from about 1 m/s in Piru to more than 10 m/s in some portions of Oat Mountain. Compared with the $I_a$ values used by Jibson et al. (2000), the values in Figure 3.13 are larger.

However, the values in Figure 3.13 are considered better estimates of $I_a$ from the Northridge earthquake because of the robust methodology used by ShakeMap®.

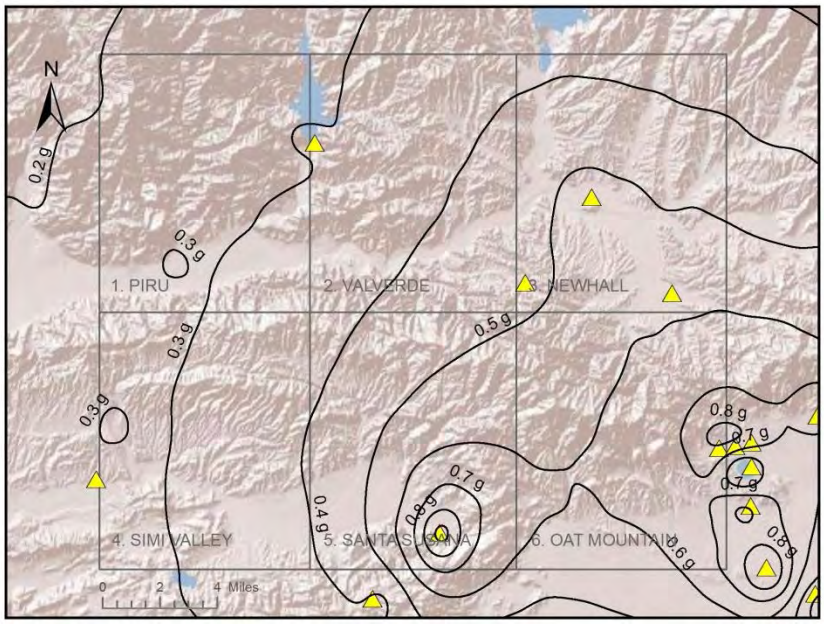


Figure 3.13: Contours of peak ground acceleration (PGA) derived by ShakeMap® in the study area during the Northridge earthquake. Contours of PGA are shown in increments of 0.1 g.

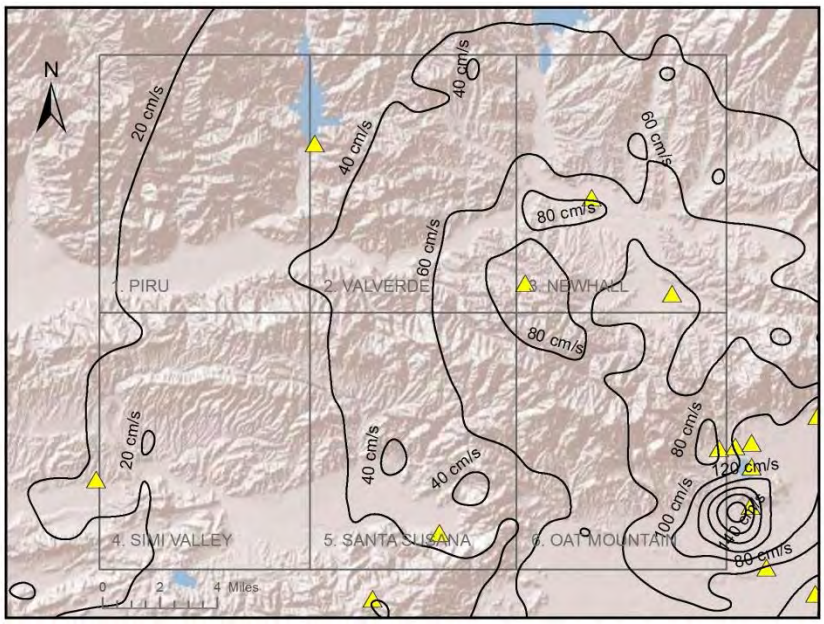


Figure 3.14: Contours of peak ground velocity (PGV) derived by ShakeMap® in the study area during the Northridge earthquake. Contours of PGV are shown in increments of 20 cm/s.

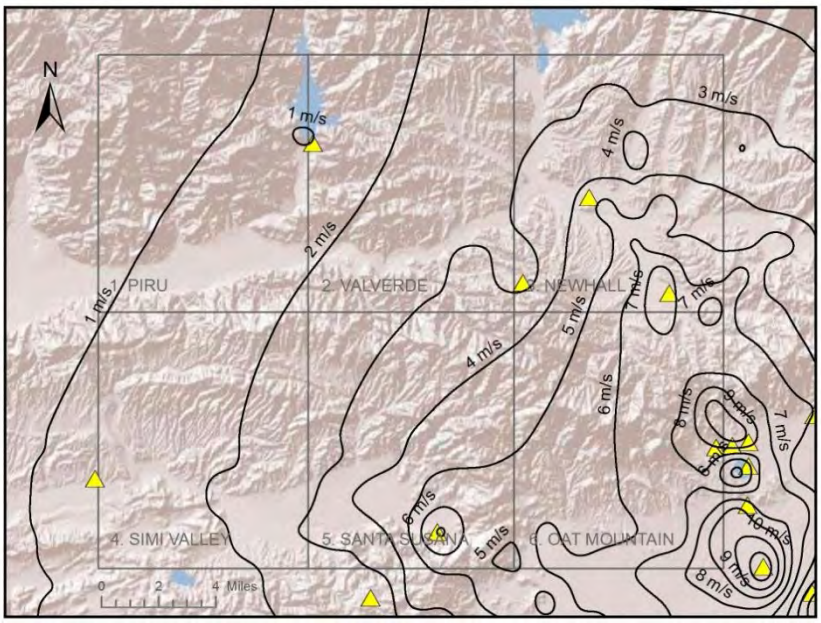


Figure 3.15: Contours of Arias intensity ($I_a$) derived by ShakeMap® in the study area during the Northridge earthquake. Contours of $I_a$ are shown in increments of 1 m/s.

## 3.5 EVALUATING THE USE OF SLIDING DISPLACEMENTS TO PREDICT LANDSLIDES

For the sliding-block method to be useful in predicting earthquake-induced landslides, modeled displacements must correspond well with landslides observed in the field (Jibson 2010). Predictive models (and model parameters) can be validated by comparing computed displacement values with locations of observed landsliding from previous earthquakes. Note that the displacements from the simplified sliding block model do not directly represent displacements that occur in the field. Rather, predicted displacements above some threshold value are often associated with landslide occurrence. Using the ArcGIS© platform, every 10-meter grid cell that is assigned a computed displacement value can be compared with the field observations of landslides (i.e. whether the cell is a landslide or non-landslide cell). Cells with larger computed displacements should intuitively be more likely to correspond to landslide cells than cells with smaller computed displacements. Different predictive models can be compared based on the strength of this correspondence.

Figures 3.16 through 3.21 show the full inventory of landslides triggered by the Northridge earthquake for each of the six quadrangles considered in this study. More than 7,000 individual landslides were digitized within the study area by Harp and Jibson (1995, 1996). The Val Verde quadrangle contains the most observed landslides (approximately 2,500) the Piru, Santa Susana and Oat Mountain quadrangles contain between 1,300-1,400 landslides apiece, and the Simi Valley and Newhall quadrangles contain around 400-450 landslides each. In general, the quadrangles with the higher concentrations of steep slopes experienced the greatest number of landslides.

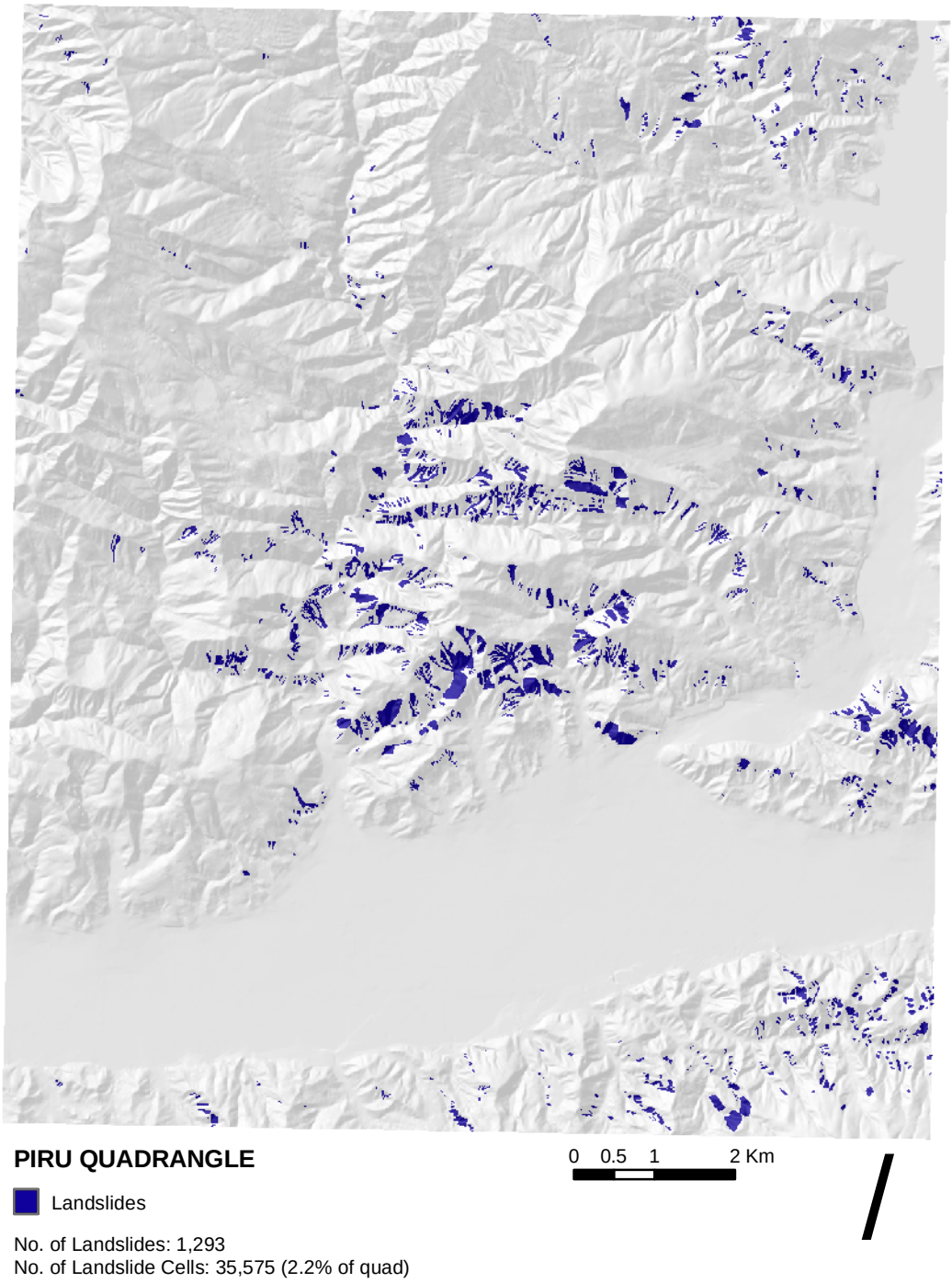


Figure 3.16: Map of landslides observed during the 1994 Northridge earthquake in the Piru quadrangle (Harp and Jibson, 1995, 1996).

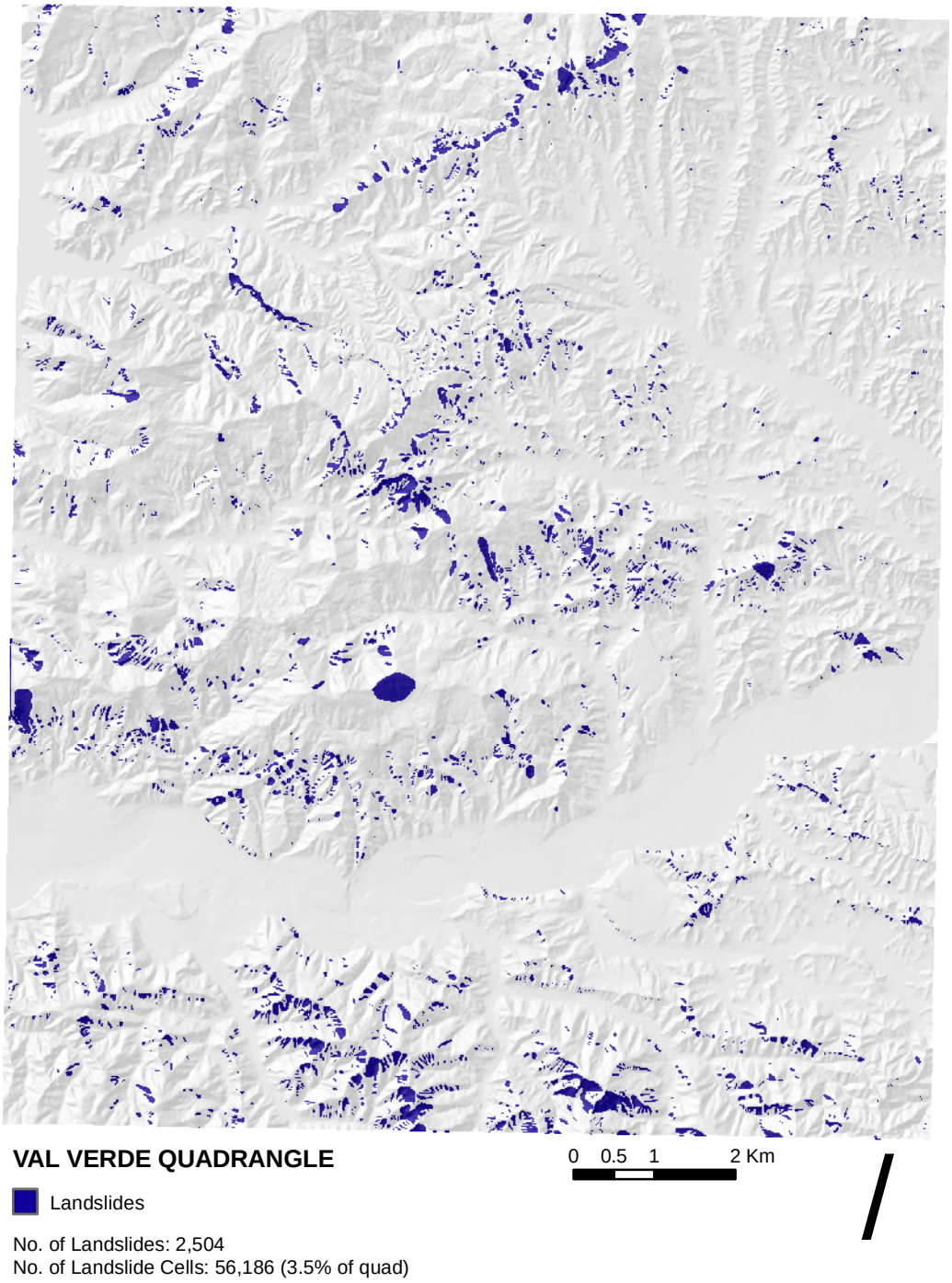


Figure 3.17: Map of landslides observed during the 1994 Northridge earthquake in the Val Verde quadrangle (Harp and Jibson, 1995, 1996).

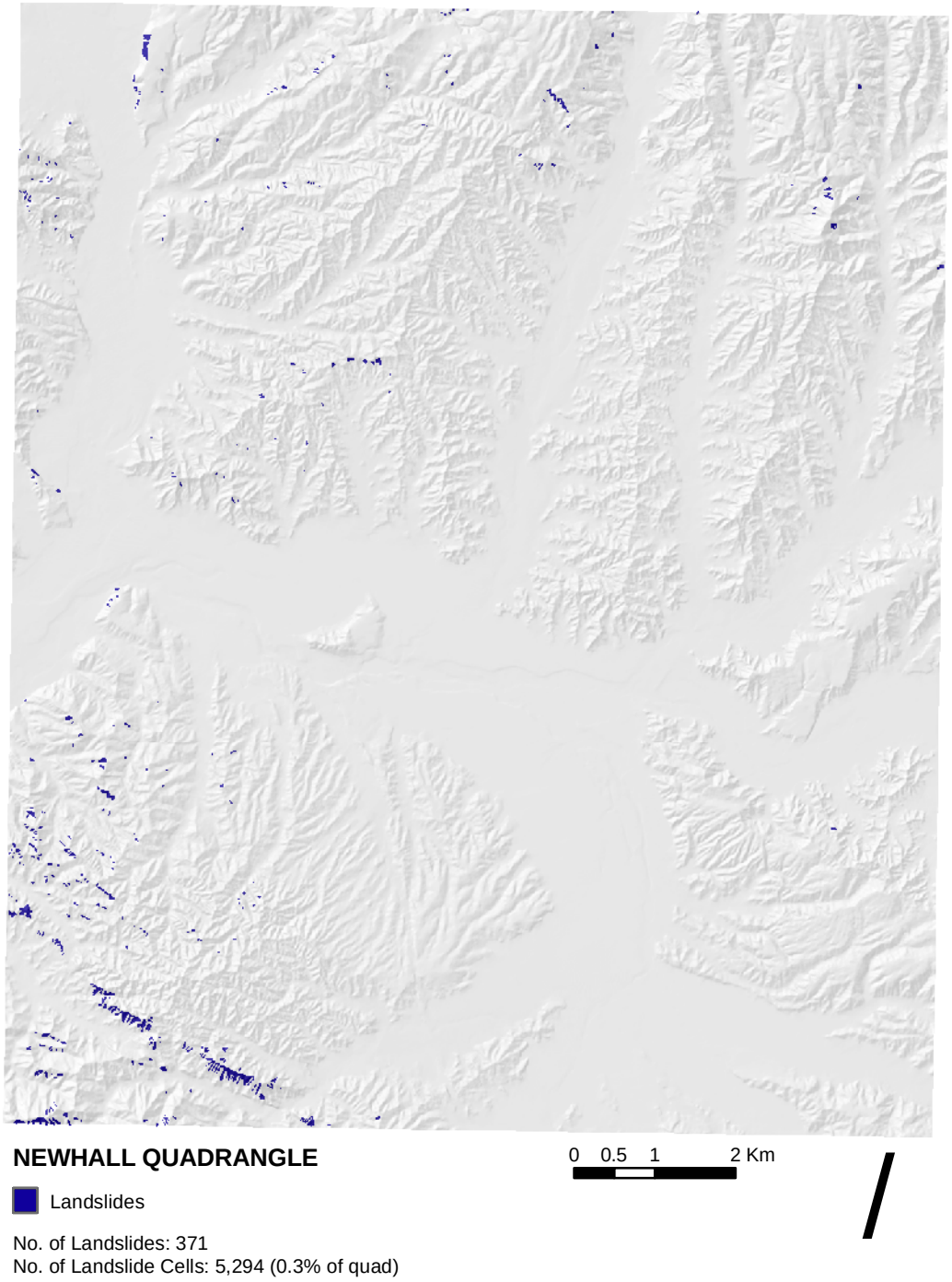


Figure 3.18: Map of landslides observed the 1994 Northridge earthquake in the Newhall quadrangle (Harp and Jibson, 1995, 1996).

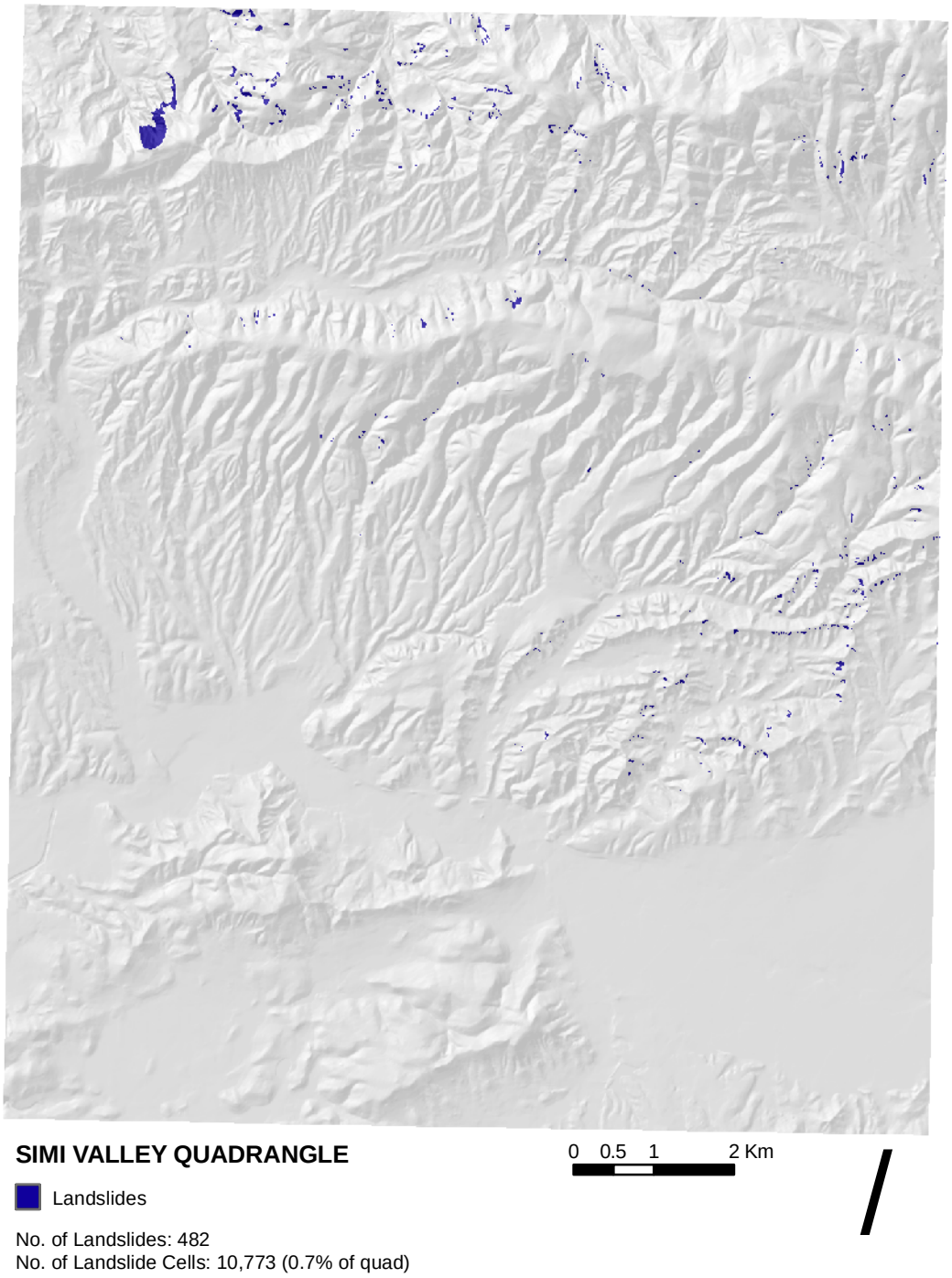


Figure 3.19: Map of landslides observed during the 1994 Northridge earthquake in the Simi Valley quadrangle (Harp and Jibson, 1995, 1996).

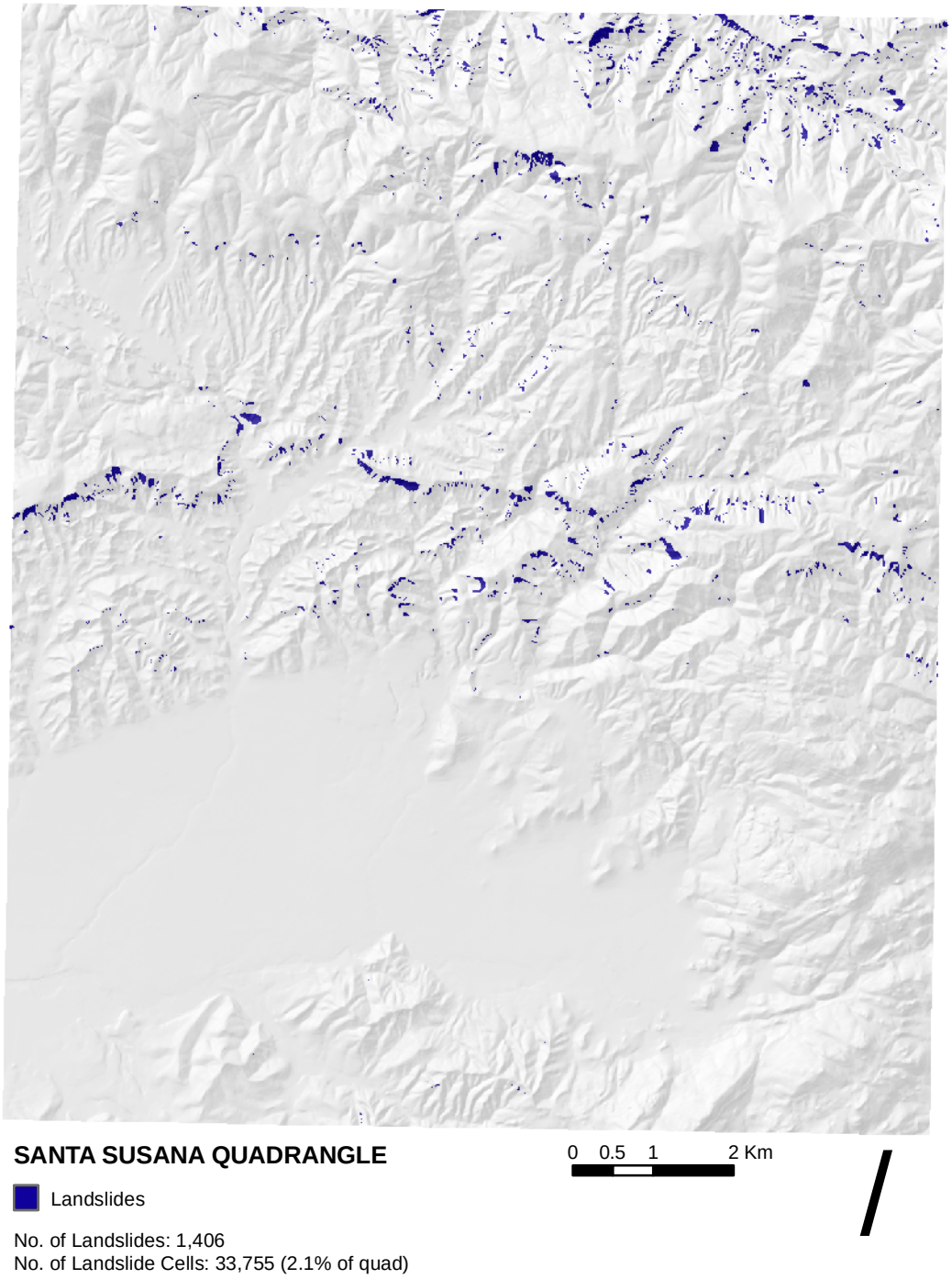


Figure 3.20: Map of landslides observed during the 1994 Northridge earthquake in the Santa Susana quadrangle (Harp and Jibson, 1995, 1996).

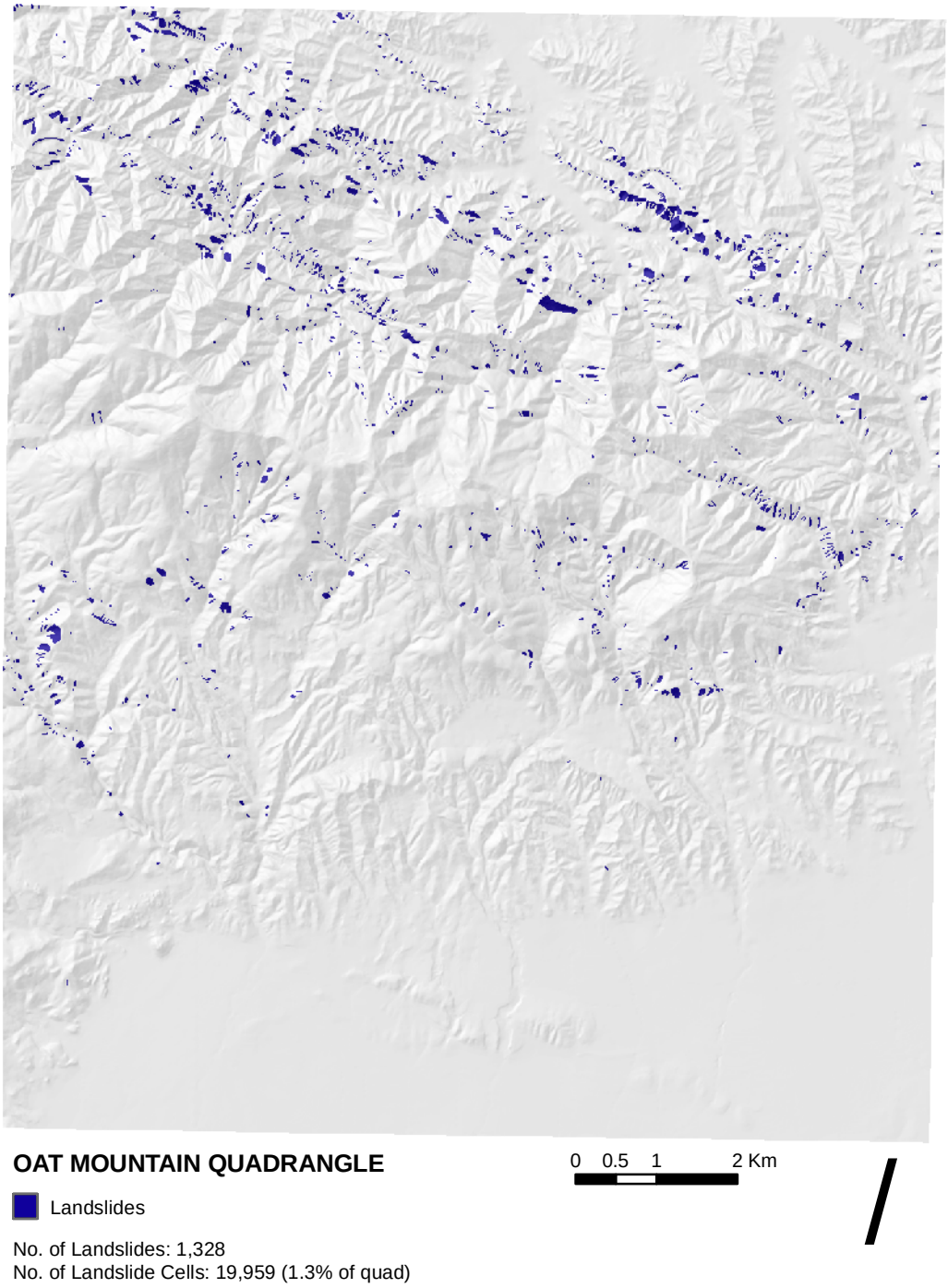


Figure 3.21: Map of landslides observed during the 1994 Northridge earthquake in the Oat Mountain quadrangle (Harp and Jibson, 1995, 1996).

Recognizing that the area of an observed landslide includes the location where the landslide initiated (upslope) and the location where the landslide stopped (downslope), predicted displacements are correlated only with landslide source areas. Landslide source areas are defined as those cells having elevations above the median elevation for each landslide, so that the upper half of each landslide is considered a source area (Jibson et al. 2000). The resulting landslide source areas comprise nearly 80,000 cells (equivalent to 8 square kilometers), or roughly 0.8% of the cells within the six quadrangle study area. Figure 3.22 shows the landslide source cells within Oat Mountain for comparison with the full landslide inventory shown in Figure 3.21. Maps of landslide source areas for all six quadrangles are given in Appendix A (Figures A-19 through A-24).

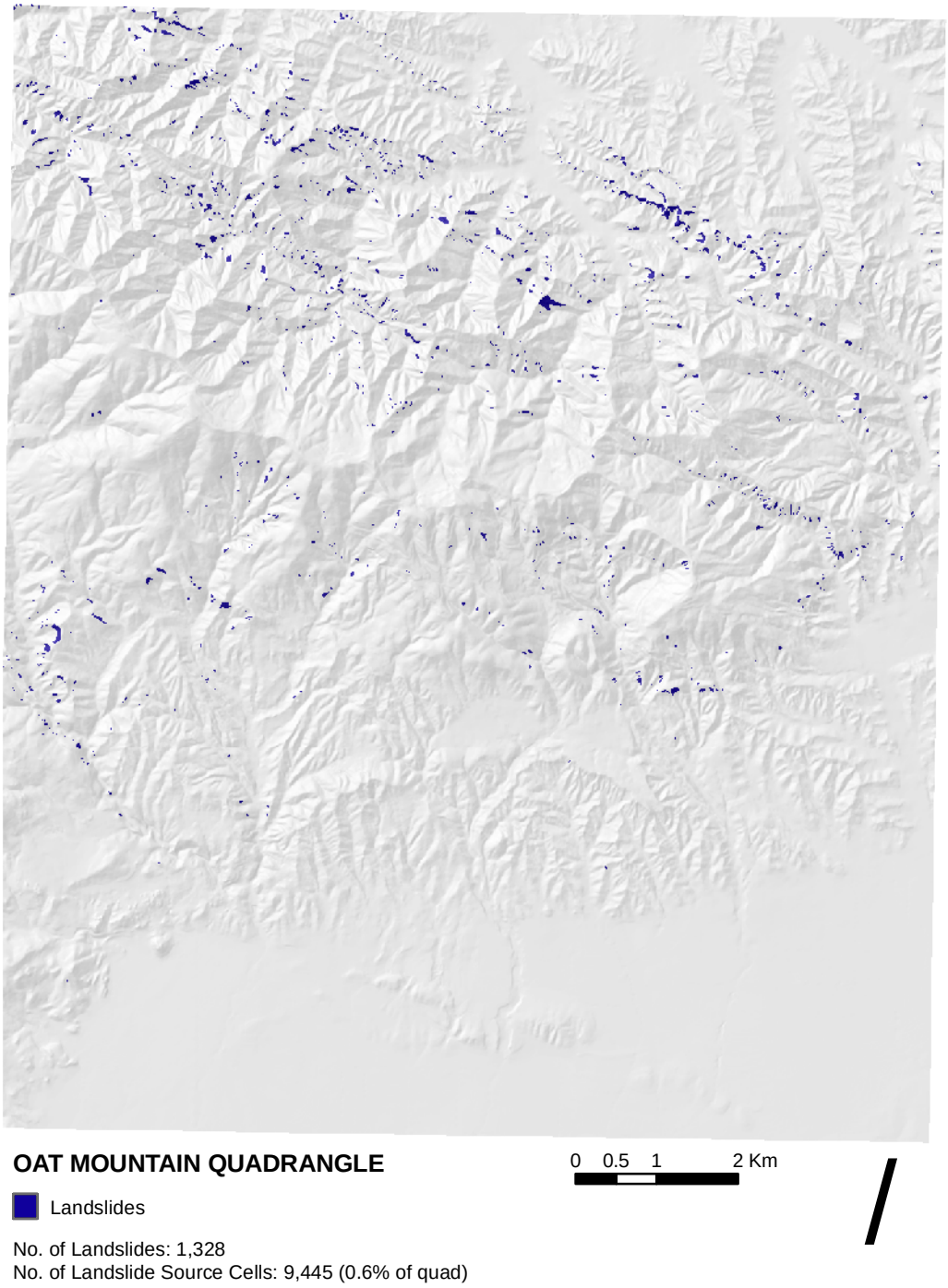


Figure 3.22: Map of landslide sources observed during the 1994 Northridge earthquake in the Oat Mountain quadrangle (Harp and Jibson, 1995, 1996).

One approach that has been used to evaluate the accuracy of the predictive models is to calculate the percentage of landslide source cells (i.e. the upper half of each landslide) that are associated with predicted displacements above a threshold value. This approach was taken by McCrink (2001), as discussed in Section 2.4. One drawback of this approach is that it does not acknowledge the occurrence of false positives (i.e. cells with large predicted displacements that do not correspond with landslide source cells). A model that captures a large percentage of landslide source cells is less useful if it also captures a large percentage of non-landslide source cells. McCrink (2001) calculated the % Quad Cover (i.e. the percentage of cells in a quadrangle that are assigned displacements above the threshold value) of each model as a way of penalizing those models that captured a large percentage of landslide source cells simply because a large percentage of the quadrangle was assigned displacements above the threshold value. However, this metric does not take into account the scenario where a large percentage of the quadrangle is landslide cells, in which case a large % Quad Cover is desirable.

Another approach that has been used to assess the ability of displacement prediction equations to predict landslides is to consider the percentage of cells within a displacement range that are associated with observed landslides. This was the approach taken by Jibson et al. (2000), also discussed in Section 2.4. One drawback of this approach is that it hides a significant amount of false negatives (i.e. small displacements being predicted within observed landslide source cells).

For this study, predicted displacements are compared with locations of observed landslide cells using a cell-by-cell approach and a landslide-by-landslide approach. The cell-by-cell approach takes into account the percentage of landslide source cells associated with displacements above a specified threshold value, as well as statistics on the occurrence of false positives and false negatives. The landslide-by-landslide approach

evaluates the ability of the different predictive models to capture a certain portion of each individual landslide group (i.e. a group of landslide source cells from the same landslide). Both of these approaches are discussed in further detail in the following sections.

### 3.5.1 Cell-by-Cell Approach

The cell-by-cell approach used in this study is similar to the approach used by McCrink (2001). The efficiency of a model is computed as the difference between the percentage of ground failures captured (%GFC) and the percentage of the quadrangle covered (%QC) with predicted landslides (i.e. cells with computed displacements above a threshold value). These parameters are computed as follows:

$$\%\,GFC = \frac{\#\ of\ landslide\ source\ cells\ with\ D > x}{total\ \#\ of\ landslide\ source\ cells} \tag{3.10}$$

$$\%\,QC = \frac{\#\ of\ cells\ with\ D > x}{total\ \#\ of\ cells\ in\ the\ quadrangle} \tag{3.11}$$

$$\%\,Efficiency = \%\,GFC - \%\,QC \tag{3.12}$$

where D is the predicted displacement in centimeters, and x is the specified displacement threshold in centimeters. Establishing a meaningful displacement threshold is a little ambiguous; displacements in the range of 5 to 15 cm have typically been used in previous studies to define failure (Jibson, 2010). For this study, modeled displacements are compared with observed landslides for two different displacement thresholds, 5 cm and 15 cm. Any cells with predicted displacements exceeding these threshold values are considered predicted landslide cells.

In addition to the parameters adopted from McCrink (2001), the percentage of each quadrangle that is covered by observed landslide source cells (% LS Area) and the

ratio of predicted landslide cells to observed landslide source cells (% QC / % LS Area) in each quadrangle is calculated for all models, and both displacement thresholds:

$$\%\ LS\ Area\ = \frac{\#\ of\ landslide\ source\ cells}{total\ \#\ of\ cells\ in\ a\ quadrangle} \tag{3.13}$$

$$\frac{\%\ QC}{\%\ LS\ Area} = \frac{\#\ of\ cells\ with\ D > x}{\#\ of\ landslide\ source\ cells} \tag{3.14}$$

This ratio provides some insight into the relative performance of different models between quadrangles where there are lots of observed landslides (e.g. the Val Verde quadrangle in the study area) and quadrangles where there are few observed landslides (e.g. the Newhall quadrangle in the study area). However, this metric does not consider whether the predicted landslide cells (% QC) are coincident with the observed landslide cells (% LS Area).

To address the occurrence of false positives and false negatives a confusion matrix (Figure 3.23) can be used to tabulate the observed landslide and no-landslide cells with the predicted landslide and no-landslide cells. The accurate predictions are represented by the diagonal elements of the confusion matrix (A, D), while the erroneous predictions are found off the diagonal (B, C). For the 2-class problem of landslide identification, false positives are represented below the diagonal (B) and false negatives above the diagonal (C). Total accuracy is defined as the percentage of cells accurately placed in the landslide or no-landslide bin:

$$\%\ Accuracy\ = \frac{[A+D]}{[A+B+C+D]} \tag{3.15}$$

Total accuracy considers both the landslide and no-landslide cells in quantifying accuracy, while the previously discussed metric % GFC only considers the landslide cells (i.e. % GFC = A/[A+C]).

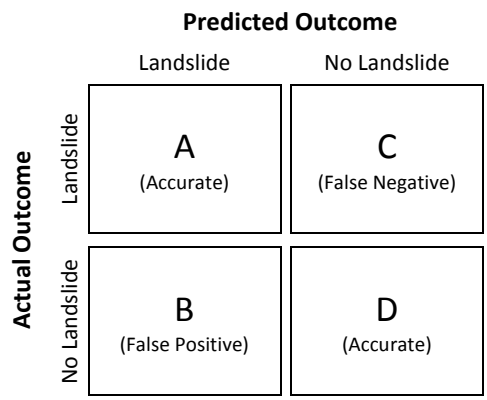


Figure 3.23: Confusion matrix used to evaluate commission error (B/[A+B]) and omission error (C/[A+C]) for landslides in a cell-by-cell comparison of predicted and observed landslides.

The commission error for landslides is defined as the percentage of the predicted landslide cells that are not actually landslide cells (i.e. false positives), and the omission error for landslides is defined as the percentage of observed landslide cells that were predicted to be no-landslide cells (i.e. false negatives):

$$\%\ Commission\ Error\ = \frac{B}{[A+B]} \tag{3.16}$$

$$\%\ Omission\ Error\ = \frac{C}{[A+C]} \tag{3.17}$$

The total accuracy and the commission and omission errors are calculated for each predictive model and each displacement threshold, for all six quadrangles in the study area. The results of these analyses are presented in Chapter 4.

### 3.5.2 Landslide-by-Landslide Approach

Another approach used in this study is to evaluate the success of the predictive models on a landslide-by-landslide basis rather than a cell-by-cell basis. This method credits the predictive models for predicting a specified minimum area of each landslide. For example, if a model captures 50% of the cells within a particular landslide, the cell-by-cell approach will calculate a %GFC = 50%. But if the specified minimum area is 50%, the landslide-by-landslide approach will credit the model for capturing that entire landslide (i.e. 100% success). The landslide-by-landslide approach can be used to better understand the results of the cell-by-cell approach, rather than serve as an alternative. It can help determine why a model captured a large or small percentage of landslide cells in a given quadrangle; maybe the model successfully located several large landslide groups but missed many smaller landslides, or maybe the model did not predict enough landslide cells to capture the larger landslides, but was able to capture many of the smaller landslides. Figure 3.24 illustrates an example of a group of observed landslide cells (outlined in black), a little more than half of which were predicted to be landslide cells (the orange cells). However, it could be argued that the model successfully identified the landslide despite the location being slightly off.

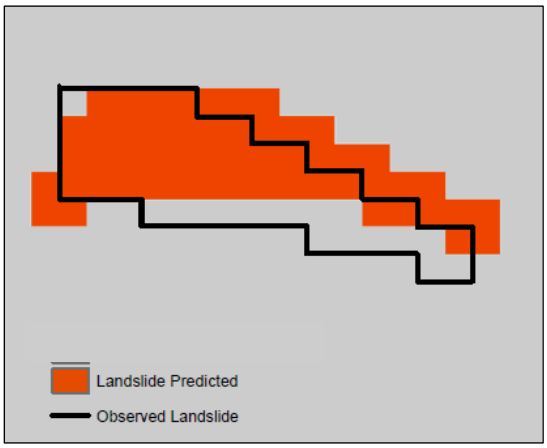


Figure 3.24: Typical comparison between observed and predicted landslide cells.

Each landslide source cell within the study area belongs to an individual, numbered landslide source. The percentage of area of each landslide source that is captured by the models can be calculated by dividing the number of predicted landslide cells within a landslide source by the total number of landslide source cells in that landslide source. The accuracy of the predictive models using the landslide-by-landslide approach, described as the % LS Captured, can then be calculated as the percentage of landslides with at least 50% of the area captured:

$$\%\ LS\ Captured\ = \frac{\#\ of\ landslides\ with\ ratio\ of\ predicted\ to\ observed\ cells \geq 0.5}{total\ \#\ of\ landslides} \quad (3.17)$$

## 3.6 SUMMARY

Using the data and procedures outlined in this chapter, estimates of rigid sliding displacement are calculated and compared with locations of observed landslides from the 1994 Northridge earthquake. The results of these analyses are presented and discussed in the following chapter.

# Chapter 4

# Validation Results

## 4.1 INTRODUCTION

This chapter presents the results of the study. Statistics on the accuracy of each model using the cell-by-cell approach and the landslide-by-landslide approach described in the previous chapter are tabulated herein for all six quadrangles. In addition, the influence of landslide size, geologic unit, slope angle and material strength on the landslide predictions is evaluated.

Because of the large study area and the number of displacement prediction models considered in this exercise, maps of predicted displacement are not shown for all six quadrangles. Instead, a representative region within the Oat Mountain quadrangle has been selected to show the maps of predicted displacement for each model and the maps comparing locations of observed landslides with predicted landslides. The location of the representative region is shown in Figure 4.1 and is located in the northeast corner of the Oat Mountain quadrangle. The representative region consists of geologic units from Strength Group 2 (Tw, Tpc, Qs) and Strength Group 3 (Tps, Qal/Qay).

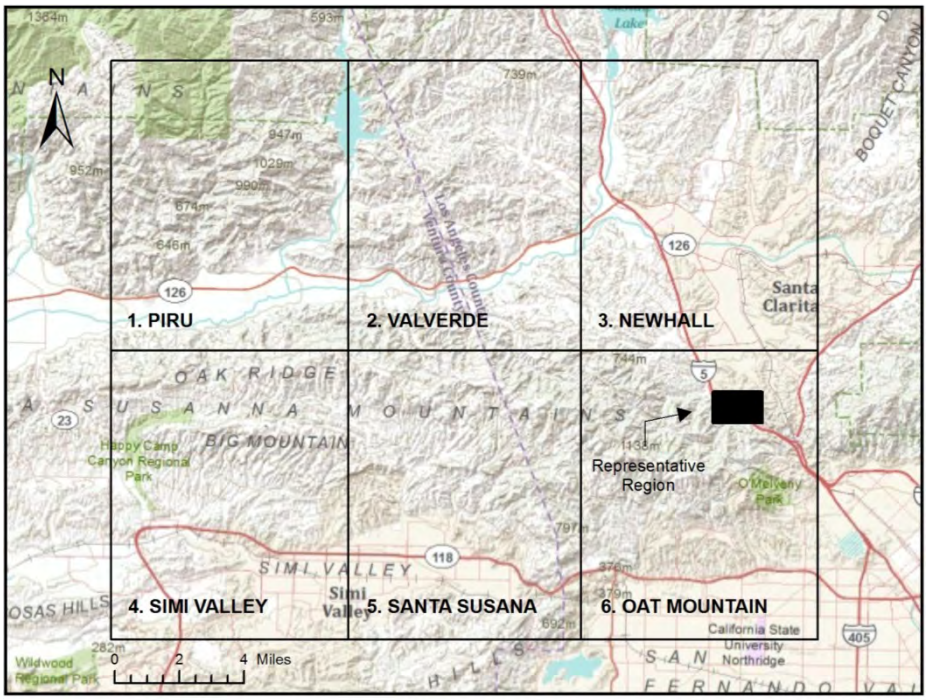


Figure 4.1: Location of the representative region within the Oat Mountain quadrangle used for comparing the results of the different displacement prediction models.

Figure 4.2 shows the observed landslides, the calculated yield acceleration values, and the estimates of $PGA$, $PGV$, and $I_a$ for the representative region within the Oat Mountain quadrangle. The proximity of this area to the fault rupture from the Northridge earthquake resulted in large ground motions, with $PGA$ ~ 0.60 to 0.65 g, $PGV$ ~ 75 to 85 cm/s, and $I_a$ ~ 6.5 m/s. The maps of predicted displacement shown in the following section are based on these input data.

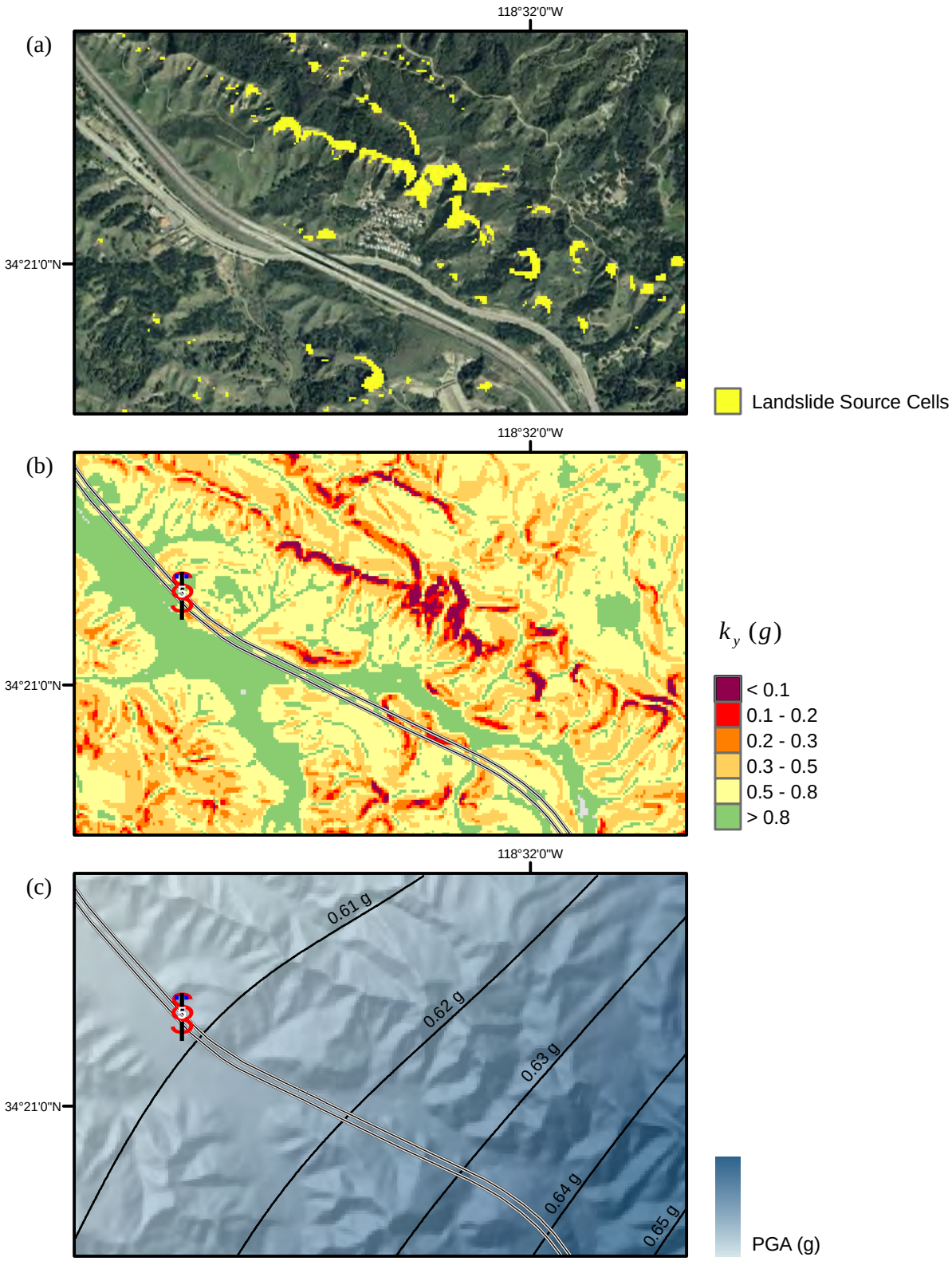


Figure 4.2 (Page 1 of 2): Maps of the small representative region within the Oat Mountain quadrangle showing (a) observed landslides, (b) calculated yield acceleration values, (c) estimates of peak ground acceleration (PGA), (d) estimates of peak ground velocity (PGV), and (e) estimates of Arias intensity.

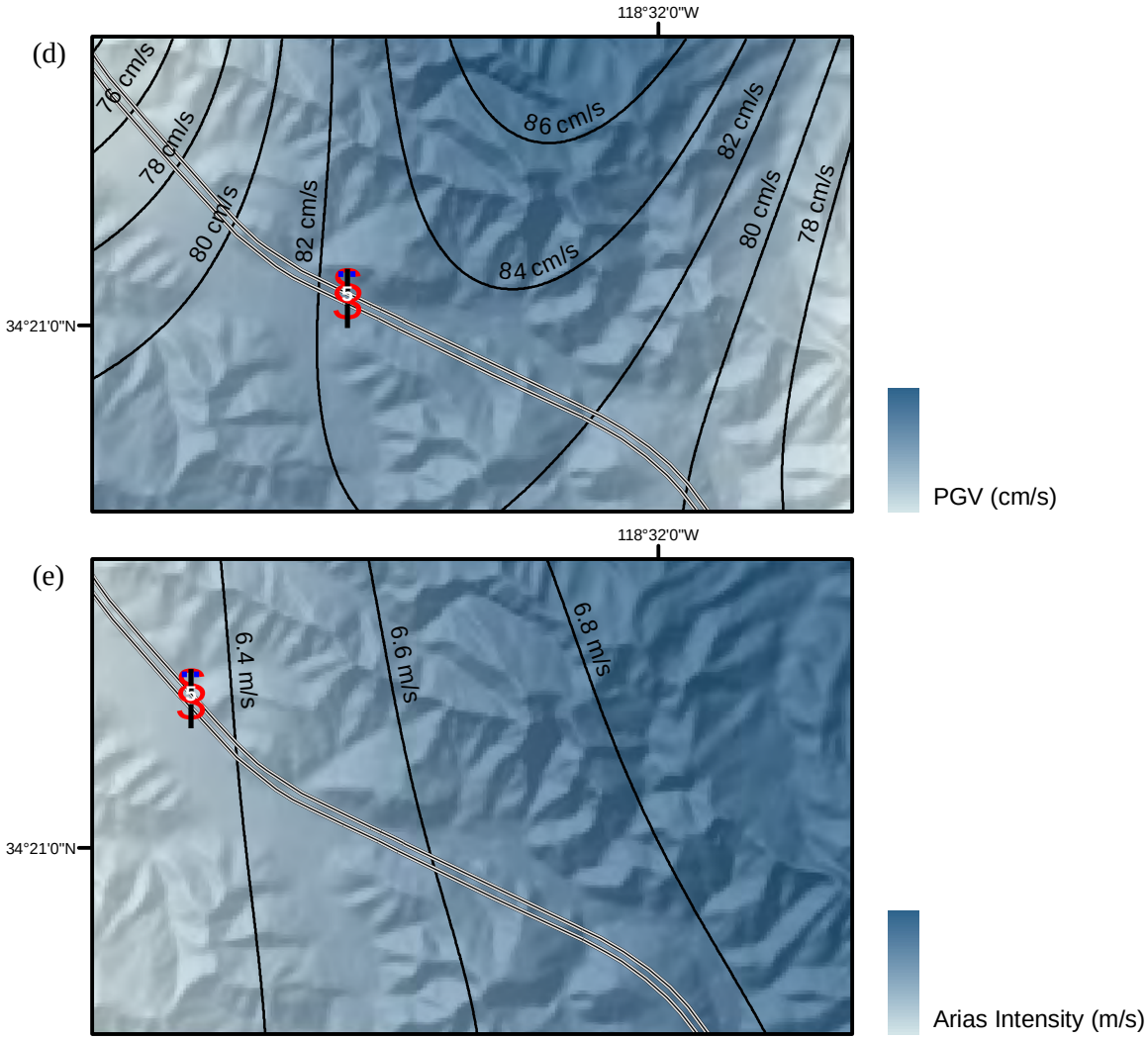


Figure 4.2 (Page 2 of 2): Maps of the small representative region within the Oat Mountain quadrangle showing (a) observed landslides, (b) calculated yield acceleration values, (c) estimates of peak ground acceleration (PGA), (d) estimates of peak ground velocity (PGV), and (e) estimates of Arias intensity.

## 4.2 MAPS OF SLIDING DISPLACEMENT

Figures 4.3(a) through 4.9(a) show sliding displacements calculated for an area within the Oat Mountain quadrangle for all seven displacement prediction models. Larger displacements (greater than 15 cm) are represented by the orange and dark red cells, smaller displacements (less than 5 cm) are represented by the grey and green cells, and moderate displacements (5-15 cm) are represented by the yellow cells. In general, calculated displacements greater than 5 cm are concentrated along the steep ridges, and displacements less than 5 cm are more spread out among flatter slopes. The model that appears to predict the largest number of cells greater than 5 cm in the area shown is model RS-($PGA$, $PGV$, $I_a$), while the model with the fewest number of cells greater than 5 cm in the area shown is model J-($PGA$).

In parts (b) and (c) of Figures 4.3 through 4.9, the displacements that exceed the threshold values of 15 cm and 5 cm, respectively, are shown in pink. These cells represent the landslides predicted when using these displacement thresholds. The locations of observed landslides are shown in blue. Generally, there are fewer observed landslide cells than predicted landslide cells. For example, the representative region has 1,159 observed landslide cells (approximately 3% of the representative region), yet the displacement models predict between 657 and 2,514 landslide cells (1.8 to 6.8% of the representative region) for the 15-cm threshold, and between 1,265 and 5,778 landslide cells (3.4 to 15.6% of the representative) for the 5-cm threshold.

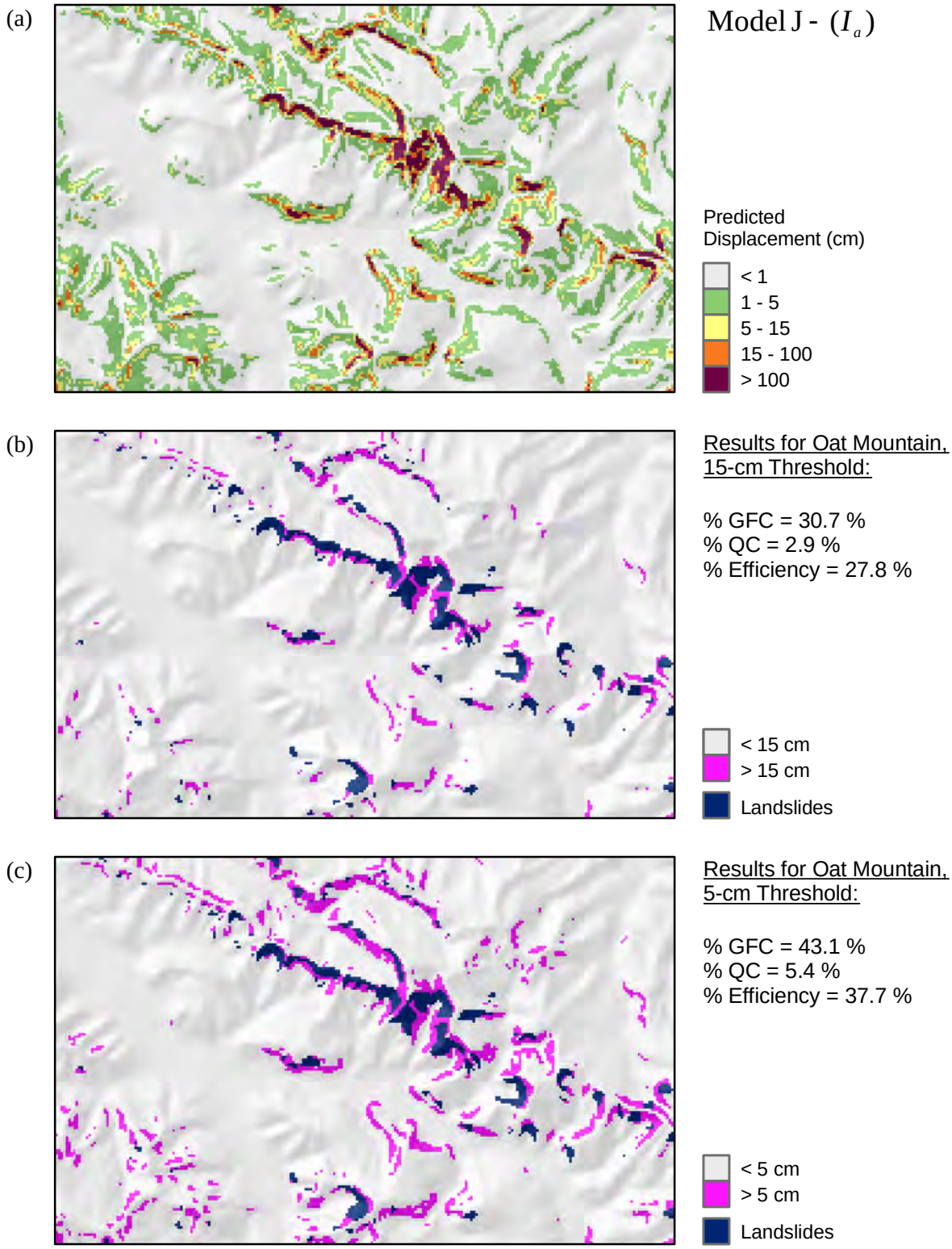


Figure 4.3: Results for Model J-(Ia) in the Oat Mountain quadrangle. (a) Predicted displacements, and (b, c) a comparison of observed and predicted landslides for two displacement thresholds (15 cm, 5 cm) are shown for the representative region. %GFC = percentage of ground failures captured, % QC = percentage of the quad predicted to be landslides, and % Efficiency = (%GFC - %QC).

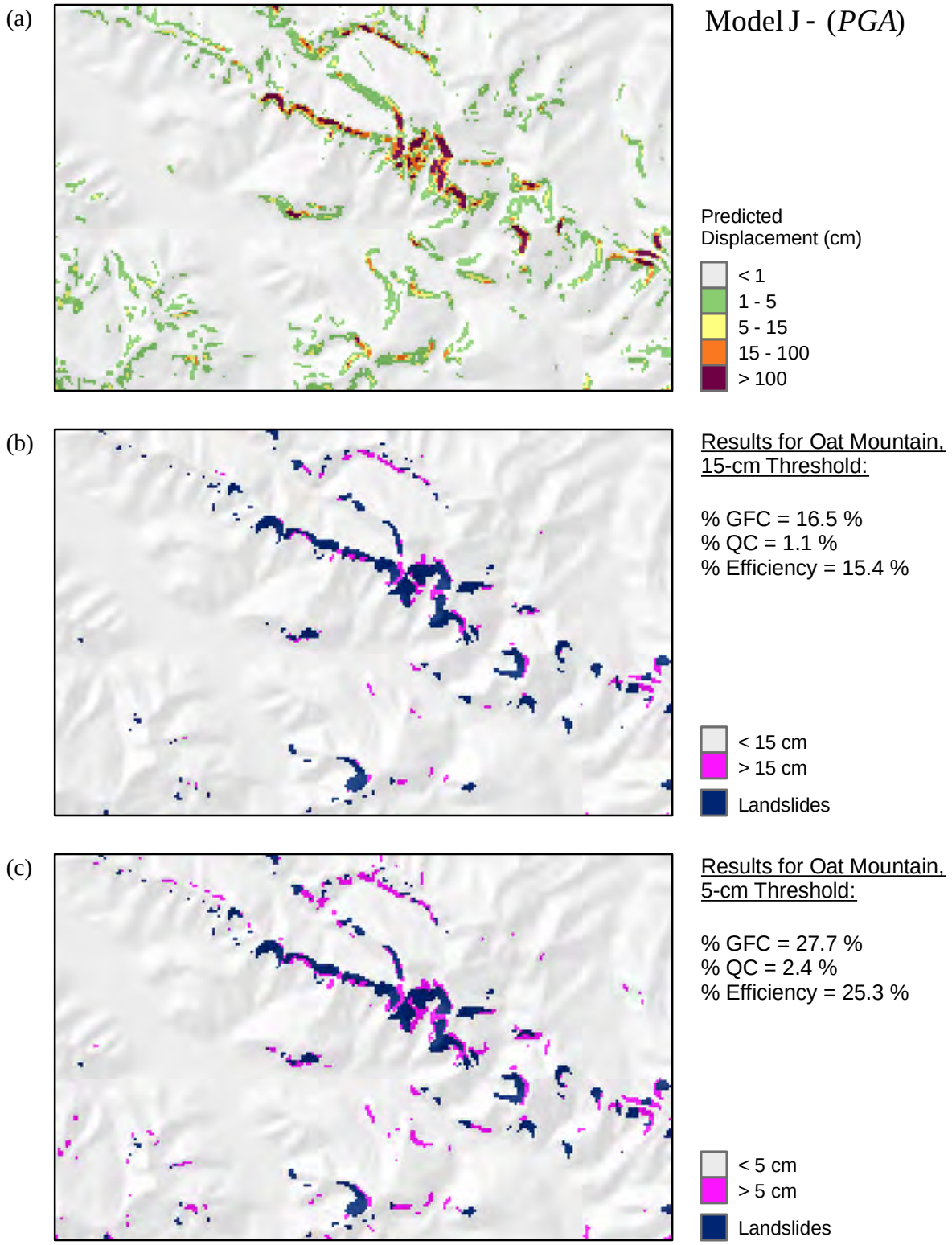


Figure 4.4: Results for model J-(PGA) in the Oat Mountain quadrangle. (a) Predicted displacements, and (b, c) a comparison of observed and predicted landslides for two displacement thresholds (15 cm, 5 cm) are shown for the representative region. %GFC = percentage of ground failures captured, %QC = percentage of the quad predicted to be landslides, and % Efficiency = (%GFC - %QC)

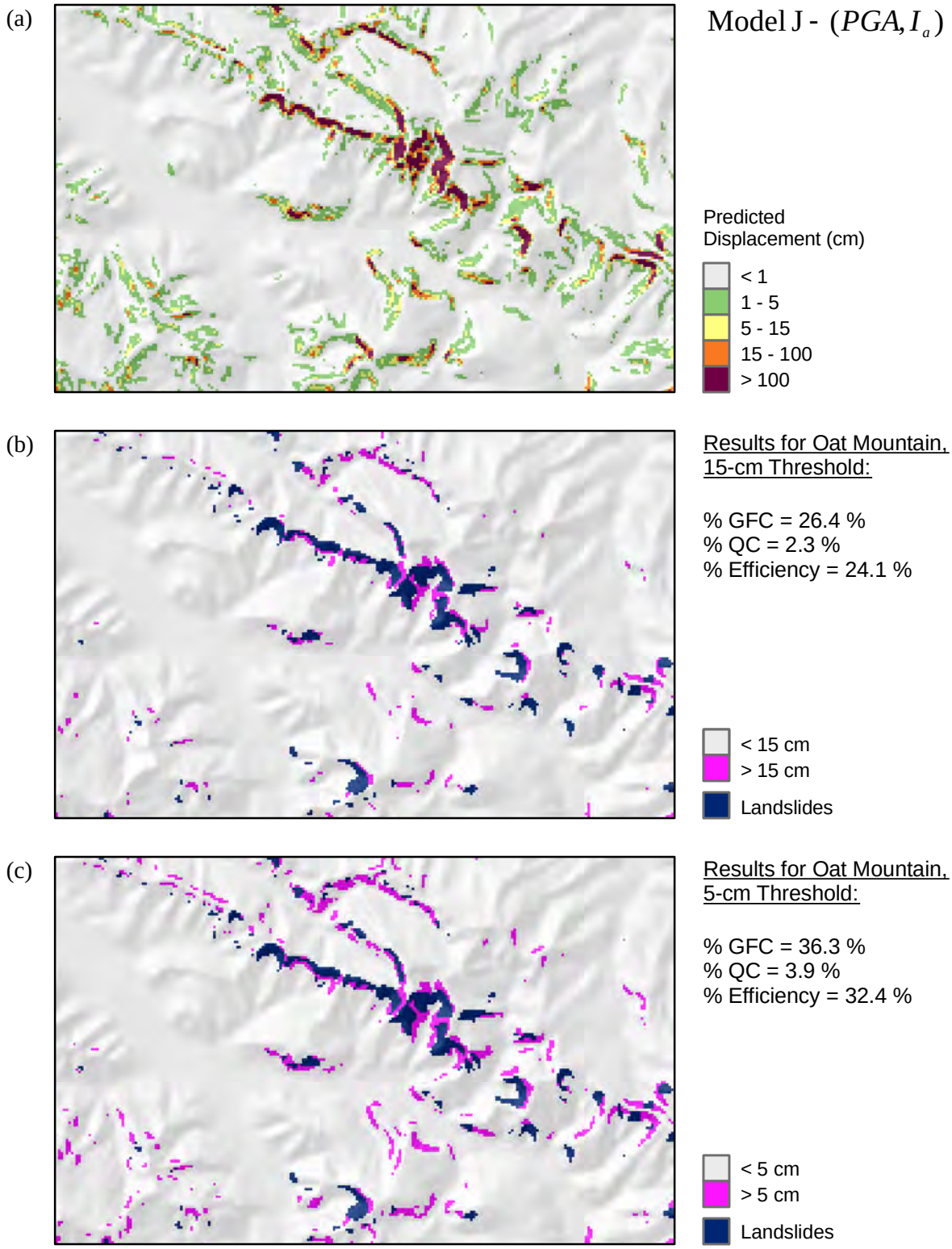


Figure 4.5: Results for Model J-(PGA, Ia) in the Oat Mountain quadrangle. (a) Predicted displacements, and (b, c) a comparison of observed and predicted landslides for two displacement thresholds (15 cm, 5 cm) are shown for the representative region. %GFC = percentage of ground failures captured, % QC = percentage of the quad predicted to be landslides, and % Efficiency = (%GFC - %QC).

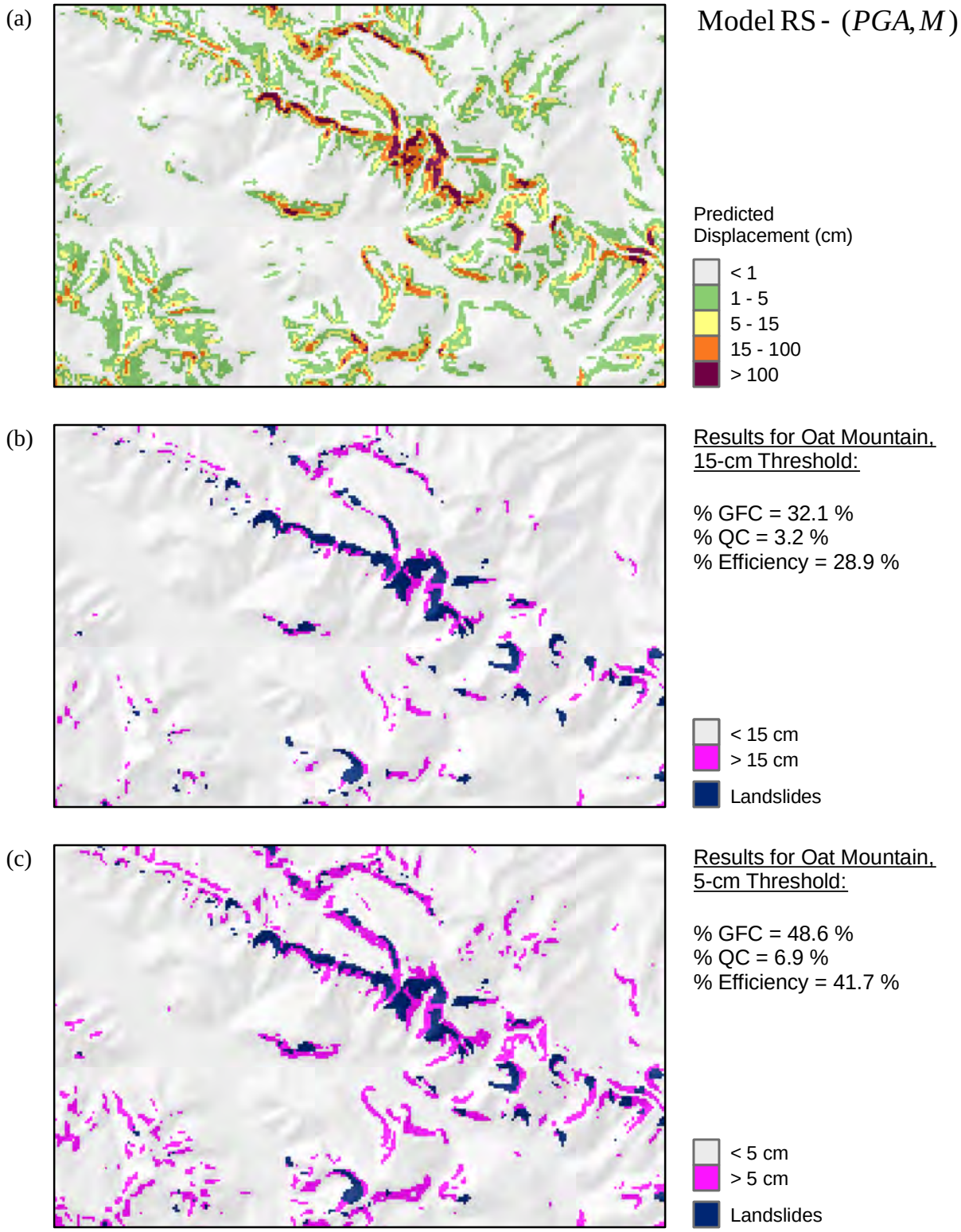


Figure 4.6: Results for Model RS-(PGA, M) in the Oat Mountain quadrangle. (a) Predicted displacements, and (b, c) a comparison of observed and predicted landslides for two displacement thresholds (15 cm, 5 cm) are shown for the representative region. %GFC = percentage of ground failures captured, % QC = percentage of the quad predicted to be landslides, and % Efficiency = (%GFC - %QC).

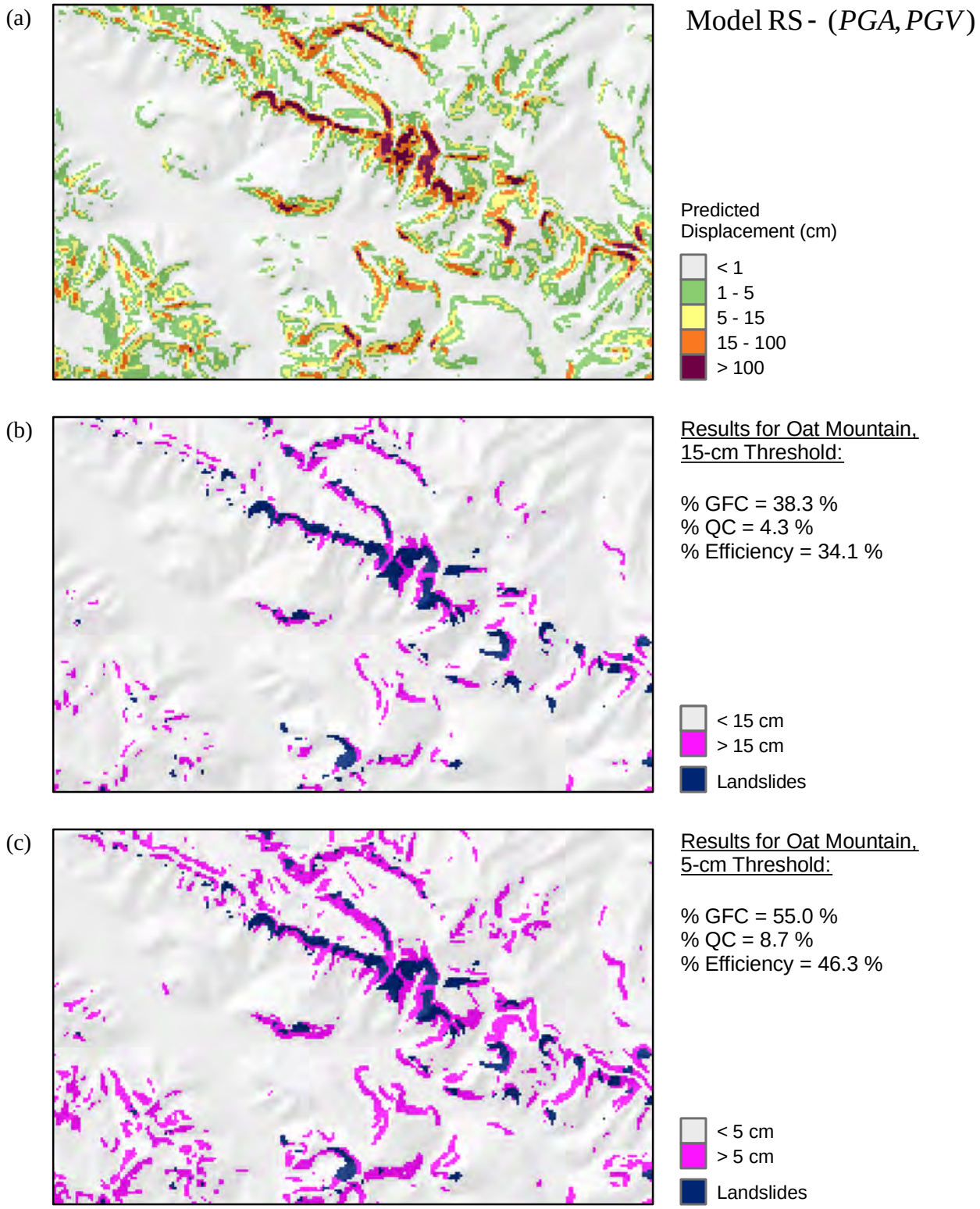


Figure 4.7: Results for Model RS-(PGA, PGV) in the Oat Mountain quadrangle. (a) Predicted displacements, and (b, c) a comparison of observed and predicted landslides for two displacement thresholds (15 cm, 5 cm) are shown for the representative region. %GFC = percentage of ground failures captured, % QC = percentage of the quad predicted to be landslides, and % Efficiency = (%GFC - %QC).

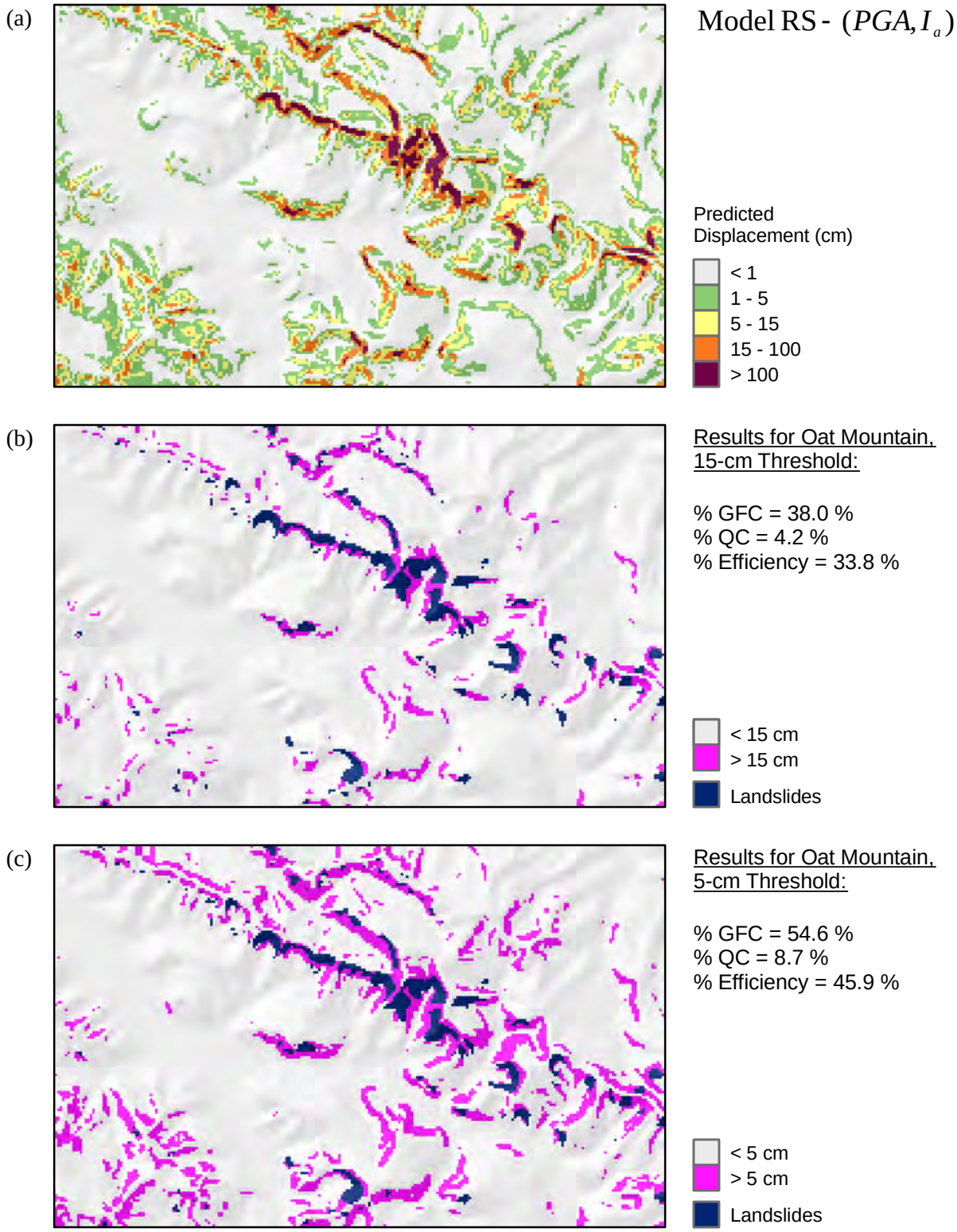


Figure 4.8: Results for Model RS-(PGA, Ia) in the Oat Mountain quadrangle. (a) Predicted displacements, and (b, c) a comparison of observed and predicted landslides for two displacement thresholds (15 cm, 5 cm) are shown for the representative region. %GFC = percentage of ground failures captured, % QC = percentage of the quad predicted to be landslides, and % Efficiency = (%GFC - %QC).

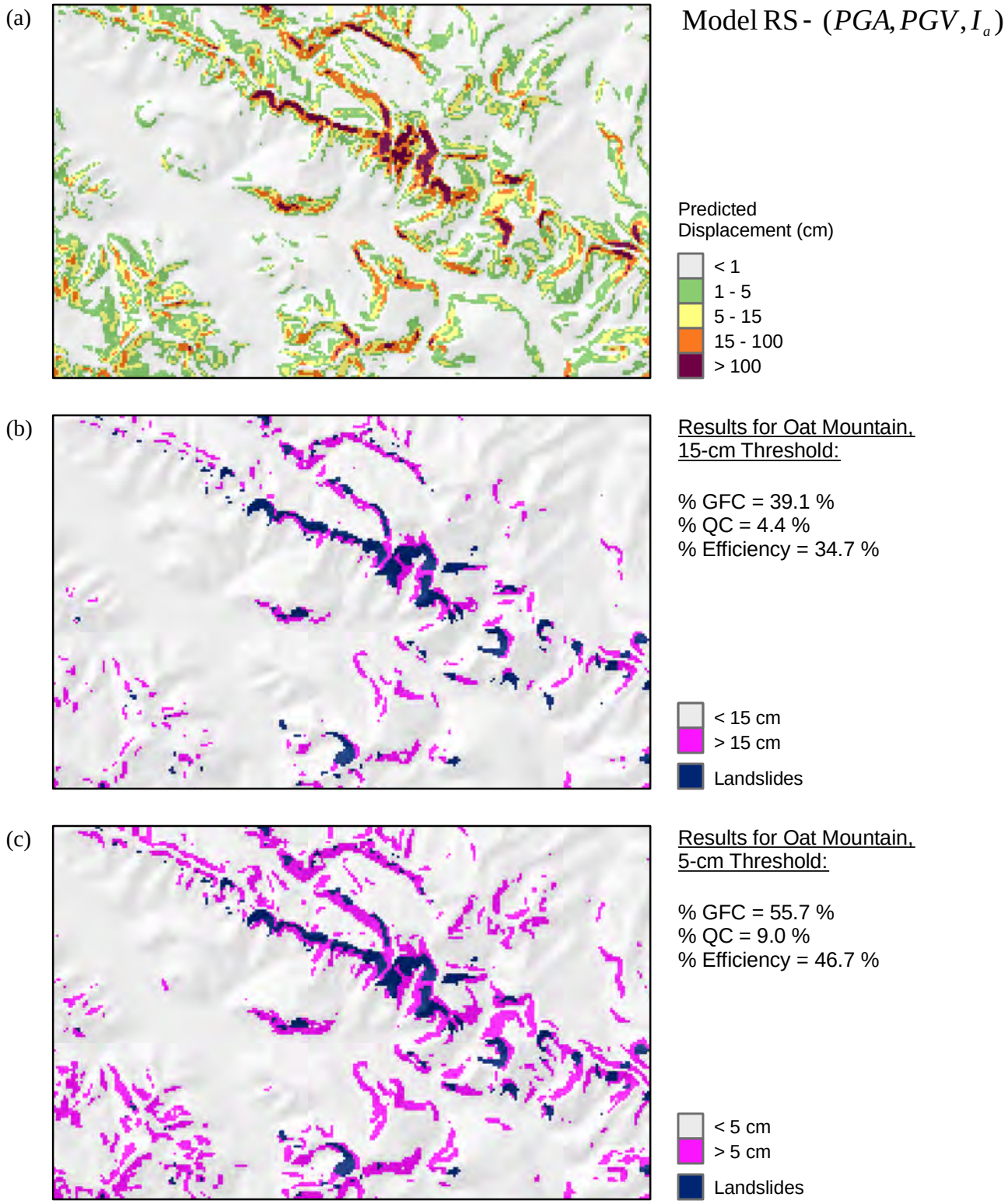


Figure 4.9: Results for Model RS-(PGA, PGV, Ia) in the Oat Mountain quadrangle. (a) Predicted displacements, and (b, c) a comparison of observed and predicted landslides for two displacement thresholds (15 cm, 5 cm) are shown for the representative region. %GFC = percentage of ground failures captured, % QC = percentage of the quad predicted to be landslides, and % Efficiency = (%GFC - %QC).

## 4.3 COMPARISON OF SLIDING DISPLACEMENTS WITH OBSERVED LANDSLIDES

Visually comparing the locations of predicted landslides with the locations of observed landslides in Figures 4.3 through 4.9, each model appears to do a good job of locating the larger landslide groups, but the smaller landslides are harder to locate. Also, there are areas where landsides are predicted but not observed (false positives), and areas where landslides are observed but not predicted (false negatives). In some cases, predicted landslide cells are immediately adjacent to observed landslide cells, indicating that the model identified a landslide but slightly missed its location. These observations are helpful in interpreting the results of quantitative analyses. The results of this study are summarized in the following sections using the analyses described in Chapter 3.

### 4.3.1 Cell-by-cell Comparison

The percentages of ground failures captured (%GFC), the percentages of quadrangle covered by predicted landslide cells (%QC) and the calculated efficiencies (%GFC - %QC) of each model, for all six quadrangles, are compiled in Table 4.1 for a displacement threshold of 15 cm, and in Table 4.2 for a displacement threshold of 5 cm. Also shown in these tables is the percentage of quadrangle covered by observed landslides (% LS Area) for each quadrangle, and the ratio of %QC to % LS Area. The ratio of %QC to % LS Area is a measure of the over-prediction (or under-prediction) of overall landslide area from the various models, without considerations of whether the landslide locations are accurately identified.

On average the 15 cm threshold captures about 20 to 30% of the observed landslide cells (%GFC = 18.7% to 29.1%) and the 5 cm threshold captures about 25 to 40% of the observed landslide cells. Across the different quadrangles the %GFC tends to be largest for the Oat Mountain quadrangle (as high as 55%) and smallest for the Newhall and Simi Valley quadrangles (as low as 10 to 15%). This result may be caused by the

Newhall and Simi Valley quadrangles having experienced the fewest landslides (0.2% and 0.3% LS Area, respectively). The average ratio of %QC / % LS Area is about 3 to 4 for the 15 cm threshold, and about 4 to 7 for the 5 cm threshold. The Piru and Oat Mountain quadrangles consistently show the largest ratios of %QC to % LS Area (generally greater than 5 to 10), while the other quadrangles show ratios generally less than 5. Using the smaller displacement threshold increases the %GFC, but also increases the over-prediction of landslide area.

Table 4.1: Summary of results for all six quadrangles of the study area, for a displacement threshold of 15 cm.

| | | J-(Ia) | J-(PGA) | J-(PGA,Ia) | RS-(PGA,M) | RS-(PGA,PGV) | RS-(PGA, Ia) | RS-(PGA,PGV,Ia) |
|---|---|---|---|---|---|---|---|---|
| 1. PIRU | % GFC | 32.0% | 28.0% | 31.6% | 35.3% | 32.8% | 34.2% | 33.1% |
| % LS Area: 1.2% | % QC | 10.5% | 9.4% | 10.5% | 11.6% | 10.7% | 11.1% | 10.7% |
| | % Efficiency | 21.5% | 18.6% | 21.1% | 23.7% | 22.2% | 23.1% | 22.4% |
| | % QC/% LS Area | 8.7 | 7.8 | 8.7 | 9.6 | 8.9 | 9.2 | 8.9 |
| 2. VAL VERDE | % GFC | 21.2% | 17.0% | 20.2% | 22.3% | 24.1% | 23.5% | 24.1% |
| % LS Area: 1.7% | % QC | 3.6% | 2.7% | 3.3% | 3.9% | 4.3% | 4.1% | 4.3% |
| | % Efficiency | 17.6% | 14.3% | 16.8% | 18.4% | 19.8% | 19.4% | 19.8% |
| | % QC/% LS Area | 2.1 | 1.5 | 1.9 | 2.3 | 2.5 | 2.4 | 2.5 |
| 3. NEWHALL | % GFC | 18.2% | 11.2% | 16.4% | 20.1% | 28.1% | 22.6% | 26.5% |
| % LS Area: 0.2% | % QC | 0.2% | 0.1% | 0.2% | 0.2% | 0.4% | 0.3% | 0.4% |
| | % Efficiency | 18.0% | 11.1% | 16.2% | 19.9% | 27.7% | 22.2% | 26.1% |
| | % QC/% LS Area | 1.4 | 0.7 | 1.1 | 1.5 | 2.4 | 2.0 | 2.3 |
| 4. SIMI VALLEY | % GFC | 17.9% | 16.1% | 17.4% | 18.7% | 16.9% | 18.9% | 17.5% |
| % LS Area: 0.3% | % QC | 0.3% | 0.3% | 0.3% | 0.3% | 0.3% | 0.4% | 0.3% |
| | % Efficiency | 17.6% | 15.8% | 17.1% | 18.3% | 16.6% | 18.6% | 17.2% |
| | % QC/% LS Area | 1.0 | 0.8 | 0.9 | 1.1 | 0.9 | 1.1 | 1.0 |
| 5. SANTA SUSANA | % GFC | 23.3% | 14.6% | 21.4% | 27.3% | 30.8% | 30.2% | 31.0% |
| % LS Area: 1.0% | % QC | 1.2% | 0.6% | 1.1% | 1.6% | 1.9% | 1.8% | 1.9% |
| | % Efficiency | 22.0% | 14.0% | 20.3% | 25.8% | 28.9% | 28.4% | 29.1% |
| | % QC/% LS Area | 1.2 | 0.6 | 1.1 | 1.5 | 1.8 | 1.7 | 1.8 |
| 6. OAT MOUNTAIN | % GFC | 30.7% | 16.5% | 26.4% | 32.1% | 38.3% | 38.0% | 39.1% |
| % LS Area: 0.6% | % QC | 2.9% | 1.1% | 2.3% | 3.2% | 4.3% | 4.2% | 4.4% |
| | % Efficiency | 27.8% | 15.4% | 24.1% | 28.9% | 34.1% | 33.8% | 34.7% |
| | % QC/% LS Area | 5.1 | 1.9 | 4.0 | 5.6 | 7.5 | 7.4 | 7.7 |
| **AVERAGE** | **% GFC** | **25.0%** | **18.7%** | **23.5%** | **27.2%** | **28.8%** | **28.8%** | **29.1%** |
| **AVERAGE** | % QC | 3.1% | 2.3% | 2.9% | 3.4% | 3.6% | 3.6% | 3.6% |
| **AVERAGE** | % Efficiency | 21.9% | 16.4% | 20.6% | 23.8% | 25.3% | 25.2% | 25.4% |
| **AVERAGE** | % QC/% LS Area | 3.7 | 2.8 | 3.5 | 4.1 | 4.3 | 4.3 | 4.4 |

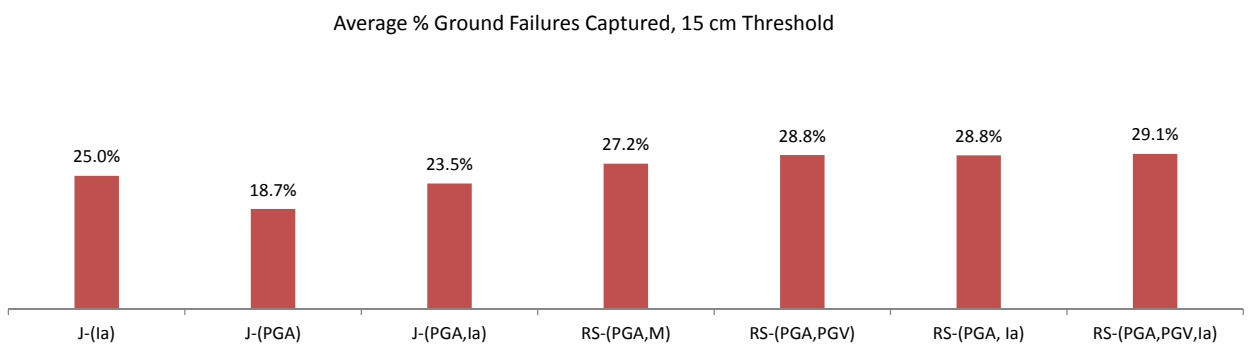

Table 4.2: Summary of results for all six quadrangles of the study area, for a displacement threshold of 5 cm.

| | | J-(Ia) | J-(PGA) | J-(PGA,Ia) | RS-(PGA,M) | RS-(PGA,PGV) | RS-(PGA, Ia) | RS-(PGA,PGV,Ia) |
|---|---|---|---|---|---|---|---|---|
| 1. PIRU | % GFC | 38.6% | 37.0% | 37.4% | 46.9% | 44.2% | 45.9% | 44.6% |
| % LS Area: 1.2% | % QC | 12.5% | 12.3% | 12.3% | 15.6% | 14.4% | 14.9% | 14.5% |
| | % Efficiency | 26.1% | 24.7% | 25.2% | 31.3% | 29.8% | 30.9% | 30.1% |
| | % QC/% LS Area | 10.4 | 10.2 | 10.2 | 13.0 | 12.0 | 12.4 | 12.1 |
| 2. VAL VERDE | % GFC | 26.6% | 22.1% | 24.1% | 30.9% | 33.3% | 32.4% | 33.2% |
| % LS Area: 1.7% | % QC | 4.9% | 3.9% | 4.3% | 6.1% | 6.8% | 6.5% | 6.8% |
| | % Efficiency | 21.6% | 18.2% | 19.8% | 24.8% | 26.5% | 25.9% | 26.5% |
| | % QC/% LS Area | 2.8 | 2.3 | 2.5 | 3.5 | 3.9 | 3.8 | 3.9 |
| 3. NEWHALL | % GFC | 26.4% | 18.6% | 22.8% | 33.2% | 43.4% | 36.7% | 41.6% |
| % LS Area: 0.2% | % QC | 0.5% | 0.2% | 0.3% | 0.6% | 1.0% | 0.9% | 1.0% |
| | % Efficiency | 26.0% | 18.4% | 22.5% | 32.5% | 42.4% | 35.9% | 40.6% |
| | % QC/% LS Area | 2.8 | 1.3 | 1.9 | 4.0 | 6.6 | 5.4 | 6.3 |
| 4. SIMI VALLEY | % GFC | 20.7% | 19.3% | 19.6% | 23.4% | 21.1% | 23.7% | 22.0% |
| % LS Area: 0.3% | % QC | 0.4% | 0.4% | 0.4% | 0.5% | 0.4% | 0.5% | 0.5% |
| | % Efficiency | 20.3% | 18.9% | 19.2% | 22.9% | 20.7% | 23.2% | 21.5% |
| | % QC/% LS Area | 1.3 | 1.1 | 1.2 | 1.6 | 1.4 | 1.6 | 1.5 |
| 5. SANTA SUSANA | % GFC | 35.1% | 24.5% | 31.0% | 45.2% | 48.2% | 48.4% | 48.7% |
| % LS Area: 1.0% | % QC | 2.3% | 1.3% | 1.8% | 3.5% | 4.0% | 4.0% | 4.1% |
| | % Efficiency | 32.8% | 23.2% | 29.1% | 41.7% | 44.2% | 44.4% | 44.6% |
| | % QC/% LS Area | 2.2 | 1.3 | 1.8 | 3.4 | 3.9 | 3.9 | 4.0 |
| 6. OAT MOUNTAIN | % GFC | 43.1% | 27.7% | 36.3% | 48.6% | 55.0% | 54.6% | 55.7% |
| % LS Area: 0.6% | % QC | 5.4% | 2.4% | 3.9% | 6.9% | 8.7% | 8.7% | 9.0% |
| | % Efficiency | 37.7% | 25.3% | 32.4% | 41.7% | 46.3% | 45.9% | 46.7% |
| | % QC/% LS Area | 9.5 | 4.3 | 6.8 | 11.9 | 15.2 | 15.2 | 15.7 |
| **AVERAGE** | **% GFC** | **32.7%** | **26.4%** | **29.7%** | **39.3%** | **41.0%** | **41.0%** | **41.3%** |
| **AVERAGE** | % QC | 4.3% | 3.4% | 3.8% | 5.5% | 5.9% | 5.9% | 5.9% |
| **AVERAGE** | % Efficiency | 28.4% | 23.1% | 25.9% | 33.8% | 35.1% | 35.1% | 35.3% |
| **AVERAGE** | % QC/% LS Area | 5.2 | 4.0 | 4.6 | 6.6 | 7.1 | 7.1 | 7.1 |

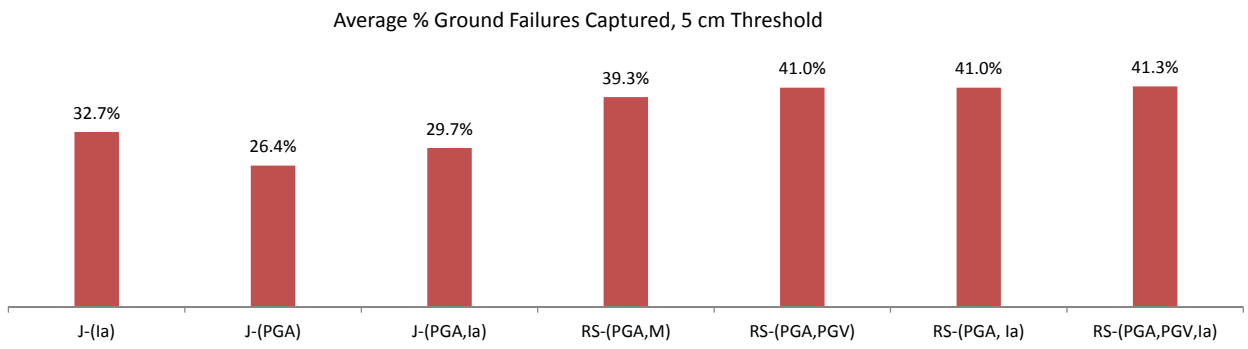

Comparing the different displacement prediction models, Tables 4.1 and 4.2 indicate that models that predict a greater number of large displacements (and thus cover more of the quadrangle) capture a larger percentage of ground failures. On average, model RS-($PGA, PGV, I_a$) captures the largest percentage of landslide source cells across all six quadrangles (GFC = 29.8%, 41.3% for the 15 cm and 5 cm thresholds, respectively) and covers the largest percentage of the six quadrangles (QC = 3.6%, 5.9%). Model J-($PGA$) captures the smallest percentage of landslide source cells (GFC = 21.0%, 26.4%) and covers the smallest percentage of the six quadrangles (QC = 2.3%, 3.4%). For comparison, observed landslide source areas represent only 0.8% of the area of all six quadrangles.

The models that predict displacement as a function of more than one ground motion parameter generally capture a larger percentage of landslides than the models that use only one ground motion parameter. The exception is model J-($PGA, I_a$) which captures a slightly smaller percentage of landslides across all six quadrangles than model J-($I_a$). The models developed by Rathje and Saygili (2008, 2009) that pair estimates of $PGA$ with estimates of $PGV$ and/or $I_a$ (RS-($PGA$,$PGV$), RS-($PGA$,$I_a$), and RS-($PGA$,$PGV$,$I_a$)) all produce similar results. In fact, the results between models within a given quadrangle are less varied than the results between quadrangles. For example, with a 5 cm threshold the models generally capture 40 to 55% of landslide source cells in Oat Mountain, but only 20 to 25% in Simi Valley.

Hard to see in this data are the large number of false positives that occur as a result of over-predicting landslides. Comparing the percentage of each quad covered by observed landslide source cells (% LS Area) with the percentage covered by predicted landslide cells (% QC) provides some insight. In Table 4.2, model RS-($PGA$, $M$) with a 5 cm threshold captures almost 50% of the observed landslides in the Piru quadrangle,

but covers almost 16% of the quadrangle with predicted landslides. This is 13 times greater than the area covered by observed landslides (% LS Area = 1.2%). Figure 4.10 illustrates this large number of false positives by showing a small area within the Piru quadrangle where nearly 100% of the observed landslides are predicted by model RS-($PGA$, $M$) with a 5 cm threshold, but far more landslides are predicted than observed.

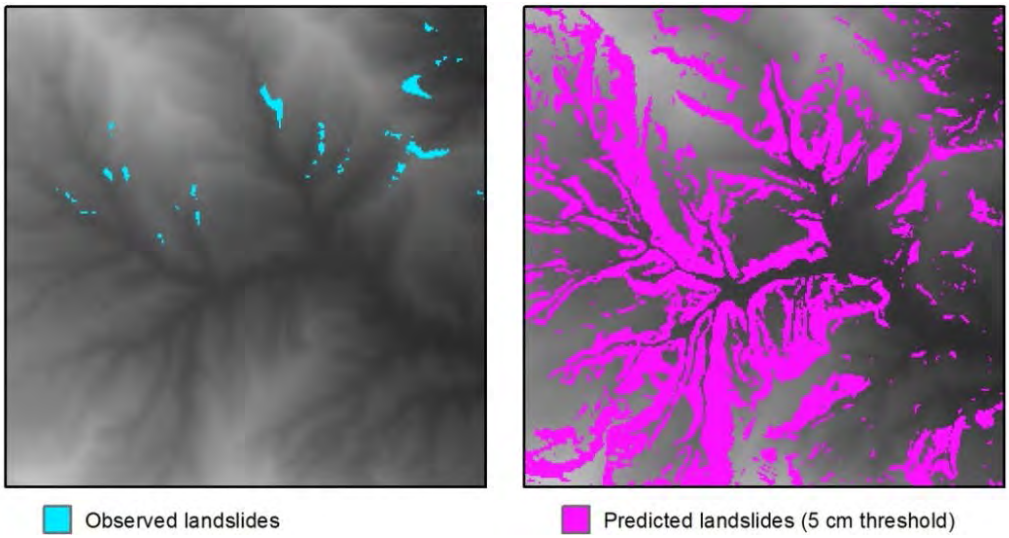


Figure 4.10: Example of false positives for model RS-($PGA$, $M$) with a 5 cm threshold. Observed and predicted landslides are shown for a small area within the Piru quadrangle, overlain onto a DEM. The area shown predominately consists of geologic units Tm4 and Qls.

The total accuracies (considering accurate identification of both landslides and non-landslides), as well as the commission errors (false positives) and omission errors (false negatives) for all models and all quadrangles are summarized in Tables 4.3 and 4.4 for the 15 cm and 5 cm displacement thresholds, respectively. Noticeably, all of the accuracies are relatively high (greater than 85%), but these high accuracies are being predominately influenced by the accurate identification of non-landslide cells, which cover a very large percentage (> 98%) of each quadrangle. Commission errors are

generally between 80 and 95% for all analyses. These large commission errors mean that 80 to 95% of predicted landslides are not landslides (i.e. false positives). These are extremely large numbers, and further indicate the over-prediction of landslide area by the models. The omission errors are generally between 45 and 85%, indicating that a large percentage of the landslides are missed by the models.

Table 4.3: Summary of model accuracy, commission error, and omission error for all six quadrangles of the study area, for a displacement threshold of 15 cm.

| | | J-(Ia) | J-(PGA) | J-(PGA,Ia) | RS-(PGA,M) | RS-(PGA,PGV) | RS-(PGA, Ia) | RS-(PGA,PGV,Ia) |
|---|---|---|---|---|---|---|---|---|
| 1. PIRU | % Accuracy | 89.1% | 90.1% | 89.1% | 88.1% | 88.9% | 88.5% | 88.9% |
| | % Commission Errors | 96.3% | 96.4% | 96.4% | 96.3% | 96.3% | 96.3% | 96.3% |
| % LS Area: 1.2% | % Omission Errors | 68.0% | 72.0% | 68.4% | 64.7% | 67.2% | 65.8% | 66.9% |
| 2. VAL VERDE | % Accuracy | 95.4% | 96.2% | 95.6% | 95.1% | 94.8% | 94.9% | 94.8% |
| | % Commission Errors | 89.8% | 88.9% | 89.6% | 90.1% | 90.3% | 90.2% | 90.2% |
| % LS Area: 1.7% | % Omission Errors | 78.8% | 83.0% | 79.8% | 77.7% | 75.9% | 76.5% | 75.9% |
| 3. NEWHALL | % Accuracy | 99.7% | 99.8% | 99.7% | 99.7% | 99.6% | 99.6% | 99.6% |
| | % Commission Errors | 87.1% | 83.1% | 85.3% | 86.8% | 88.2% | 88.6% | 88.4% |
| % LS Area: 0.2% | % Omission Errors | 81.8% | 88.8% | 83.6% | 79.9% | 71.9% | 77.4% | 73.5% |
| 4. SIMI VALLEY | % Accuracy | 99.5% | 99.5% | 99.5% | 99.4% | 99.5% | 99.4% | 99.5% |
| | % Commission Errors | 81.9% | 79.7% | 81.3% | 82.3% | 81.5% | 82.7% | 82.0% |
| % LS Area: 0.3% | % Omission Errors | 82.1% | 83.9% | 82.6% | 81.3% | 83.1% | 81.1% | 82.5% |
| 5. SANTA SUSANA | % Accuracy | 98.2% | 98.6% | 98.3% | 98.0% | 97.7% | 97.8% | 97.7% |
| | % Commission Errors | 80.9% | 77.0% | 80.2% | 81.9% | 83.2% | 82.7% | 83.1% |
| % LS Area: 1.0% | % Omission Errors | 76.7% | 85.4% | 78.6% | 72.7% | 69.2% | 69.8% | 69.0% |
| 6. OAT MOUNTAIN | % Accuracy | 96.9% | 98.5% | 97.4% | 96.6% | 95.6% | 95.6% | 95.4% |
| | % Commission Errors | 93.9% | 91.5% | 93.4% | 94.2% | 94.9% | 94.8% | 94.9% |
| % LS Area: 0.6% | % Omission Errors | 69.3% | 83.5% | 73.6% | 67.9% | 61.7% | 62.0% | 60.9% |
| **AVERAGE** | **% Accuracy** | **96.5%** | **97.1%** | **96.6%** | **96.2%** | **96.0%** | **96.0%** | **96.0%** |
| **AVERAGE** | **% Commission Errors** | **88.3%** | **86.1%** | **87.7%** | **88.6%** | **89.1%** | **89.2%** | **89.2%** |
| **AVERAGE** | **% Omission Errors** | **76.1%** | **82.8%** | **77.8%** | **74.0%** | **71.5%** | **72.1%** | **71.4%** |

Table 4.4: Summary of model accuracy, commission error, and omission error for all six quadrangles of the study area, for a displacement threshold of 5 cm.

| | | J-(Ia) | J-(PGA) | J-(PGA,Ia) | RS-(PGA,M) | RS-(PGA,PGV) | RS-(PGA, Ia) | RS-(PGA,PGV,Ia) |
|---|---|---|---|---|---|---|---|---|
| 1. PIRU | % Accuracy | 87.2% | 87.4% | 87.4% | 84.3% | 85.5% | 85.0% | 85.4% |
| | % Commission Errors | 96.3% | 96.4% | 96.3% | 96.4% | 96.3% | 96.3% | 96.3% |
| % LS Area: 1.2% | % Omission Errors | 61.4% | 63.0% | 62.6% | 53.1% | 55.8% | 54.1% | 55.4% |
| 2. VAL VERDE | % Accuracy | 94.3% | 95.1% | 94.8% | 93.2% | 92.6% | 92.9% | 92.7% |
| | % Commission Errors | 90.6% | 90.2% | 90.3% | 91.2% | 91.5% | 91.4% | 91.5% |
| % LS Area: 1.7% | % Omission Errors | 73.4% | 77.9% | 75.9% | 69.1% | 66.7% | 67.6% | 66.8% |
| 3. NEWHALL | % Accuracy | 99.5% | 99.7% | 99.6% | 99.3% | 98.9% | 99.1% | 99.0% |
| | % Commission Errors | 90.7% | 86.2% | 88.1% | 91.6% | 93.4% | 93.2% | 93.4% |
| % LS Area: 0.2% | % Omission Errors | 73.6% | 81.4% | 77.2% | 66.8% | 56.6% | 63.3% | 58.4% |
| 4. SIMI VALLEY | % Accuracy | 99.4% | 99.4% | 99.4% | 99.3% | 99.4% | 99.3% | 99.3% |
| | % Commission Errors | 84.0% | 82.5% | 83.1% | 85.1% | 84.5% | 85.6% | 84.9% |
| % LS Area: 0.3% | % Omission Errors | 79.3% | 80.7% | 80.4% | 76.6% | 78.9% | 76.3% | 78.0% |
| 5. SANTA SUSANA | % Accuracy | 97.4% | 98.2% | 97.8% | 96.4% | 95.9% | 96.0% | 95.9% |
| | % Commission Errors | 84.2% | 81.0% | 82.8% | 86.8% | 87.7% | 87.6% | 87.8% |
| % LS Area: 1.0% | % Omission Errors | 64.9% | 75.5% | 69.0% | 54.8% | 51.8% | 51.6% | 51.3% |
| 6. OAT MOUNTAIN | % Accuracy | 94.5% | 97.3% | 95.9% | 93.1% | 91.3% | 91.4% | 91.1% |
| | % Commission Errors | 95.4% | 93.5% | 94.7% | 95.9% | 96.4% | 96.4% | 96.5% |
| % LS Area: 0.6% | % Omission Errors | 56.9% | 72.3% | 63.7% | 51.4% | 45.0% | 45.4% | 44.3% |
| **AVERAGE** | **% Accuracy** | **95.4%** | **96.2%** | **95.8%** | **94.3%** | **93.9%** | **93.9%** | **93.9%** |
| **AVERAGE** | **% Commission Errors** | **90.2%** | **88.3%** | **89.2%** | **91.2%** | **91.6%** | **91.8%** | **91.7%** |
| **AVERAGE** | **% Omission Errors** | **68.2%** | **75.1%** | **71.5%** | **62.0%** | **59.1%** | **59.7%** | **59.0%** |

### 4.3.2 Landslide-by-landslide Comparison

The percentages of landslides captured (% LS Captured) by each model for all six quadrangles are compiled in Table 4.5 for a displacement threshold of 15 cm and in Table 4.6 for a displacement threshold of 5 cm. Referring back to Chapter 3, a landslide is considered "captured" if at least 50% of observed landslide cells within the landslide are predicted to be landslide cells (i.e. the predicted displacements exceed the threshold value). The % LS Captured values range from as small as 4 to 5% in the Simi Valley quadrangle (15 cm threshold) to as large as 45 to 55% in the Oat Mountain quadrangle (5 cm threshold). Compared with the %GFC values determined from the cell-by-cell analysis, the % LS Captured values are about 8 to 10 percentage points smaller. There are a few exceptions, such as Model RS-($PGA$, $M$) in Oat Mountain, which captured 53.3% of the landslides (Table 4.6) versus 48.6% of landslide cells (Table 4.2). The results between quadrangles are also more varied when using the landslide-by-landslide approach rather than the cell-by-cell approach. For example, model RS-($PGA$, $PGV$) with the 5 cm threshold captures 54.1% of landslides in Oat Mountain and 8.3% of landslides in Simi Valley when using the landslide-by-landslide approach. The same model and threshold resulted in % GFC values of 55% and 21.1% using the cell-by-cell approach in these two quadrangles.

Similar to the results from the cell-by-cell analysis, the models that predict displacement as a function of more than one ground motion parameter perform better than the models that use only one ground motion parameter. Model RS-($PGA, PGV$) captures the largest percentage of landslides ( 20.5%, 33.7% for the 15 cm, 5 cm thresholds, respectively), and Model J-(PGA) captures the smallest percentage of landslides (10.6%, 17.4%).

Table 4.5: Summary of landslide-by-landslide analysis for all six quadrangles of the study area, for a displacement threshold of 15 cm

| | | J-(Ia) | J-(PGA) | J-(PGA,Ia) | RS-(PGA,M) | RS-(PGA,PGV) | RS-(PGA, Ia) | RS-(PGA,PGV,Ia) |
|---|---|---|---|---|---|---|---|---|
| 1. PIRU<br>% LS Area: 1.2% | % LS Captured | 27.8% | 23.8% | 27.4% | 32.1% | 28.9% | 30.6% | 29.2% |
| 2. VAL VERDE<br>% LS Area: 1.7% | % LS Captured | 14.9% | 10.9% | 13.8% | 16.0% | 17.7% | 17.0% | 17.7% |
| 3. NEWHALL<br>% LS Area: 0.2% | % LS Captured | 9.6% | 5.5% | 8.0% | 10.4% | 15.4% | 11.5% | 14.3% |
| 4. SIMI VALLEY<br>% LS Area: 0.3% | % LS Captured | 4.7% | 3.8% | 4.2% | 5.1% | 4.2% | 4.2% | 4.5% |
| 5. SANTA SUSANA<br>% LS Area: 1.0% | % LS Captured | 16.4% | 8.2% | 14.2% | 19.3% | 22.7% | 21.8% | 22.8% |
| 6. OAT MOUNTAIN<br>% LS Area: 0.6% | % LS Captured | 25.2% | 11.5% | 20.4% | 26.9% | 33.9% | 33.1% | 34.6% |
| **AVERAGE** | **% LS Captured** | **16.4%** | **10.6%** | **14.7%** | **18.3%** | **20.5%** | **19.7%** | **20.5%** |

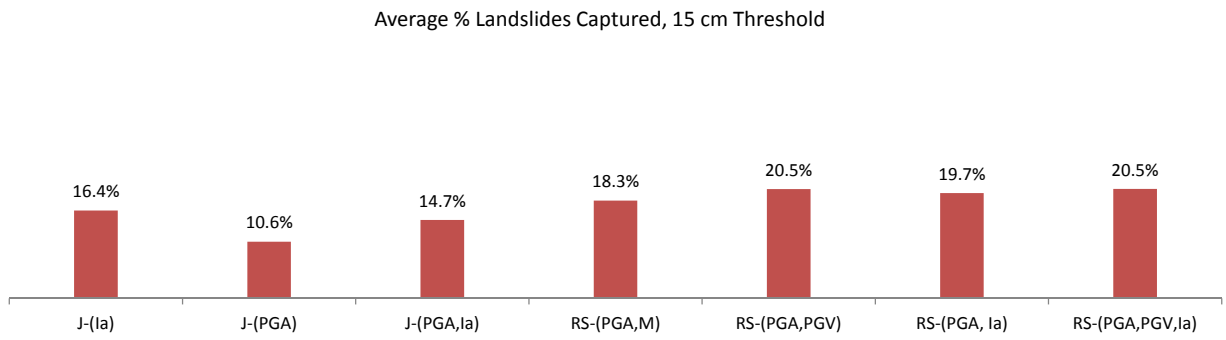

Table 4.6: Summary of landslide-by-landslide analysis for all six quadrangles of the study area, for a displacement threshold of 5 cm

| | | J-(Ia) | J-(PGA) | J-(PGA,Ia) | RS-(PGA,M) | RS-(PGA,PGV) | RS-(PGA, Ia) | RS-(PGA,PGV,Ia) |
|---|---|---|---|---|---|---|---|---|
| 1. PIRU<br>% LS Area: 1.2% | % LS Captured | 35.1% | 33.8% | 34.3% | 42.5% | 40.9% | 41.0% | 43.2% |
| 2. VAL VERDE<br>% LS Area: 1.7% | % LS Captured | 20.6% | 15.8% | 17.8% | 26.7% | 27.8% | 27.6% | 25.2% |
| 3. NEWHALL<br>% LS Area: 0.2% | % LS Captured | 13.2% | 10.4% | 11.3% | 23.4% | 29.1% | 26.6% | 19.8% |
| 4. SIMI VALLEY<br>% LS Area: 0.3% | % LS Captured | 7.2% | 5.5% | 6.2% | 7.2% | 8.3% | 9.8% | 10.0% |
| 5. SANTA SUSANA<br>% LS Area: 1.0% | % LS Captured | 26.6% | 17.4% | 22.3% | 42.2% | 42.3% | 43.2% | 37.7% |
| 6. OAT MOUNTAIN<br>% LS Area: 0.6% | % LS Captured | 39.5% | 21.6% | 31.7% | 53.3% | 54.1% | 54.6% | 45.9% |
| **AVERAGE** | **% LS Captured** | **23.7%** | **17.4%** | **20.6%** | **32.5%** | **33.7%** | **33.8%** | **30.3%** |

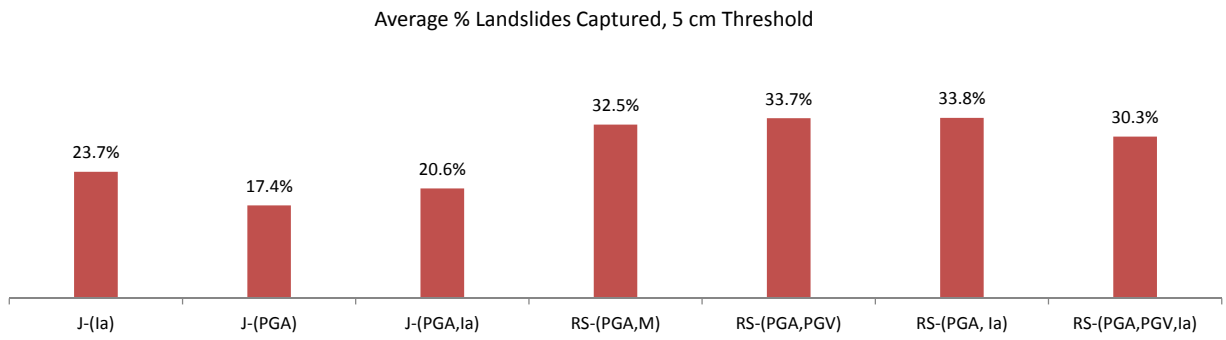

Because the landslide-by-landslide approach does not take into account the size of the landslide – missing a 2-cell landslide counts the same as missing a 30-cell landslide – a model may capture a large percentage of landslide cells and still perform poorly if the cells it misses are all small, individual landslides. If the distribution of landslides within a quadrangle is weighted towards smaller landslides, this could help explain why the majority of models captured a smaller percentage of landslides versus landslide cells.

The distributions of landslides within the Oat Mountain and Simi Valley quadrangles are plotted in Figures 4.11 and 4.12, respectively, as a function of landslide size (i.e. number of cells in each landslide), and the percentage of each landslide captured by Model RS-($PGA$, $PGV$) with a displacement threshold of 5 cm. The data are also summarized in Tables 4.7 and 4.8. The distributions of landslide size within these two quadrangles are generally representative of the distributions across all six quadrangles, but the results are very different. Oat Mountain contains 1,259 individual landslides, 54.1% of which are captured by Model RS-($PGA$, $PGV$). Simi Valley contains 471 individual landslides, 8.3% of which are captured by the same model.

Figure 4.11 shows that nearly 40% of the landslides within Oat Mountain are 1 or 2-cell landslides, but it also shows that the model captured 50.6% of these small landslides, very close to the average for the entire quadrangle (54.1%). The percentage of landslides that were completely missed (0% cells captured) gradually decreases with increasing landslide size, indicating that the model did a slightly better job capturing the larger landslides, but overall the distribution is not heavily skewed one way or the other. In comparison, Figure 4.12 shows that about 27% of the landslides within Simi Valley are 1 or 2-cell landslides, and the model captured about 7% of these small landslides, also very close to the average for the quadrangle (8.3%). What is surprising is that 79% of landslides are completely missed, and most of them are larger than 2 cells in size.

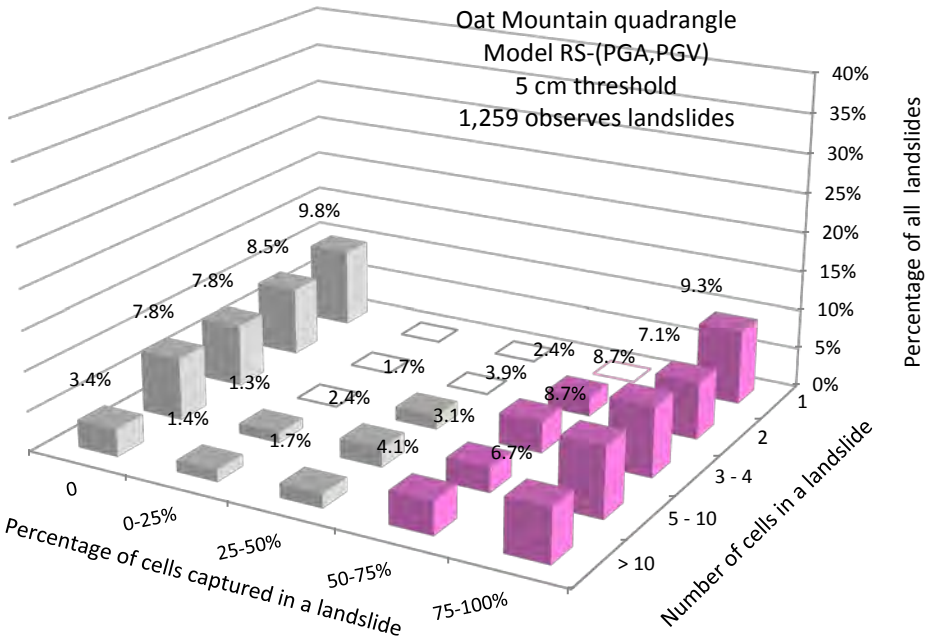


Figure 4.11: Distribution of landslides within the Oat Mountain quadrangle as a function of landslide size (number of cells) and the percentage of cells captured by Model RS-(PGA,PGV).

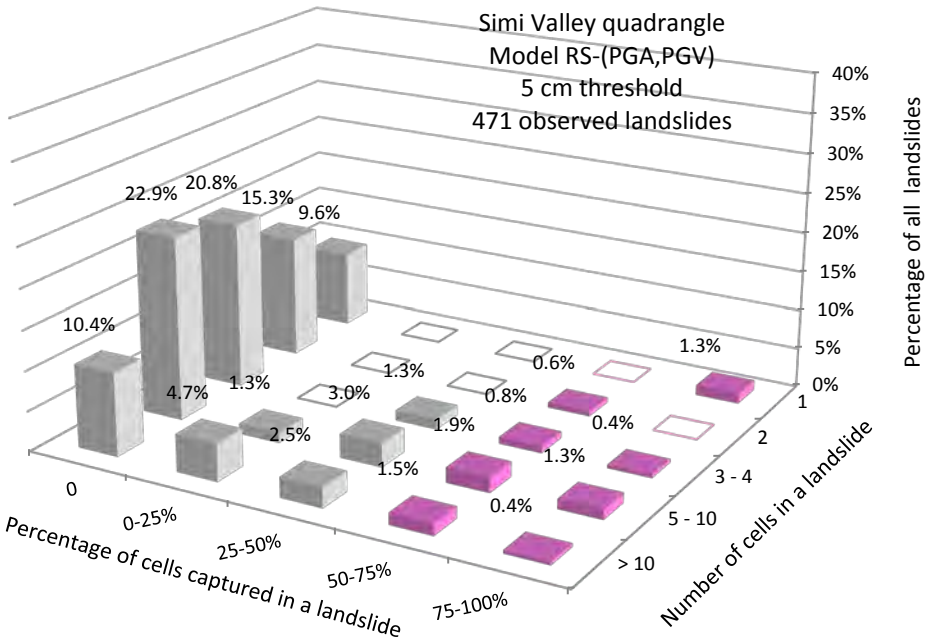


Figure 4.12: Distribution of landslides within the Simi Valley quadrangle as a function of landslide size (number of cells) and the percentage of cells captured by Model RS-(PGA,PGV).

Table 4.7: Distribution of observed landslides within the Oat Mountain quadrangle as a function of landslide size and the percentage of cells captured by model RS-(PGA,PGV) with a 5 cm threshold.

| Percentage of cells captured in each landslide | Number of cells in each landslide: 1 | 2 | 3 - 4 | 5 - 10 | > 10 | |
|---|---|---|---|---|---|---|
| **0** | 9.8% | 8.5% | 7.8% | 7.8% | 3.4% | **37.3%** |
| **0-25%** | 0.0% | 0.0% | 0.0% | 1.3% | 1.4% | **2.7%** |
| **25-50%** | 0.0% | 0.0% | 1.7% | 2.4% | 1.7% | **5.9%** |
| **50-75%** | 0.0% | 2.4% | 3.9% | 3.1% | 4.1% | **13.5%** |
| **75-100%** | 9.3% | 7.1% | 8.7% | 8.7% | 6.7% | **40.6%** |
| | **19.1%** | **18.0%** | **22.2%** | **23.3%** | **17.4%** | |

Table 4.8: Distribution of observed landslides within the Simi Valley quadrangle as a function of landslide size and the percentage of cells captured by model RS-(PGA,PGV) with a 5 cm threshold.

| Percentage of cells captured in each landslide | Number of cells in each landslide: 1 | 2 | 3 - 4 | 5 - 10 | > 10 | |
|---|---|---|---|---|---|---|
| **0** | 9.6% | 15.3% | 20.8% | 22.9% | 10.4% | **79.0%** |
| **0-25%** | 0.0% | 0.0% | 0.0% | 1.3% | 4.7% | **5.9%** |
| **25-50%** | 0.0% | 0.0% | 1.3% | 3.0% | 2.5% | **6.8%** |
| **50-75%** | 0.0% | 0.6% | 0.8% | 1.9% | 1.5% | **4.9%** |
| **75-100%** | 1.3% | 0.0% | 0.4% | 1.3% | 0.4% | **3.4%** |
| | **10.8%** | **15.9%** | **23.4%** | **30.4%** | **19.5%** | |

In summary, the results of Model RS-($PGA$, $PGV$) were consistently good for all landslides within the Oat Mountain quadrangle, and consistently poor for all landslides within the Simi Valley quadrangle. Because the distribution of landslide size within each quadrangle was similar, the difference in performance between the two quadrangles does not appear to reflect significant bias from smaller landslides. Referring back to Table 4.2, model RS-($PGA$, $PGV$) predicted landslides to cover approximately 8.7% of the Oat Mountain quadrangle, and the actual landslides covered only 0.6% of the quadrangle. This suggests that the model is simply missing the landslides, perhaps due to poor

estimates of the ground motions or shear strengths, inaccuracies in slope angle caused by the resolution of the DEM, or because of the limits of the simple sliding block model used. Figure 4.13 shows an example of a 3-cell landslide within Oat Mountain. The landslide is completely missed by the model, but cells immediately adjacent to the landslide are identified.

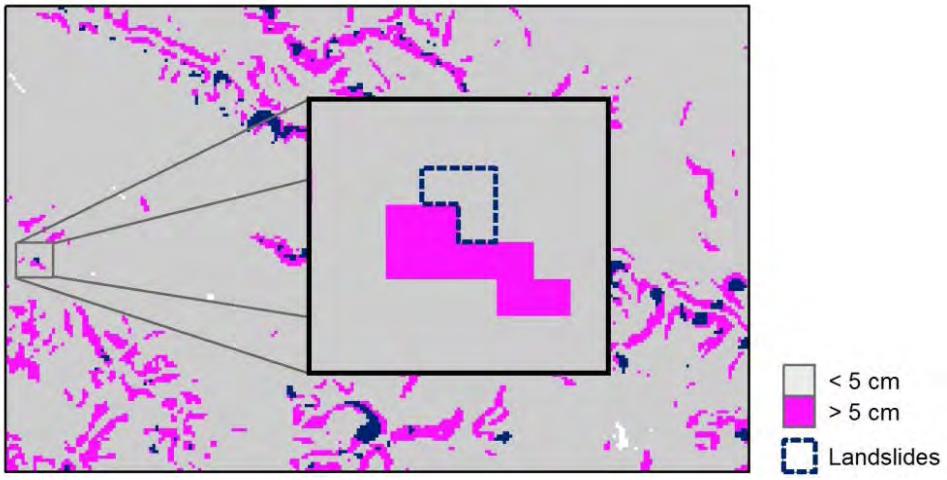


Figure 4.13: Example of a three-cell landslide within the Oat Mountain quadrangle that was missed by Model RS-(PGA, PGV) with a 5 cm threshold.

### 4.3.3 Influence of Geologic Unit and Slope Angle on Model Accuracy

After evaluating the accuracy of the different predictive models, the distribution of observed and predicted landslide cells within individual geologic units was analyzed. The results of Model RS-(PGA, PGV) with a 5 cm threshold in the Oat Mountain quadrangle are shown in Table 4.9 as a function of geologic unit.

Table 4.9: Distribution of observed and predicted landslide cells across geologic units in the Oat Mountain quadrangle using Model RS-(PGA, PGV) and a 5 cm threshold

| | | | | Observed LS Cells | | | Predicted LS Cells | | Accurate | |
|---|---|---|---|---|---|---|---|---|---|---|
| | | | | **9,445** | | | **143,418** | | **5,197** | |
| Strength Group | ϕ'(°) | c'(kPa) | Geologic Unit | CELLS | % of LS cells | % of G.Unit | CELLS | % of G.Unit | CELLS | %GFC in G. Unit |
| 1 | 39 | 31.3 | Tl | 49 | 0.52% | 1.91% | 0 | 0.00% | 0 | 0.00% |
| 1 | 39 | 31.3 | Tlc | | 0.00% | 0.00% | 0 | 0.00% | 0 | 0.00% |
| 1 | 39 | 31.3 | Tss | 6 | 0.06% | 0.56% | 0 | 0.00% | 0 | 0.00% |
| 1 | 39 | 31.3 | Tsc1 | 5 | 0.05% | 0.08% | 0 | 0.00% | 0 | 0.00% |
| 1 | 39 | 31.3 | Tsc2 | 2 | 0.02% | 0.04% | 0 | 0.00% | 0 | 0.00% |
| 1 | 39 | 31.3 | Tsc3 | 126 | 1.33% | 1.42% | 0 | 0.00% | 0 | 0.00% |
| 1 | 39 | 31.3 | Kc | 166 | 1.76% | 0.22% | 0 | 0.00% | 0 | 0.00% |
| 1 | 39 | 31.3 | Tm | 395 | 4.18% | 0.52% | 0 | 0.00% | 0 | 0.00% |
| 1 | 39 | 31.3 | Tm1/4/5/s | 373 | 3.95% | 0.38% | 0 | 0.00% | 0 | 0.00% |
| 1 | 39 | 31.3 | Tm2 | 66 | 0.70% | 0.36% | 0 | 0.00% | 0 | 0.00% |
| 1 | 39 | 31.3 | Tm3 | 14 | 0.15% | 0.15% | 0 | 0.00% | 0 | 0.00% |
| 1 | 39 | 31.3 | Tmd | 252 | 2.67% | 3.31% | 0 | 0.00% | 0 | 0.00% |
| 1 | 39 | 31.3 | Tt | 128 | 1.36% | 0.81% | 0 | 0.00% | 0 | 0.00% |
| 1 | 39 | 31.3 | Ttb | 21 | 0.22% | 1.36% | 0 | 0.00% | 0 | 0.00% |
| 1 | 39 | 31.3 | Tt1/3 | 6 | 0.06% | 0.40% | 0 | 0.00% | 0 | 0.00% |
| 1 | 39 | 31.3 | Tt2/4 | 79 | 0.84% | 0.74% | 0 | 0.00% | 0 | 0.00% |
| 2 | 32 | 13.3 | Tp | 145 | 1.54% | 1.01% | 1461 | 10.22% | 74 | 51.03% |
| 2 | 32 | 13.3 | Tpc | 1275 | 13.50% | 2.50% | 13004 | 25.53% | 928 | 72.78% |
| 2 | 32 | 13.3 | Qsw | 16 | 0.17% | 0.03% | 908 | 1.67% | 10 | 62.50% |
| 2 | 32 | 13.3 | Tw | 3559 | 37.68% | 1.66% | 87541 | 40.80% | 2810 | 78.95% |
| 2 | 32 | 13.3 | Twc | 557 | 5.90% | 1.12% | 18304 | 36.66% | 419 | 75.22% |
| 2 | 32 | 13.3 | Qs | 402 | 4.26% | 0.27% | 6016 | 4.10% | 268 | 66.67% |
| 2 | 32 | 13.3 | Qsu | 50 | 0.53% | 0.10% | 2626 | 5.01% | 19 | 38.00% |
| 2 | 32 | 13.3 | Qsm | 429 | 4.54% | 0.47% | 4468 | 4.89% | 204 | 47.55% |
| 3 | 28 | 19.6 | acf, af | 16 | 0.17% | 0.32% | 42 | 0.84% | 10 | 62.50% |
| 3 | 28 | 19.6 | rf | | 0.00% | 0.00% | 0 | | | |
| 3 | 28 | 19.6 | Qc | | 0.00% | 0.00% | 9 | 0.40% | | 0.00% |
| 3 | 28 | 19.6 | Tps | 845 | 8.95% | 1.50% | 2806 | 4.98% | 272 | 32.19% |
| 3 | 28 | 19.6 | Tws | 349 | 3.70% | 1.07% | 4498 | 13.84% | 174 | 49.86% |
| 3 | 28 | 19.6 | Qal, Qay/1/2, Qp | 1 | 0.01% | 0.00% | 127 | 0.04% | | 0.00% |
| 3 | 28 | 19.6 | Qao | 9 | 0.10% | 0.02% | 81 | 0.20% | 1 | 11.11% |
| 3 | 28 | 19.6 | Qt | | 0.00% | 0.00% | 10 | 0.41% | | 0.00% |
| 3 | 28 | 19.6 | Qto | 1 | 0.01% | 0.05% | 11 | 0.53% | 1 | 100.00% |
| 4 | 25 | 22.3 | Qls | 103 | 1.09% | 0.14% | 1506 | 2.10% | 7 | 6.80% |

The data show that zero landslides were predicted within any of the geologic units in Strength Group 1 (which represents the largest set of shear strength values) despite nearly 20% of the landslides observed in the Oat Mountain quadrangle occurring within these geologic units. The majority of landslides (~68%) occurred within geologic units in Strength Group 2, and the model was very accurate within this strength group, capturing between 38% and 79% of the observed landslide source cells within each geologic unit. However, the ratio of predicted to observed landslide cells was very large. The highest percentage of landslide cells captured is 79% in geologic unit Tw, but the analysis predicts 41% of that geologic unit to be landslides while only 1.6% of the unit experienced landslides. The fewest landslides occurred in Strength Groups 3 and 4 and almost all of them occurred in two geologic units, Tps and Tws.

Figure 4.14 shows the distribution of slope angles for all cells, the distribution of slope angles for the observed landslide cells, and the percentage of observed landslide cells within each slope angle bin for three different geologic units; Tm (Modelo formation; see Table 3.1) from Strength Group 1, Tw (Towsley formation) from Strength Group 2, and Tps (Pico formation) from Strength Group 3. These three geologic units contain 51% of all the landslide cells observed in the quadrangle, with the Tm unit contributing 4.2%, the Tw unit contributing 37.7%, and the Tps unit contributing 8.9%.

Approximately 65% of the slopes within the Tm unit are between 20 and 40 degrees, and no slopes are greater than 60 degrees. Most of the landslides (~80%) in this unit occurred on slopes between 30 and 50 degrees. The percentage of area within each slope bin that is covered by landslides increases with increasing slope angle. The large strength assigned to this unit resulted in the model predicting landslides (i.e. displacements greater than 5 cm) only on slopes steeper than about 63° (i.e. a slope

threshold of 63°). As a result, no landslides were predicted. These results indicate that perhaps the assigned strength for the Tm unit was too large.

The distribution of slope angles within geologic unit Tw shows a larger number of steep slopes, and similar to the Tm unit, most of the landslides (~80%) occurred on slopes of 30 to 50 degrees. Again, the percentage of slopes covered by landslides increases with increasing slope angle. The strength assigned to unit Tw is smaller than for unit Tm, and the slope threshold (representing a displacement of 5 cm) is about 34°. Because the strength is constant for all slopes within geologic unit Tw, all slopes steeper than about 34° are predicted to fail. The %GFC is large for this geologic unit (79%, see Table 4.9) due to the fact that a large percentage of the observed landslides occurred on slopes steeper than 34°. All landslides on slopes steeper than 34° are captured, but at the expense of predicting all of these slopes will fail. As Figure 4.14 shows, the percentage of landslide cells within a slope angle bin never approaches 100%.

Lastly, the distribution of slope angles within geologic unit Tps looks almost identical to that of the Tm unit, and a similar distribution of slope angles is seen within the observed landslide cells. However, the strength assigned to the Tps unit is lower than the strength assigned to the Tm unit, such that the slope threshold (representing a displacement of 5 cm) is 39° and 32% of the landslides were accurately identified.

One other interesting observation is that the slope threshold for Tps (Strength Group 3) is larger than for Tw (Strength Group 2), although Strength Group 3 is considered the “weaker” strength group in the CGS seismic hazard zone report for Oat Mountain (CDMG, 1997b) based on the assigned friction angles (28° vs. 32°). However, because the cohesion assigned to the Tps unit (19.6 kPa) is 50% larger than the cohesion assigned to the Tw unit (13.3 kPa), at the small confining pressures considered for the infinite slope analyses used in this study the strength of Tps is larger than Tw.

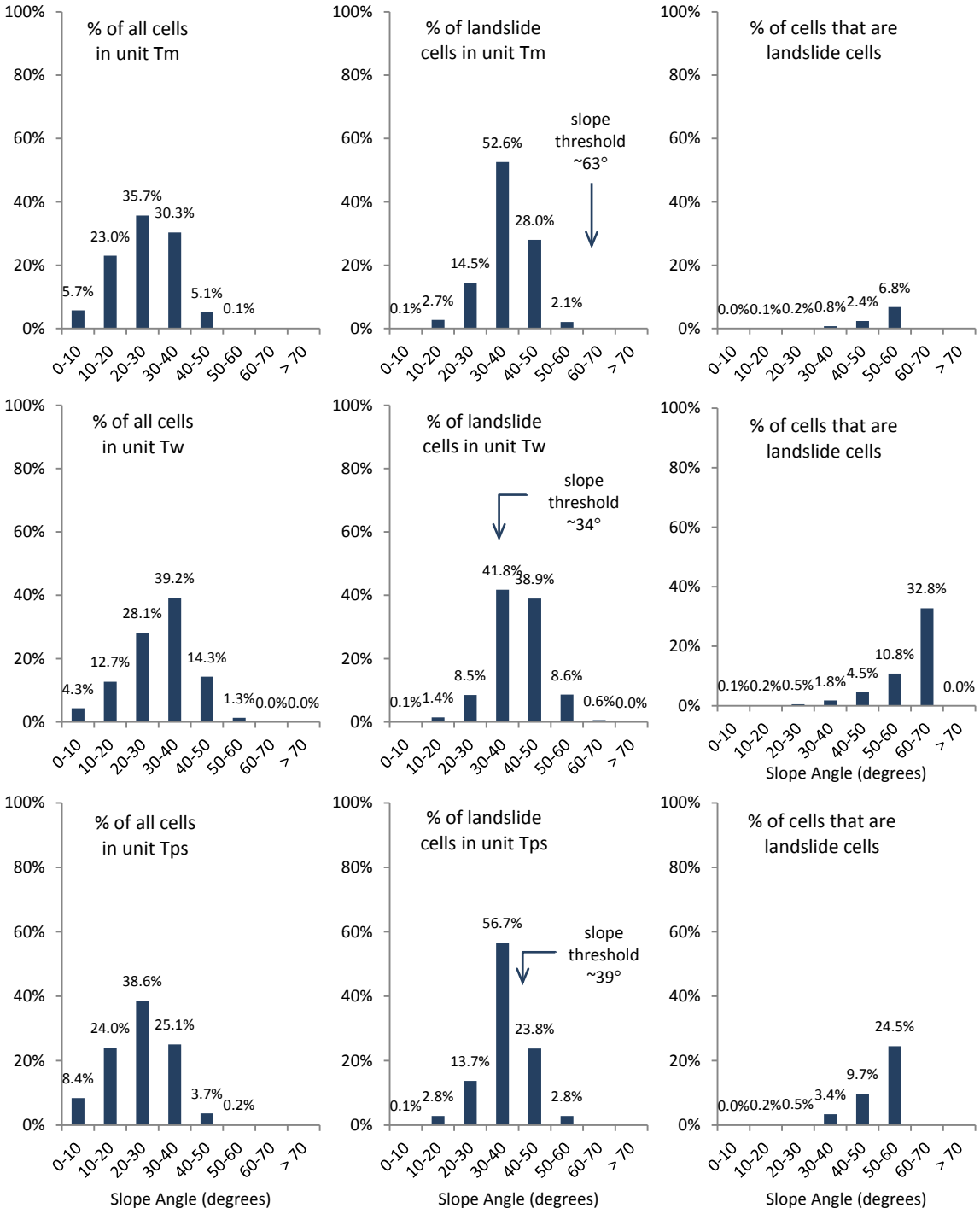


Figure 4.14: Distribution of slope angles for all cells and all observed landslide cells in the Oat Mountain quadrangle within geologic units (a) Tm, in Strength Group 1, (b) Tw, in Strength Group 2, and (c) Tps, in Strength Group 3.

As noted, if the shear strength across a geologic unit is constant, as is the case in this study, the prediction of landslides (displacement) within that unit becomes a function of slope angle. If the assigned strength is high, the model will only predict landslides in the steepest slopes and may miss most or all of the observed landslides. If the assigned strength is low, the model will predict landslides in many of the flatter slopes, where the observed landslide density is smaller. This will result in a larger percentage of landslides captured but also a significant over-prediction in the total landslide area. The distributions in Figure 4.14 indicate that there is significant spatial variability of shear strength within individual geologic units, which explains why some 60° slopes remain stable while some 20° slopes fail within the same geologic unit. It is very difficult to evaluate and assign spatial variations in strength properties for a regional-scale analysis, and it will likely continue to be a challenge in the short-term.

## 4.4 INFLUENCE OF SHEAR STRENGTH ON LANDSLIDE PREDICTIONS

The influence of geologic material strengths on the displacement and landslide predictions using model RS-($PGA$, $PGV$) is evaluated in this section. Model RS-($PGA, PGV$) is evaluated using the cell-by-cell approach with a 5 cm displacement threshold and three different sets of shear strength values; (Case I) strengths used by Jibson et al. (2000) and documented in Table 2.5, (Case II) strengths used in this study and documented in Table 3.1, and (Case III) strengths used by CGS ($\varphi'$ from Table 3.1, $c' = 0$). The influence of material strengths is evaluated within the Oat Mountain quadrangle only.

Figure 4.15 shows predicted displacements within the representative region in Oat Mountain using model RS-($PGA$, $PGV$) and three different sets of shear strength parameters. Case I is based on strengths used by Jibson et al. (2000) and results in the smallest concentration of large displacements. Case II represents the strengths used in this study and results in a greater area of large displacements. Case III is based on the approach used by CGS that ignores cohesion ($c' = 0$) and results in large displacements across the majority of the representative region.

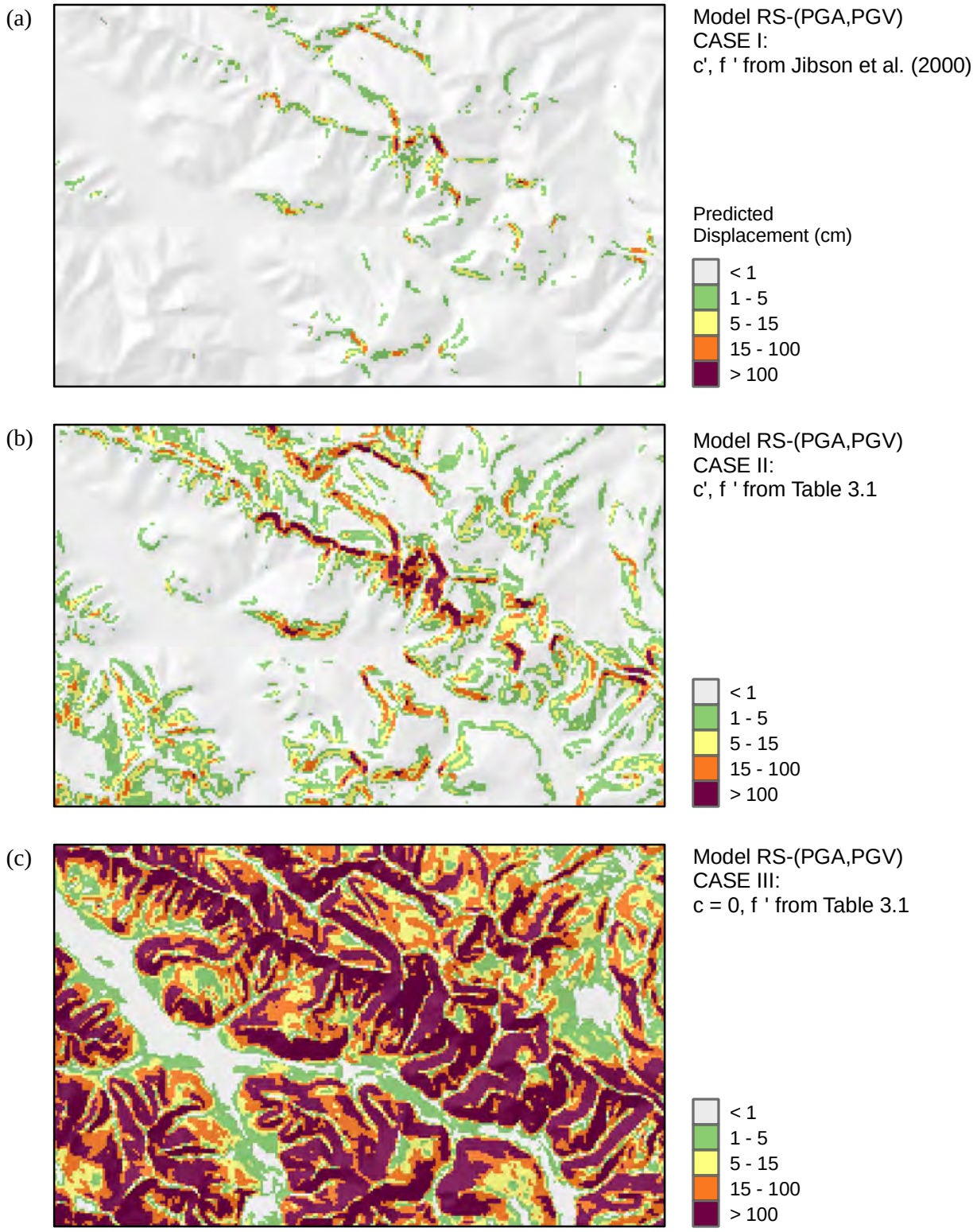


Figure 4.15: Displacements predicted within a representative region of the Oat Mountain quadrangle using model RS-(PGA, PGV) and three different sets of shear strength values.

Figure 4.16 shows a comparison of observed landslides and predicted landslides (for a displacement threshold of 5 cm) using Model RS-($PGA$, $PGV$) and the three different sets of shear strength values. Case I covers 0.3% of the Oat Mountain quadrangle with predicted landslide cells, and captures only 6.8% of observed landslide cells. Case II covers 8.7% of the quadrangle with predicted landslide cells, and captures 55% of observed landslide cells. Case III covers 49.3% of the quadrangle with predicted landslide cells, and captures 97% of observed landslide cells.

A summary of results across all six quadrangles is provided in Table 4.10. On average Case I only captures 3% of the landslide cells, while Case II captures 41% and Case III captures 95% of the landslide cells. The results show that increasing strengths across entire geologic units in order to make a small number of statically unstable cells stable – i.e. the approach used by Jibson et al. (2000) in Case I – results in predicted displacements that are too small to capture a large percentage of observed landslide cells. In contrast, ignoring any contribution of cohesion in the slope stability analysis – i.e. the approach used by CGS (Case III) – results in predicted displacements that are too large across many flatter slopes and grossly overestimates the area of earthquake-induced landslide hazard. On average Case III predicts landslides for 41% of the study area, which is about 50 times larger an area than the observed landslide area (i.e. %QC / % LS Area ≈ 50%). The efficiency in Oat Mountain for Case III (46.3%) is almost identical to that for Case II (47.9%), despite the large difference in the ratios of % QC to % LS Area (86 for Case III, 15 for Case II). These results point to the severe over-prediction of landslides using the CGS approach to assigning shear strengths.

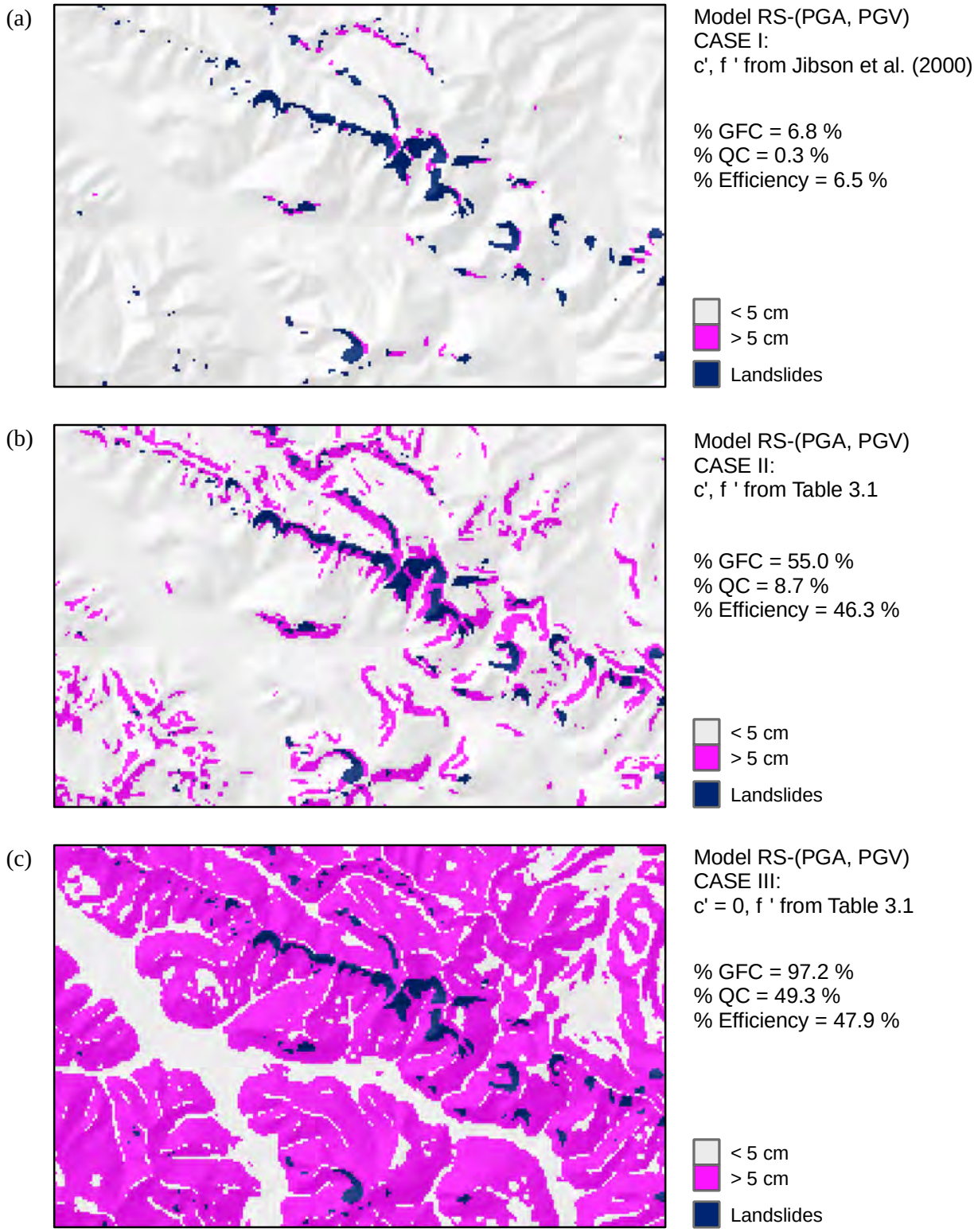


Figure 4.16: Comparison of observed and predicted landslides within a representative region of the Oat Mountain quadrangle using Model RS-(PGA, PGA) with a 5 cm threshold and three different sets of shear strength values

Table 4.10: Summary of results for all six quadrangles of the study area using Model RS-(PGA, PGV) with a 5 cm threshold and three different sets of shear strength values

| | | Case I | Case II | Case III |
|---|---|---|---|---|
| 1. PIRU | % GFC | 0.5% | 44.2% | 97.0% |
| | % QC | 0.0% | 14.4% | 64.0% |
| % LS Area: 1.2% | % Efficiency | 0.4% | 29.8% | 33.0% |
| | % QC/% LS Area | 0.0 | 12.0 | 53.3 |
| 2. VAL VERDE | % GFC | 4.9% | 33.3% | 95.4% |
| | % QC | 0.2% | 6.8% | 54.2% |
| % LS Area: 1.7% | % Efficiency | 4.6% | 26.5% | 41.2% |
| | % QC/% LS Area | 0.1 | 3.9 | 31.3 |
| 3. NEWHALL | % GFC | 4.8% | 43.4% | 92.8% |
| | % QC | 0.0% | 1.0% | 29.4% |
| % LS Area: 0.2% | % Efficiency | 4.8% | 42.4% | 63.4% |
| | % QC/% LS Area | 0.3 | 6.6 | 185.5 |
| 4. SIMI VALLEY | % GFC | 0.9% | 21.1% | 80.1% |
| | % QC | 0.0% | 0.4% | 13.0% |
| % LS Area: 0.3% | % Efficiency | 0.8% | 20.7% | 67.2% |
| | % QC/% LS Area | 0.0 | 1.4 | 39.2 |
| 5. SANTA SUSANA | % GFC | 2.2% | 48.2% | 94.5% |
| | % QC | 0.1% | 4.0% | 37.8% |
| % LS Area: 1.0% | % Efficiency | 2.1% | 44.2% | 56.7% |
| | % QC/% LS Area | 0.1 | 3.9 | 36.9 |
| 6. OAT MOUNTAIN | % GFC | 6.8% | 55.0% | 97.2% |
| | % QC | 0.3% | 8.7% | 49.3% |
| % LS Area: 0.6% | % Efficiency | 6.5% | 46.3% | 47.9% |
| | % QC/% LS Area | 0.5 | 15.2 | 85.9 |
| **AVERAGE** | **% GFC** | **3.3%** | **41.0%** | **94.7%** |
| **AVERAGE** | % QC | 0.1% | 5.9% | 41.2% |
| **AVERAGE** | % Efficiency | 3.2% | 35.1% | 53.5% |
| **AVERAGE** | % QC/% LS Area | 0.1 | 7.1 | 49.5 |

# Chapter 5

# Conclusions

## 5.1 SUMMARY AND CONCLUSIONS

This thesis presented a comparison of methodologies for predicting earthquake-induced landslides using permanent displacement analysis. Regional estimates of sliding displacement were computed within a Geographic Information System (GIS) and compared with locations of observed landslides within six quadrangles shaken by the 1994 Northridge, California earthquake. This study area was chosen because of the availability of a comprehensive inventory of over 11,000 landslides triggered during the Northridge earthquake and nearly 200 strong-motion recordings of the main shock throughout the region. The main goals of this research were to qualitatively and quantitatively compare the accuracy of different predictive models, and to explore the influence of factors such as landslide size, geologic unit, slope angle, and shear strength on the accuracy of the model predictions. Two different approaches were taken to assess the accuracy of the models – a cell-by-cell approach and a landslide-by-landslide approach.

### 5.1.1 Comparing Predictive Models

Estimates of sliding displacement were calculated using three empirical models developed by Jibson (2007) that predict displacement as a function of yield acceleration and ($I_a$), ($PGA$), and ($PGA$, $I_a$); and four empirical models developed by Rathje and Saygili (2008, 2009) that predict displacement as a function of yield acceleration and ($PGA$, $M$), ($PGA$, $PGV$), ($PGA$, $I_a$), and ($PGA$, $PGV$, $I_a$). The results of both the cell-by-cell analysis and the landslide-by-landslide analysis showed that, on average, there was not a significant difference in accuracy between the different predictive models. For a 5 cm displacement threshold, the highest average percentage of landslide cells captured (%GFC) was 41.3% by Model RS-($PGA$, $PGV$, $I_a$) and the lowest was 26.4% by Model J-($PGA$). In general, the models that predict displacement as a function of more than one ground motion parameter performed better than the models that predict displacement as a function of only one ground motion parameter. There was very little difference in the performance of the three vector models developed by Rathje and Saygili (Saygili and Rathje, 2008), suggesting that estimates of either $PGV$ or $I_a$ can be paired with estimates of $PGA$ and yield similar results.

The difference in results between the models developed by Jibson (2007) and the models developed by Rathje and Saygili (2008, 2009) can in part be explained by the use of a displacement threshold and the behavior of the models at different yield accelerations. Based on the plot in Figure 3.11 that shows a comparison of predicted displacements for all models as a function of yield accelerations, a 5 cm displacement threshold corresponds to yield accelerations of about 0.09 g using the Jibson (2007) models (i.e. values of $k_y$ < 0.09 g will result in displacements > 5 cm) and 0.12 g using the Rathje and Saygili (2008, 2009) models (i.e. values of $k_y$ < 0.12 g will result in displacements > 5 cm). This difference seems subtle but it means that more cells exceed

the displacement threshold using the Rathje and Saygili (2008, 2009) models than do using the Jibson (2007) models, and so more landslides are captured. This is also why the difference in results using a 5 cm threshold versus a 15 cm threshold is larger for the Rathje and Saygili (2008, 2009) models.

Surprisingly, the difference in results between predictive models was not as great as the difference in results between different quadrangles. For example, Model RS-($PGA$, $PGV$) with a 5 cm threshold captured 55.0% of landslide cells in the Oat Mountain quadrangle, but only 21.1% in the Simi Valley quadrangle. The model captured the same percentage of landslide cells in the Piru and Santa Susana quadrangles (~45%) but the ratio of predicted to observed landslide cells (%QC / %LS Area) was 12.0 in Piru and only 3.9 in Santa Susana. One possible reason for these discrepancies is that the shear strength values assigned to individual geologic units vary from one quadrangle to the next. For example, the shear strength values published by the California Geological Survey (CGS) for geologic unit Tm (Modelo formation) are ($c' = 31.3\ kPa$, $\varphi' = 39°$) within the Oat Mountain quadrangle, and ($c' = 12.0\ kPa$, $\varphi' = 35°$) within the neighboring Santa Susana quadrangle.

### 5.1.2 Factors Influencing Model Accuracy

Because the accuracies of the models using the landslide-by-landslide approach were smaller than those using the cell-by-cell approach, the distribution of landslide size within Oat Mountain was evaluated to see if the results were being skewed by a large number of small landslides. Looking at the maps of predicted and observed landslides, there appeared to be a number of 1 and 2-cell landslides scattered across each quadrangle that the models were not locating at all or the models were predicting landslides in cells immediately adjacent to the observed landslides. For a 1-cell landslide, the landslide-by-landslide approach is a binary problem; the model either captures it or does not capture it.

If the models were missing a lot of 1-cell landslides, it would hurt the results of the landslide-by-landslide approach but have little impact the results of the cell-by-cell analysis. However, the distribution of landslide sizes within Oat Mountain showed that despite a large percentage of small landslides (60% were less than 5 cells) the models were missing an equal percentage of small and large landslides across the quadrangle. This result is only significant because it means that there is some other factor influencing the model accuracy.

The influence of individual geologic units on model accuracy was evaluated by plotting the distribution of landslide cells captured in each unit in the Oat Mountain quadrangle. What was immediately noticeable was that not a single landslide cell was predicted within any geologic unit in Strength Group 1, despite the fact that nearly 20% of observed landslides occurred within these units. Given the level of ground shaking observed in the Oat Mountain quadrangle and the shear strength values assigned to these units ($c' = 31.3\ kPa,\ \varphi' = 39°$), only slopes steeper than about 63 degrees would be predicted to fail. All of the slopes in these geologic units were flatter than 60 degrees, and the majority of observed landslides occurred in slopes between 30 and 50 degrees. This result may indicate that the strengths assigned to Strength Group 1 were too large. In contrast, the model did very well capturing a large percentage of landslides (%GFC up to 80%) within the geologic units in Strength Group 2. Given the shear strength values assigned to these units ($c' = 13.3\ kPa,\ \varphi' = 32°$), slopes steeper than about 34 degrees would be predicted to fail. However, associated with a large %GFC is a large over-prediction of the total landslide area.

When different geologic units are grouped together and assigned one set of shear strength values, the prediction of displacement within that group becomes a function of only slope angle. The steeper the slope, the larger the displacement predicted. However,

the distribution of slope angles within observed landslide cells shows that the majority of landslides do not necessarily occur on the steepest slopes. Often times the steepest slopes exist because they represent the largest strength within a geologic unit. Assigning one set of shear strength values does not take into account the spatial variability of material strength within individual geologic units. This spatial variability is why landslides can be observed in 20 degree slopes but not in 60 degree slopes of the same geologic unit.

If the assigned shear strength values are high, only the steepest slopes will be predicted to fail. If the assigned strengths are low, too many of the flatter slopes will be predicted to fail. This result was shown in the comparison of results using strengths assigned in this study and strengths assigned by Jibson et al. (2000) and CGS. Jibson et al. (2000) used larger strengths and captured a significantly smaller number of observed landslides. The approach used by CGS ignores cohesion, which results in a large number of landslides captured but also results in predicted landslides covering more than half of some of the quadrangles. Without cohesion, many of the slopes within the quadrangles become statically unstable, which is not realistic. Thus, the strengths used by CGS and the resulting estimates of seismic stability are unrealistic.

## 5.2 RECOMMENDATIONS

Based on the results herein, the accuracy of permanent displacement analyses depends less on the predictive models used and more on the uncertainty in the parameters used as input to these displacement models (i.e. ground motion parameters and the shear strength parameters that affect $k_y$). Reducing the uncertainty in ground motion predictions and material properties will help improve predictions of seismic landslide hazard moving forward. Understanding the spatial variability of strengths within geologic units and preserving the relative differences in strength between units is particularly important. In addition to improving these model parameters, the conditions under which earthquake-induced landslides have occurred during past (and more recent) earthquakes must be documented and studied to continue developing criteria for assessing seismic landslide hazards.

With the emergence of GIS as a powerful research platform, the increasing availability of ground shaking data from sources like ShakeMap®, and better methods for documenting earthquake-induced landslides, these methodologies must continue to be validated against observations of landsliding from other earthquakes. To date, most validation exercises (including the study described herein) have focused on the Northridge earthquake. Data need to be compiled for landslides from other earthquakes such that other validation exercises can be performed on these data sets. Through these additional studies the observations from the Northridge earthquake can be extended.

# References


The Seismic Hazards Mapping Act, SHMA. (1990). California Public Resources Code, Chapter 7.8, Section 2690-2699.6.

Arias, A. (1970). A measure of earthquake intensity. In R. J. Hansen (Ed.), *Seismic design for nuclear power plants* (pp. pp 438-483). MIT Press, Cambridge MA.

Boore, D. M., & Atkinson, G. M. (2008). Ground motion prediction equations for the average horizontal component of PGA, PGV, and 5%-damped PSA at spectral periods between 0.01s and 10.0s. *Earthquake Spectra, Vol. 24*(1), pp. 99-138.

Boore, D. M., Joyner, W. B., & Fumal, T. E. (1997). Equations for estimating horizontal response spectra and peak accelerations from western North American earthquakes: a summary of recent work. *Seismological Research Letters, 68*, pp. 128-153.

Bray, J. D., & Travasarou, T. (2007). Simplified procedure for estimating earthquake-induced deviatoric slope displacements. *Journal of Geotechnical and Geoenvironmental Engineering, 133*(4), 381-392.

California Department of Conservation, C. G. (2002). *Seismic Hazard Zone Report for the Piru 7.5-Minute Quadrangle, Ventura County, California.*

California Department of Conservation, C. G. (2002b). *Seismic Hazard Zone Report for the Val Verde 7.5-Minute Quadrangle, Los Angeles and Ventura Counties, California.*

California Department of Conservation, C. G. (2008). *Guidelines for evaluating and mitigating seismic hazards in California.* Special Publication 117A.

California Department of Conservation, D. o. (1997). *Seismic Hazard Zone Report for the Newhall 7.5-Minute Quadrangle, Los Angeles County, California.*

California Department of Conservation, D. o. (1997b). *Seismic Hazard Zone Report for the Oat Moutain 7.5-Minute Quadrangle, Los Angeles County, California.*

California Department of Conservation, D. o. (1997c). *Seismic Hazard Zone Report for the Simi Valley East and Simi Valley West 7.5-Minute Quadrangles, Ventura and Los Angeles Counties, California.*

Cornell, C. A., & Luco, N. (2001). Ground motion intensity measures for structural performance assessment at near-fault sites. *Proceedings of the U.S.-Japan joint workshop and third grantees meeting, U.S.-Japan Coop. Res. on Urban EQ Disaster Mitigation.* Seattle, Washington.

Haneberg, W. C. (2006). Effects of digital elevation model errors on spatially distributed seismic slope stability calculations: an example from Seattle, Washington. *Environmental & Engineering Geoscience, XXI*(3), pp. 247-260.

Harp, E. L., & Jibson, R. W. (1995). *Inventory of landslides triggered by the Northridge, California earthquake.* U.S. Geological Survey Open-File Report 95-213.

Harp, E. L., & Jibson, R. W. (1996). Landslides triggered by the 1994 Northridge, California earthquake. *Seismological Society of America, 86*, S319-S332.

Holden, R. E., & Real, C. R. (1990). *Seismic hazard information needs of the insurance industry, local government, and property owners in California - an analysis.* California Division of Mines and Geology.

Jibson, R. (2010, Available online 1 October). Methods for assessing the stability of slopes during earthquakes - a retrospective. *Engineering Geology*, DOI: 10.1016/j.enggeo.2010.09.017.

Jibson, R. W. (1993). Predicting earthquake-induced landslide displacements using Newmark's sliding block analysis. *Transportation Research Record, 1411*, 9-17.

Jibson, R. W. (2007). Regression models for estimating coseismic landslide displacement. *Engineering Geology, 91*, 209-218.

Jibson, R. W., & Michael, J. A. (2009). *Maps showing seismic landslide hazard in Anchorage, Alaska.* 2 sheets (scale 1:25,000), U.S. Geological Survey Scientific Investigations Map 3077.

Jibson, R. W., Harp, E. L., & Michael, J. A. (1998). *A method for producing digital probabilistic seismic landslide hazard maps - an example from the Los Angeles, California area.* U.S. Geological Survey Open-File Report 98-113.

Jibson, R. W., Harp, E. L., & Michael, J. A. (2000). A method for producing digital probabilistic seismic landslide hazard maps. *Engineering Geology, Volume 58*(3-4), 271-289.

Joyner, W. B., & Boore, D. M. (1988). Measurement, characterization, and prediction of strong ground-motions . *Proceedings of the Conference on Earthquake Engineering & Soil Dynamics II* (pp. 43-102). Park City, UT: ASCE.

Keefer, D. K. (1984). *Landslides caused by earthquakes.* Geological Society of America Bulletin 95.

Keefer, D. K. (2002). Investigating landslides caused by earthquakes - a historical review. *Surveys in Geophysics, 23*, 473-510.

Kramer, S. L. (1996). *Geotechnical Earthquake Engineering.* Prentice-Hall, Inc.

Kramer, S. L. (1997). Modified Newmark model for seismic displacements of compliant slopes. *Journal of Geotechnical and Geoenvironmental Engineering, Vol. 123*(7), 635-644.

McCrink, T. P. (2001). Regional earthquake-induced landslide mapping using Newmark displacement criteria, Santa Cruz County, California. In H. Ferriz, & R. Anderson (Eds.), *Engineering Geology Practice in Northern California: California Division of Mines and Geology Bulletin 210 / Association of Engineering Geologists Special Publication 12* (pp. 77-92).

McCrink, T. P., & Real, C. R. (1996). *Evaluation of the Newmark method for mapping earthquake-induced landslide hazards in the Laurel 7-1/2 minute quadrangle, Santa Cruz County, California.* California Division of Mines and Geology Final Technical Report for the U.S. Geological Survey Contract 143-93-G-2334. U.S. Geological Survey, Reston, Virginia.

Newmark, N. (1965). Effects of earthquakes on dams and embankments. *Geotechnique, 15*(2), 139-160.

Rathje, E. M., & Saygili, G. (2009). Probabilistic assessment of earthquake-induced sliding displacements of natural slopes. *Bulletin of the New Zealand Society for Earthquake Engineering, 42*(1), 18-27.

Saygili, G. (2008). A probabilistic approach for evaluating earthquake-induced landslides. Ph.D. Dissertation, University of Texas at Austin, Austin, TX.

Saygili, G., & Rathje, E. M. (2008). Empirical predictive models for earthquake-induced sliding displacements of slopes. *Journal of Geotechnical and Geoenvironmental Engineering, 134*, 790-803.

Travasarou, T., Bray, J. D., & Abrahamson, N. A. (2003). Empirical attenuation relationship for Arias Intensity. *Earthquake Engineering & Structural Dynamics, 32*(7), 1133-1155.

Wald, D. J., Heaton, T. H., & Hudnut, K. W. (1996). Rupture history of the 1994 Northridge, California earthquake from strong-motion, GPS, and leveling data. *Bulletin of the Seismological Society of America, 86*, S49-S70.

Wu, Y. M., Teng, T. L., Shin, T. C., & Hsiao, N. C. (2003). Relationship between peak ground acceleration, peak ground velocity, and intensity in Taiwan. *Bulletin of the Seismological Society of America, 93*, 386-396.

Yerkes, R. F., & Campbell, R. H. (1995a). Preliminary geologic map of the Newhall 7.5-minute quadrangle, southern California: a digital database. U.S. Geological Survey OFR 95-800.

Yerkes, R. F., & Campbell, R. H. (1995b). Preliminary geologic map of the Oat Mountain 7.5-minute quadrangle, southern California: a digital database. U.S. Geological Survey OFR 95-89.

Yerkes, R. F., & Campbell, R. H. (1995c). Preliminary geologic map of the Piru 7.5-minute quadrangle, southern California: a digital database. U.S. Geological Survey OFR 95-801.

Yerkes, R. F., & Campbell, R. H. (1995d). Preliminary geologic map of the Val Verdel 7.5-minute quadrangle, southern California: a digital database. U.S. Geological Survey OFR 95-699.

Yerkes, R. F., & Campbell, R. H. (1997a). Preliminary geologic map of the Santa Susana 7.5-minute quadrangle, southern California: a digital database. U.S. Geological Survey OFR 97-258.

Yerkes, R. F., & Campbell, R. H. (1997b). Preliminary geologic map of the Simi 7.5-minute quadrangle, southern California: a digital database. U.S. Geological Survey OFR 97-259.